

**Power Supplies for  
High-Power Piezoelectric  
Multi-Mass Ultrasonic Motor**

Zur Erlangung des akademischen Grades

**DOKTORINGENIEUR (Dr.-Ing.)**

der Fakultät für Elektrotechnik, Informatik und Mathematik  
der Universität Paderborn  
genehmigte Dissertation  
von

M.Sc. Rongyuan Li  
Guizhou, China

Referent: Prof. Dr.-Ing. Joachim Böcker  
Korreferent: Prof. Dr.-Ing. Andreas Steimel

Tag der mündlichen Prüfung: 29.01.2010

Paderborn, den 05.07.2010

Diss. EIM-E/263



## Declaration

I confirm that the work submitted in this dissertation is the result of my own investigation and all the sources I have used or quoted have been acknowledged by means of complete references.

Paderborn, Sep.21.2009

---

Rongyuan Li

to my loving parents, wife and son.

## Acknowledgments

The work submitted in this dissertation has been carried out during my research as scientific co-worker at University of Paderborn, department of Power Electronics and Electric Drives (LEA), Germany.

I would like to express my sincerely high appreciation to my advisor Prof. Dr.-Ing. Joachim Böcker for his strict confidence, availability and full support throughout the whole period of my doctoral research. Dr. Böcker's extensive vision and creative thinking have been the source of my inspiration for the Ph.D work.

I sincerely thank Dr.-Ing. Norbert Fröhleke, he gives me guidance, encouragement and support during all the time. In an incredible short time, he carefully reads all my manuscript and gives invaluable remarks.

I would like to appreciate Prof. Dr.-Ing Horst Grotstollen and Prof. Xingshan Li (Beihang University, China), they kindly initiate me into the study in the department of Power Electronics and Electric Drives (LEA) at University of Paderborn for pursuing my doctor's degree.

I would like to thank Prof. Dr.-Ing. Andreas Steimel, as an important member of the committee, he gives good advices and suggestions for my manuscript. I also want to thank all of the other committee members.

It has been a great pleasure to work in the group of LEA, and to work with such talented, hard-working and creative colleagues. I would like to thank all of them, their friendships and help make my stay at LEA pleasant and enjoyable. This is a happy reminiscent stage in my life.

I also want to thank the administrative and technical co-workers of LEA for their great help. Special thanks are due to Mr. Norbert Sielemann for his fruitful

collaboration in the realization of hardware for the laboratory prototypes.

I'd like to give my sincere thanks to my parents for their endless love, encouragement and support throughout my life.

Finally, I would like to thank my wife, Manli Hu, who has always been there with her love, encouragement and understanding during this period of my doctoral study.

Thanks belong to the European Community for funding the PIBRAC project under AST4-CT-2005-516111 as well as our project partners.

# Kurzfassung

Verglichen mit klassischen elektromagnetischen Motoren weisen piezoelektrische Ultraschallmotoren hohes Drehmoment bei niedrigen Drehzahlen und niedrige Trägheit auf, was sie für spezielle industrielle Anwendungen, bei denen es auf hohe Kraftdichten ankommt, qualifiziert. So sind sie im Kontext der europäischen und amerikanischen Förderprogramme zu "More Electric Aircraft" favorisierte Akteure. Bisher jedoch existieren keine industriellen piezoelektrischen Antriebe, bestehend aus Motor und geregelter Stromversorgung im Leistungsbereich von einigen Kilowatt, wie sie für den Ersatz hydraulischer Bremsen für Flugzeuge erforderlich sind. Das europäische Projekt PIBRAC (Piezoelectric Break Actuator) zielt darauf ab, die Technologie eines leistungsstarken piezoelektrischen Multimassen-Ultraschallmotors, der durch ein Vorprojekt entwickelt wurde, für einen Flugzeugbremsaktuator zu entwickeln.

Ziel dieser Dissertation ist es, eine passende elektronische Stromversorgung für die Speisung eines Multimassen-Ultraschallmotors zu untersuchen und zu entwickeln.

Dazu wird zunächst eine Literaturübersicht über die Konzepte der Stromrichter gegeben, die hinsichtlich Blindleistungskompensation, harmonische Verzerrungen und ihrer Beeinflussung durch Mehrstufen-Wechselrichter beurteilt werden. Ebenso in die Beurteilung eingeschlossen sind Entwurfsaspekte der Filterschaltung und Regelung.

Der neu vorgeschlagene LLCC-PWM Umrichter, bestehend aus LLCC-Filter kombiniert mit PWM Stromrichter, wird zur Anregung des piezoelektrischen Hochleistungsmotors entwickelt. Zwei- und Drei-Stufen Wechselrichter in Verbindung mit PWM Techniken wurden hinsichtlich Elimination von Oberschwingungen, Verlustleistungen, harmonischer Verzerrung, Volumen und Gewicht des Filters untersucht.

Um ausgewählte Oberschwingungen (3., 5., 7. und 9. Oberschwingungen) der Speisespannung zur Lebensdauererlängerung der piezoelektrischen Stacks zu beseitigen, werden entsprechende Schaltwinkel der PWM off-line berechnet.

Oberschwingungen höherer Ordnung werden durch die LLCC Filtereigenschaften ausreichend gedämpft.

Mit der neuartigen Lösung sind folgende bedeutende Vorteile verbunden:

1. Die Blindleistung des piezoelektrischen Aktors wird lokal kompensiert, indem die parallel angeordnete Spule nahe am Aktor angebracht wird. Folglich liefert der gesamte vorgeschaltete Schaltungsteil bestehend aus Wechselrichter, Schwingkreis, Transformator und Kabel, welches im Flugzeug durchaus 20 Meter lang sein kann, überwiegend Wirkleistung. Dadurch kann der Wirkungsgrad erhöht und die Belastung der vorgenannten Bauteile verringert werden.
2. Das Ausgangsfilter weist, verglichen mit den klassischen Resonanzumrichtern, eine optimierte Leistung bei minimalem Volumen und Gewicht auf, und nutzt darüber hinaus die Streuinduktivität des Transformators sowie die Induktivität des Kabels.
3. Die gesamte harmonische Verzerrung (THD) der piezoelektrischen Aktor - Spannung wird bei gleichbleibender Schaltfrequenz reduziert.

Für den Steuerungsentwurf wird ein Mittelwertmodell für den Multimassen-Ultraschallmotor vorgeschlagen. Die Regelungsentwürfe werden durch Simulationen zum transienten und stationären Verhalten untersucht und überprüft. Ein Spannungsregler mit Vorsteuerung, gegründet auf einer vereinfachten inneren Übertragungsfunktion, wird dann vorgestellt. Ein FPGA wird als Controller aufgrund seiner Flexibilität und Verarbeitungsgeschwindigkeit eingesetzt.

Andere Anwendungsbereiche der LLCC-PWM Umrichter sind: Ultraschall-unterstützte Materialbearbeitung wie Bohren, Schneiden, Meißeln und Fräsen.

# Abstract

Due to the particular performances of piezoelectric ultrasonic motors compared to classical electromagnetic motor, such as high torque at low rotational speed and low inertia, they qualify for specific industrial applications. During the progress towards the "More Electric Aircraft", research and development of actuators based on piezoelectric technology impact more technological innovations. However, an industrialized piezoelectric device consisting of motor and its power supply do not exist in the kilowatt power range and above. They are required, e.g. for piezoelectric brake actuators to replace hydraulic brake actuators used in aircrafts. Hence, the European project PIBRAC aims to research the high-power piezoelectric multi-mass ultrasonic motors technology in order to develop an aircraft brake actuator for an advanced application.

The purpose of this dissertation is to investigate the technology of designing the power supply and its control for driving high power piezoelectric multi-mass ultrasonic motor developed in PIBRAC project.

A comprehensive literature survey is presented on reactive-power compensation, harmonic distortion, multilevel inverter techniques, filter circuit design issues, control issues, and fundamental issues on piezoelectric actuator drive schemes.

The proposed LLCC-PWM inverter was developed to excite the high-power piezoelectric ultrasonic motors, where a LLCC-filter circuit is utilized and operated in PWM-controlled mode. Two-level and three-level harmonic elimination technologies are investigated in respect to power losses, total harmonics distortion, volume and weight of the filter circuit.

In order to eliminate selected harmonics (3<sup>rd</sup>, 5<sup>th</sup>, 7<sup>th</sup> and 9<sup>th</sup> harmonic) for prolonging the lifetime of the piezoelectric stacks, suitable switching angles of the PWM are calculated off-line. Other higher frequency harmonics will be sufficiently suppressed by the LLCC filter characteristics.

The proposed solution offers significant advantages to improve the performance of the power supply as follows.

1. Reactive power of the piezoelectric actuator is compensated locally, by placing the inductor close to the actuator. Therefore power supply and the cable connecting power supply and piezoelectric actuator provide mostly active power, their volume and weight are reduced consequently.
2. The output filter shows optimized performance at minimized volume and weight, compared to the classical resonant inverters, and makes use of leakage inductance of transformer and cable inductance.
3. Total harmonic distortion (THD) of the piezoelectric actuator voltage is reduced without increasing the switching frequency.

Control schemes are proposed for driving the MM-USM. For control design, an averaging model of the MM-USM driven by LLCC PWM inverter is studied and verified by simulation results at transient and steady state conditions. A feed-forward voltage controller is designed and implemented, based on a simplified inner loop transfer function. A FPGA is employed as controller by reason of its flexibility, fast and parallel processing characteristics.

The proposed LLCC-PWM inverter was employed for driving a high power airborne piezoelectric brake actuator in an European project PIBRAC. Other potential fields of application of LLCC-PWM inverters are: superimposed sonotrodes assisted ultrasonic drilling, cutting, and milling of tooling machines.

# Nomenclature

$C_m$	Electric equivalent serial resonance capacitance of mechanical load
$C_p$	Piezoelectric capacitance
$C_s$	Serial resonance capacitance of LLCC filter circuit
$i_{iv}(t)$	Current of power inverter output
$i_{L_s}(t)$	Current of inductance $L_s$
$f_{mr1}$	Mechanical resonance frequency
$f_{Op}$	Operating frequency of MM-USM
$G_{LLCC}(s)$	Transfer function of LLCC filter circuit
$G_{f,el}(z)$	Electrical subsystem transfer function represented by a pre-filter using second order Butterworth filter
$L_m$	Electric equivalent serial resonance inductance of mechanical load
$L_p$	Parallel inductance of LLCC filter circuit
$L_s$	Serial inductance of LLCC filter circuit
$M$	Admittance ratio
$\mathbf{M}_a$	Reference vector of $\hat{U}_{iv}^\star$
$\omega_{mr1}$	Mechanical resonance frequency
$P_{Avg}$	Conjugate complex poles of averaging model of electrical subsystem

---

$P_{PI}$	Conjugate complex poles of LLCC filter
$Q_M$	quality factor
$R'_p$	Electric equivalent resistance of mechanical load
$S_i(t)$	Gate drive signals of MOSFETs, $i = 1, 2, \dots$
$\hat{U}_{1iv}$	Magnitude of fundamental component of inverter output voltage
$\hat{U}_{1iv}^\star$	Set-value of first Fourier coefficient
$U_{dc}$	DC-link voltage
$u_{set}$	Set-value of inverter voltage $u_{iv}(t)$
$\hat{U}_{viv}$	Fourier coefficient of inverter output voltage
$u_{Cp}(t)$	Voltage of piezoelectric actuator
$u_{tri}(t)$	Triangle signals used for CBM
$u_{sin}(t)$	Sinusoidal reference signal for CBM
$u_{iv}(t)$	Inverter output voltage
$\mathbf{x}_{el}$	State variables of the electrical subsystem
$x_s(t), x_c(t)$	Slowly time-varying Fourier coefficients
$Y_{LLCC}(s)$	Admittance of LLCC filter circuit
$Y_{Pi}(s)$	Admittance of electric equivalent circuit of piezoelectric actuator
$\alpha_i$	Switching angles
$\alpha_{LLCC}$	Design parameter for LLCC filter circuit
$\boldsymbol{\alpha}^{(j)}$	Vector with switching angles $\alpha_i$ , , where $j$ is the iteration count of the loop
$\lambda$	Power factor

## GLOSSARY

<b>Converter</b>	Consisting of inverter and filter.
<b>CBM</b>	Carrier-based pulse width modulation.
<b>Filter</b>	Comprising discrete filter components such as inductors and capacitors
<b>EMA</b>	Electromagnetic actuator.
<b>HEM</b>	Harmonic elimination modulation.
<b>Inverter</b>	Fundamental power circuitry built with high-power semiconductor switches such as power diodes, power MOSFETs and IGBTs
<b>MM-USM</b>	Multi-mass ultrasonic motor.
<b>PIBRAC</b>	Piezoelectric brake actuator.
<b>Power supply</b>	Consisting of inverter, filter and cable.
<b>THD</b>	Total harmonic distortion
<b>TW-USM</b>	Traveling-wave-type ultrasonic motor.



# Contents

<b>Nomenclature</b>	<b>i</b>
<b>1 Introduction</b>	<b>1</b>
1.1 Background . . . . .	1
1.2 Motivation and Objective . . . . .	4
1.3 Dissertation Structure . . . . .	7
<b>2 A High-Power Airborne Piezoelectric Brake Actuator</b>	<b>9</b>
2.1 Modeling of Piezoelectric Actuators . . . . .	9
2.2 Multi-Mass Ultrasonic Motor . . . . .	16
2.3 Power Consumption of a Brake Actuator . . . . .	23
2.4 Requirement of Power Supply and Control . . . . .	26
<b>3 Power Supply Topologies for High-Power Piezoelectric Actuators</b>	<b>29</b>
3.1 State-of-the-Art of Power Supplies for Piezoelectric Actuators . . . . .	30
3.1.1 Classification of Power Supplies for Driving Piezoelectric Actuators . . . . .	30
3.1.2 Resonant Switching Power Supply for Driving High-Power Piezoelectric Actuators . . . . .	32
3.1.2.1 Inverter Topologies and Square-wave Modulation	32
3.1.2.2 LC-Resonant Inverter . . . . .	36
3.1.2.3 LLCC-Resonant Inverter . . . . .	40
3.1.3 PWM-Controlled Inverter with LC Filter . . . . .	46
3.1.3.1 Inverter Topology and Pulse Width Modulation . . . . .	46

## CONTENTS

---

3.1.3.2	LC-PWM Inverter . . . . .	48
3.2	Advanced Power Supply Concepts . . . . .	52
<b>4</b>	<b>PWM-Controlled Driving Concept with LLCC-Filter Circuit</b>	<b>55</b>
4.1	LLCC-Filter Circuit Design Fed by PWM Inverter . . . . .	56
4.1.1	Design Consideration . . . . .	56
4.1.2	Design of Filter Parameters . . . . .	58
4.2	Advanced Pulse Width Modulation Design . . . . .	61
4.2.1	Introduction . . . . .	61
4.2.2	LLCC Two-Level Inverter Using Selected Harmonics Elimination Technique . . . . .	62
4.2.2.1	PWM with Elimination of Selected Harmonics . . . . .	63
4.2.2.2	Effects on LLCC Filter . . . . .	67
4.2.3	LLCC Three-Level Carrier-Based PWM Inverter . . . . .	69
4.2.3.1	Three-Level PWM Inverter and its Carrier-Based PWM . . . . .	71
4.2.3.2	Effects on LLCC Filter . . . . .	76
4.3	Evaluation and Comparison of Power Supply Topologies . . . . .	79
4.3.1	Switching Conditions . . . . .	79
4.3.2	Preliminary Design of Filter Components . . . . .	82
4.3.2.1	Filter Components . . . . .	82
4.3.2.2	Filter Performance . . . . .	84
4.3.3	Power Factor . . . . .	85
4.3.4	Total Harmonic Distortion (THD) . . . . .	86
4.3.4.1	THD of Inverter Output Voltage . . . . .	86
4.3.4.2	THD of Filtered Voltages . . . . .	87
4.3.5	Estimation of Efficiency and Weight . . . . .	90
4.3.6	Comparison Results . . . . .	91
4.4	Experimental Validation . . . . .	92
4.4.1	Prototype Design . . . . .	92
4.4.1.1	Power Circuitry and Control Interface . . . . .	93
4.4.1.2	Control Circuitry and Auxiliary Functions . . . . .	94
4.4.2	Measurements with Three-Level CBM . . . . .	95

4.4.3	Measurements with Two-Level HEM . . . . .	96
4.5	Summary . . . . .	97
<b>5</b>	<b>Investigation on LLC Three-Level PWM inverter</b>	<b>99</b>
5.1	Three-Level Harmonic Elimination Modulation (HEM) . . . . .	99
5.2	LLC Three-Level HEM Inverter . . . . .	104
5.3	Strategy for Voltage-Balancing Control . . . . .	107
5.4	Cascaded DC-DC-AC Three-Level Topology . . . . .	111
5.5	Measurement Results of LLC Three-Level Inverter with Equiva- lent Load . . . . .	112
5.6	Summary . . . . .	113
<b>6</b>	<b>Control Design of Power Supply</b>	<b>115</b>
6.1	Control Objective . . . . .	115
6.2	Modeling of MM-USM Driven by LLC-PWM Inverter . . . . .	116
6.2.1	Generalized Averaging Method . . . . .	116
6.2.2	Averaging Model of Electrical Subsystem . . . . .	116
6.2.3	Averaging Model of Piezoelectric Mechanical Subsystem . . . . .	118
6.2.4	Dynamic Behavior Analysis . . . . .	121
6.3	Voltage and Current Control Scheme Based on FPGA Implemen- tation . . . . .	124
6.3.1	Voltage and Current Control Schemes . . . . .	124
6.3.2	Measurement and Signal Processing Scheme . . . . .	125
6.3.3	Feed-Forward Voltage Control . . . . .	126
6.4	Experiment on Driving MM-USM . . . . .	128
6.5	Summary . . . . .	130
<b>7</b>	<b>Conclusion</b>	<b>131</b>
<b>A</b>	<b>Definition</b>	<b>143</b>
A.1	Power Factor . . . . .	143
A.2	General Fourier Coefficient Solution of Inverter Voltage . . . . .	143
A.3	Harmonic Elimination Modulation (HEM) Using Newton Algorithm	146
A.4	Total Harmonic Distortion (THD) . . . . .	148

## CONTENTS

---

<b>B Design Aspects</b>	<b>149</b>
B.1 Inductive Components Using Area Products . . . . .	149
B.2 Efficiency Calculations . . . . .	150

# Chapter 1

## Introduction

### 1.1 Background

At the beginning of the last century airplanes had a relatively simple structure. Before the forties and fifties of the last century, electromagnetic actuators were employed dominantly as drives in different devices of the aircrafts. Along with the availability of powerful hydraulic and pneumatic components, they gradually replaced airborne electromagnetic actuators. This historical development has changed back for modern aircrafts, as an expensive supply system is implemented with the three kinds of on-board subsystems: electrical, hydraulic and pneumatic subsystems. This causes a number of disadvantages in respect to safety issues and maintenance cost.

#### **A. Airborne hydraulic brake**

The brake system is an important safety-relevant system of the airplane, which is to stop the heavy airplane in a short landing time. The brake consists of a pile of carbon disks, which are pressed together by the hydraulic cylinders, see Fig. 1.1. These hydraulic cylinders enable the symmetric pressing of the rotating carbon disks. An anti-skid brake system (ABS), which was first used in airplanes in 1920, nowadays has been adopted as a standard equipment for the control of the brakes.

The fluids of the hydraulic subsystem are spread within the aircraft in a wide network of pipes, and must be controlled and refilled at regular relative short inter-

## 1. INTRODUCTION

---

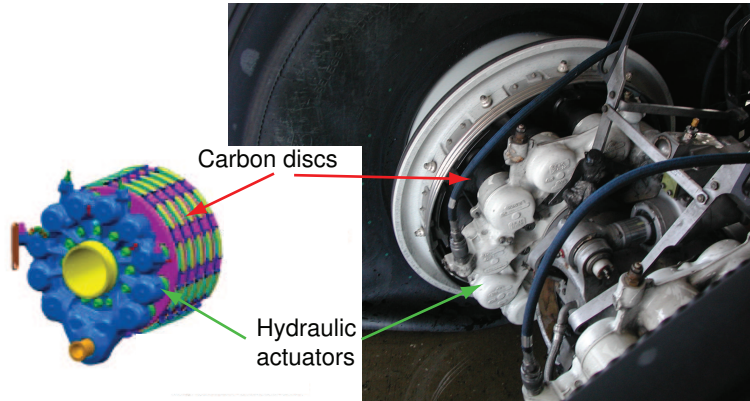


Figure 1.1: Airborne hydraulic brake

vals, so the maintenance of this subsystem is costly. Leakage of the hydraulic subsystem results in environmental pollution and is nearly inevitable. Furthermore, hydraulic oil is inflammable and leads to a danger of fire. All these disadvantages of the hydraulic brake system accelerate the development of electromechanical brakes in recent years.

### B. Airborne electromechanical brake

Fig. 1.2 shows the first modern airborne electromechanical brake building with an electromechanical actuator (EMA), which was developed by the French company Messier Bugatti and is presently in the test phase [MB06]. High-power density permanent magnet synchronous motors (PMSM) are adopted as the electric drives. The rotational movement of the motor is converted to a linear motion by a ball screw, but an additional reduction gear with high transfer ratio has to be inserted to adapt the high rotational speed of the motor to the slow shift of the ball screw.

The electromechanical brake reduces significantly maintenance cost and fire risk. After the first flight demonstrator was tested in the United States of America (USA) several years ago, Boeing decided to fit electromechanical brakes in their new 787 Dreamliner. In the programs: "More Electric Aircraft" and "ALL Electric Aircraft", the companies EADS, Airbus and Messier Bugatti plan to reduce or even completely replace the hydraulic or pneumatic systems with the electric systems in the airplane brake systems for Airbus and Boeing [JGvdB04]

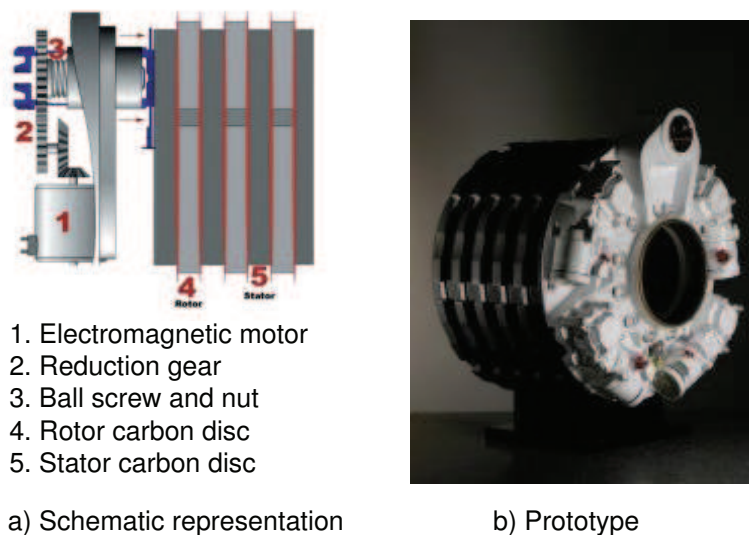


Figure 1.2: Airborne electromechanical brake

[JC06] [Fal06]. It is therefore probable that electromechanical brakes become the standard brake in new aircrafts in the future.

However, the electromechanical brake with conventional electromagnetic motor and reduction gears bring a weight increase and a very high electric peak power consumption. The main part of this energy is wasted in the kinetic energy of the high inertia of motor rotors and reduction gears due to the high frequency of the command of the actuator during anti-skid operation. Due to the limitation of airborne electromechanical brake with electromagnetic motors, it should be considered as the first step for hydraulic system replacement [AAOW06].

### C. Airborne piezoelectric brake

In contrast to electromagnetic motors, well-designed piezoelectric ultrasonic motors can produce high torque with small rotational speed and require therefore no reduction gear for the above case. The mass (without power supply) and the resulting inertia of the piezoelectric drives are smaller compared with that of electromagnetic drives. These advantages make the piezoelectric drives a good alternative to the electromagnetic drives, and let it be attractive for the aircraft industry [JGvdB04].

## 1. INTRODUCTION

---

As classical piezoelectric drive solution, the traveling-wave-type ultrasonic motors (TW-USM) are well known [MSF00], but they are available only for small-power applications up to approx. 20 watt and suffer from a poor efficiency. During the European Commission (EC) project PAMELA, the French company SAGEM developed a new generation of piezoelectric ultrasonic motors named multi-mass ultrasonic motor (MM-USM). They were designed to replace hydraulic actuators on the secondary flight-control surfaces in aircrafts (like flaps, spoilers and trimming etc.) [SF01].

An even more advanced innovation of airborne actuators is the adoption of brake actuators based on piezoelectric technology [WLFB07]. In order to evaluate the advantages of this technology, a new EC project PIBRAC was proposed. The objective of the PIBRAC project is to develop a piezoelectric brake for airplanes based on a aforementioned MM-USM. Compared with conventional EMA, the MM-USM meets the requirements of the aircraft brake actuators very well with an high torque level at low speed, a low inertia with short response time and a high power-to-weight ratio. So if a MM-USM is adopted to drive the ball screw (see Fig. 1.2) directly for above case, the complex reduction gear can be omitted, and the inertia of the actuator can be reduced significantly.

### 1.2 Motivation and Objective

Piezoelectric actuators generate microscopic mechanical ultrasonic vibrations based on the principle of the inverse piezoelectric effect at small and medium power. A high power density can only be achieved at ultrasonic frequencies with the use of resonant amplification by the mechanical part. Though the power has to be converted from serial microscopic, high-frequency oscillation to a linear or rotatory movements by a frictional contact [Mas98], piezoelectric actuators are becoming more and more popular in aircraft and industry. They are used to construct various kinds of piezoelectric systems such as ultrasonic motors and sonotrodes for ultrasonic machining, welding and cleaning.

In contrast to conventional electromagnetic actuators, piezoelectric actuators do not make use of magnetic fields and behave non-inductively. In fact, a piezoelectric actuator is known to exhibit a distinct capacitive behavior, which has to

## 1.2 Motivation and Objective

---

be considered when designing the power supply. A closer inspection reveals that the electrical behavior depends on the frequency-dependent interactions between the actuator and the load. Previous works on ultrasonic motors have shown that the motor's quality factor ( $Q_M$ ), which is the product of a capacitive reaction of the motor with the mechanical quality of the oscillatory system and is used to measure the system damping, has a strong influence on choosing the converter topology.

Up to now piezoelectric motors have been realized with low power (less than 100 W). In order to satisfy the requirements of direct drives in airplanes, a novel piezoelectric motor with a power rating of several kW should be developed, to generate the demanded mechanical vibration force. Although power supplies for ultrasonic applications like piezoelectric motors and sonotrodes are available in the market, however, they cover only a range of some ten watts, which is far away from the demanded kW range.

Appropriate vibration is expected in the ultrasonic frequency range of 20 - 40 kHz. The task of the power supply is to excite the piezoelectric actuators at such frequency. This means the electrical power taken from the aircraft power supply has to be converted to oscillating voltages and currents of that frequency. Furthermore, the level of voltages and currents needs to be adjusted in order to properly control the actuator force. Since each energy conversion causes losses, the electrical conversion contributes also to the losses of the brake actuator. One goal is to realize an electrical efficiency of about 90 % or even better, in order to achieve an acceptable overall brake actuator efficiency of about 40 %. This can only be achieved by an optimal design of the power electronic system to the particular needs of the ultrasonic motor. Furthermore the volume and weight of the power supply need to be optimized to satisfy the novel brake system specifications.

Major goals of the PIBRAC project, which represents the base for this investigation and development, are a reduction of

- volume and weight
- peak power consumption

## 1. INTRODUCTION

---

The converter output filter is also an object of the investigation, since it is required to suppress output current or voltage harmonics, whatever is applied in resonant converter or PWM converter. In its simplest configuration the system consists of one inductor in series with the piezoelectric capacitance, which results in a LC-type filter, but of course also higher-order filters like LLC- or LLCC-type can be employed. Objectives for the filter design are the reduction of the harmonic content of the output voltage, the reduction of weight (since especially the inductances may grow bulky), and the improvement of dynamic response, efficiency and robustness. Some filter types are known to be rather sensitive to parameter variation caused by temperature changes of the actuator, so that a feedback control should be adopted to stabilize the system by adjusting the amplitude, phase or frequency. Other filter types have shown to be more robust, and the corresponding control scheme can be accomplished with less complexity and cost. These issues must be taken into account when choosing the appropriate converter topology.

A novel concept of PWM-controlled LLCC inverter in the kW power range is developed and implemented in order to feed the multi-mass ultrasonic motor (MM-USM) with the high-power piezoelectric actuators. It is designed to reduce the total harmonic distortion of the motor voltage and to locally compensate the reactive power of the piezoelectric actuators. In order to limit the switching frequency, an optimal pulse width modulation method using harmonic elimination is designed and implemented on a FPGA.

Detailed studies on the stationary and dynamic behavior by computer simulation are necessary to design the control scheme. Furthermore the requirements for the brake control have to be considered as well as the various boundary conditions such as starting and stopping operation mode of the brake.

A cascaded voltage and current controller is designed to adjust the driving voltage within a suitable frequency range. By combining PWM inverter and LLCC filter, the whole power supply shows optimal performance with minimal volume and weight contrasting to LC- and LLCC-resonant controlled converters.

### 1.3 Dissertation Structure

The dissertation is organized and divided into following sections:

1. At first, the operating principle of piezoelectric actuators and the MM-USM are discussed in Chapter 2. After that the power consumption of the piezoelectric brake actuator is analyzed, then the description of the driving concept via a power supply is also presented in Chapter 2.
2. A detailed evaluation of the state-of-the-art of power supplies for driving piezoelectric ultrasonic motors is given in Chapter 3, which includes inverter topologies, filters and modulation schemes.
3. Two kinds of novel power-supply concepts are presented in Chapter 4, supplemented by a list of comparison criteria. This is concluded by the determination of the most qualified power-supply topology.
4. Improvements for a three-level inverter control using the harmonic elimination modulation method are described in Chapter 5.
5. In Chapter 6, modeling of the power supply using the selected topology treated in Chapter 4 and Chapter 5, as well as the piezoelectric motor stator are described, based on a suitable generalized averaging method. A model-based control scheme of the power supply is presented. Validations of power supply and control scheme are also given in Chapter 6.
6. Conclusions are finally stated in Chapter 7.



## Chapter 2

# A High-Power Airborne Piezoelectric Brake Actuator

High-power piezoelectric actuators are used to build up various kinds of piezoelectric systems like ultrasonic motors and sonotrodes for ultrasonic machining. Due to the high force generation, they are becoming more and more attractive in aircraft and industrial applications.

In this chapter, the basic operating principle of the piezoelectric actuator is studied firstly. After that special emphasis is laid on the analysis of the electrical behavior of a multi-mass ultrasonic motor (MM-USM), which is developed for a high-power airborne piezoelectric brake actuator using high-power piezoelectric actuators. Lastly, the design specifications and the description of the driving concept by the application oriented power supply are presented.

### 2.1 Modeling of Piezoelectric Actuators

Piezoelectric actuators are normally constructed using solid-state piezoelectric ceramic actuators. Unlike the conventional electromagnetic actuator, the piezoelectric actuator converts electrical energy directly into mechanical energy through linear motion, without utilizing the interaction of magnetic fields to produce the force or torque. Usually they are able to generate high pressure from 35 to 50 MN/m<sup>2</sup>, in comparison to approximated from 0.05 to 1 MN/m<sup>2</sup> of electromagnetic actuators [Uch97].

## 2. A HIGH-POWER AIRBORNE PIEZOELECTRIC BRAKE ACTUATOR

---

Moreover in case of actuators preloaded by mechanical pressure, the actuators can also be supplied with pure AC-voltage sources and can be operated in their mechanical resonance frequency, which ensures efficient operating [SF01].

A piezoelectric actuator mostly consists of several piezoelectric elements if a rotating action for a motor is to be formed, which are considered as an electromechanical vibration system [Uch97]. For the analysis of piezoelectric actuators the load is represented by the well-known equivalent circuit depicted in Fig. 2.1, it is based on the electrical and mechanical characteristics [Wal95].

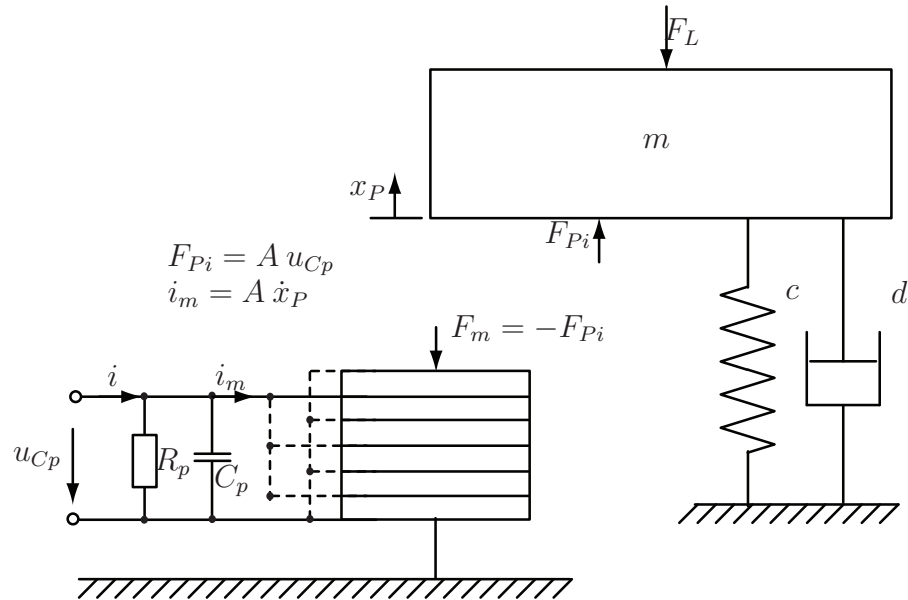


Figure 2.1: Principle of a piezoelectric actuator

Usually the capacitance formed by the piezoelectric material are represented as  $C_p$ , and the dielectric losses within the ceramics represented as  $R_p$ . The usual value of this resistor is very large and hence the losses caused by this can be neglected. And then, the electrical equivalent of capacitive current can be written as:

$$C_p \dot{u}_{Cp} = i - \frac{1}{R_p} u_{Cp} - i_m \quad (2.1)$$

In various contributions [Uch97] [Wal95] [Gro02], the mechanical parts of the piezoelectric actuator are described generally by a spring-mass-damper system, and it is described by

$$m \ddot{x}_P = F_{Pi} - c x_P - d \dot{x}_P - F_L \quad (2.2)$$

## 2.1 Modeling of Piezoelectric Actuators

where  $F_{Pi}$  is the force of the piezoelectric actuator excited by the voltage  $u_{Cp}$ , and  $F_L$  represents the mechanical load. The coupling between the electrical resonance system and the mechanical vibration system is defined by force factor  $A$ . The behavior described by Eq. 2.1 and Eq. 2.2 can be represented as block diagram as shown in Fig. 2.2.

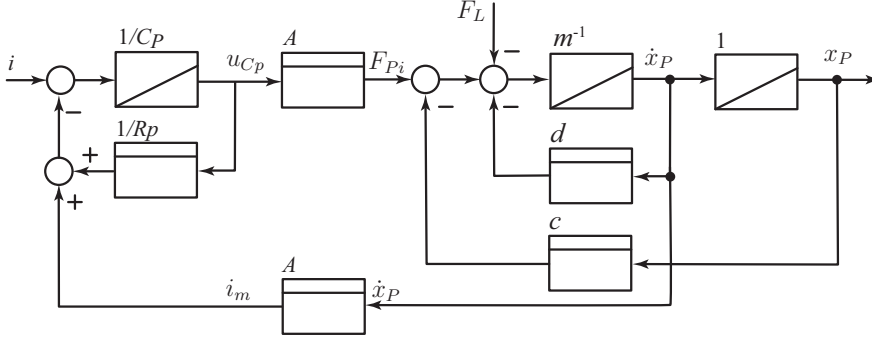


Figure 2.2: Action diagram of a piezoelectric actuator

With  $u_{Cp}$ ,  $\dot{x}_P$ ,  $x_P$  selected as state variables and with the input variable  $i$ , a state space model can be derived from Eq. 2.1 and Eq. 2.2 as:

$$\begin{bmatrix} \dot{u}_{Cp} \\ \dot{x}_P \\ \ddot{x}_P \end{bmatrix} = \begin{bmatrix} \frac{-1}{C_p R_p} & 0 & -\frac{A}{C_p} \\ 0 & 0 & 1 \\ \frac{A}{m} & -\frac{c}{m} & -\frac{d}{m} \end{bmatrix} \begin{bmatrix} u_{Cp} \\ x_P \\ \dot{x}_P \end{bmatrix} + \begin{bmatrix} \frac{1}{C_p} \\ 0 \\ 0 \end{bmatrix} i \quad (2.3)$$

Mechanical system	Electrical system	Relation
Mass $m$	Inductance $L_m$	$L_m = m/A^2$
Damping $d$	Resistor $R_m$	$R_m = d/A^2$
Stiffness $c$	Capacitance $C_m$	$C_m = A^2/c$
Force $f_{Pi}$	Voltage $u_{Cp}$	$f_{Pi} = A u_{Cp}$
Displacement $x$	Charge $q_m$	$i_m = \dot{q}_m = A \dot{x}$

Table 2.1: Equivalence relations between mechanical and electrical quantities

In order to analyze the behavior of the mechanical vibration system and its effects on the power supply the mechanical variables are transferred to equivalent electrical components and are tabulated in Tab. 2.1 for the comparison of quantities.

## 2. A HIGH-POWER AIRBORNE PIEZOELECTRIC BRAKE ACTUATOR

---

Moreover the spring-mass-damper system can be replaced by its equivalent electrical circuit (see Fig. 2.3(a)) for the resonant operation according to the great pioneer in the piezoelectric field Arno Lenk [Len74].

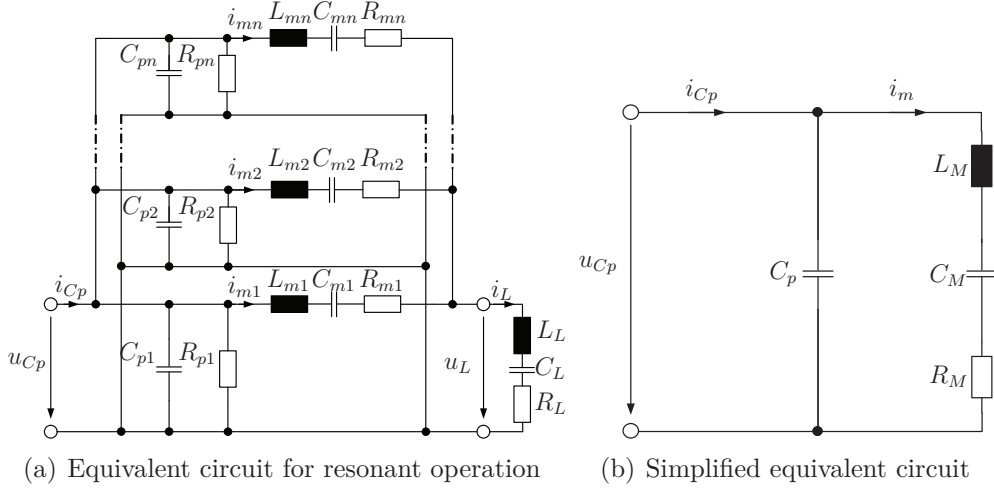


Figure 2.3: Electric equivalent circuit

In Fig. 2.3(a) we see that the mechanical vibration system is described by a grid of parallel branches of  $C_p$ ,  $R_p$  and series-resonant circuit  $L_m$ - $C_m$ - $R_m$ , which represent inertial mass, stiffness and damping of the mechanical characteristics shown in Fig. 2.1. These parallel branches result from the physically paralleled basic piezoelectric elements.

The mechanical load can be approximately modeled by a linear impedance represented by equivalent inductance  $L_L$ , capacitance  $C_L$  and resistance  $R_L$  [Gro02]. By combining the equivalent variable of load with  $L_m$ - $C_m$ - $R_m$  of the actuator, the whole mechanical resonant circuit parameters can be simplified using Eq. 2.4. The equivalent circuit is then represented in Fig. 2.3(b) by using lumped parameters:

$$\begin{aligned}
 L_M &= L_m + L_L \\
 R_M &= R_m + R_L \\
 C_M &= \frac{C_m C_L}{C_m + C_L}
 \end{aligned} \tag{2.4}$$

## 2.1 Modeling of Piezoelectric Actuators

---

Then the simplified resonant circuit is described by the following differential equations:

$$L_M \ddot{q}_M + R_M \dot{q}_M + \frac{1}{C_M} q_M = u_{Cp} \quad (2.5)$$

$$C_p \dot{u}_{Cp} + \dot{q}_M + \frac{u_{Cp}}{R_p} = \dot{q} = i \quad (2.6)$$

Using  $u_{Cp}$ ,  $\dot{q}_M$ ,  $q_M$  as state variables, the state-space model Eq. 2.7 can be derived. We find that the Eq. 2.7 and Eq. 2.3 are identical, when the system matrix variables are replaced by the parameters listed in Tab. 2.1.

$$\begin{bmatrix} \dot{u}_{Cp} \\ \ddot{q}_M \\ \dot{q}_M \end{bmatrix} = \begin{bmatrix} 0 & \frac{-1}{C_p} & 0 \\ \frac{1}{L_M} & -\frac{R_M}{L_M} & -\frac{1}{C_M L_M} \\ 0 & 1 & 0 \end{bmatrix} \begin{bmatrix} u_{Cp} \\ \dot{q}_M \\ q_M \end{bmatrix} + \begin{bmatrix} \frac{1}{C_p} \\ 0 \\ 0 \end{bmatrix} i \quad (2.7)$$

The impedance of the series-resonant circuit  $Z_M(j\omega)$  is derived from the simplified equivalent circuit in Fig. 2.3(b) with

$$Z_M(j\omega) = j\omega L_M + \frac{1}{j\omega C_M} + R_M . \quad (2.8)$$

If the driving frequency of the piezoelectric actuator is the same as the mechanical resonance frequency, the  $L_M$ - $C_M$ - $R_M$  circuit behaves as a purely resistive load  $R_M$  [Mas98]. Paralleling the piezoelectric capacitance  $C_p$  to  $Z_m(j\omega)$ , the admittance  $Y_{Pi}(j\omega)$  is derived in Eq. 2.9, which is used to characterize the piezoelectric actuator subjected to a variation of load and a parameter tolerance of  $C_p$  caused by temperature changes and production lots.

$$\begin{aligned} Y_{Pi}(j\omega) &= j\omega C_p + \frac{1}{Z_M(j\omega)} \\ &= j\omega C_p + \frac{1}{j\omega L_M + \frac{1}{j\omega C_M} + R_M} \end{aligned} \quad (2.9)$$

The mechanical resonance frequency  $\omega_{mr1}$  is calculated by

$$\omega_{mr1} = 1/\sqrt{L_M C_M} . \quad (2.10)$$

## 2. A HIGH-POWER AIRBORNE PIEZOELECTRIC BRAKE ACTUATOR

---

The mechanical part is replaced by  $R_M$  when the piezoelectric actuator is operated at  $\omega_{mr1}$ , so the admittance of the piezoelectric actuator is attained at the mechanical resonance frequency as:

$$Y_{Pi}(j\omega_{mr1}) = j\omega_{mr1}C_p + \frac{1}{R_M} . \quad (2.11)$$

Additionally, two variables the quality factor  $Q_M$  and the admittance ratio  $M$  have shown to be suitable for analyzing the electrical behavior [Sch04a] [Len74] [KF04]:

$$Q_M = \frac{Z_{M0}}{R_M} , \quad (2.12)$$

$$M = \frac{1}{Q_M\alpha_p} = R_M C_p \omega_{mr1} , \quad (2.13)$$

with  $Z_{M0} = \sqrt{L_M/C_M}$  the characteristic impedance and  $\alpha_p = C_M/C_p$  the capacitance ratio.

In order to illustrate the general frequency characteristic of the piezoelectric actuator, the normalized admittance  $Y_{Pi}(j\Omega)$  is derived in Eq. (2.14), in which the normalized frequency  $\Omega = \omega/\omega_{mr1}$  is used:

$$Y_{Pi}(j\Omega) = \frac{\Omega}{Z_{M0}\alpha_p} \cdot \frac{(M\alpha_p^2\Omega + j(M^2\alpha_p^2\Omega^2 + (1 - \Omega^2)(1 + \alpha_p - \Omega^2)))}{M^2\alpha_p^2\Omega^2 + (-1 + \Omega^2)^2} \quad (2.14)$$

The input-admittance frequency characteristic of the piezoelectric actuator equivalent circuit is shown in Fig. 2.4 for different admittance ratios  $M$ .

By applying the normalization  $\Omega = \omega/\omega_{mr1}$ , two normalized resonance frequencies  $\Omega_{mr1}$  and  $\Omega_{mr2}$  can be observed in Fig. 2.4:

$$\begin{aligned} \Omega_{mr1} &= 1 \\ \Omega_{mr2} &= \sqrt{1 + \frac{C_M}{C_P}} = \sqrt{1 + \alpha_p} \end{aligned} \quad (2.15)$$

They represent the series- and the parallel-resonance frequency

$$\begin{aligned} \omega_{mr1} &= 1/\sqrt{L_M C_M} , \\ \omega_{mr2} &= \omega_{mr1} \sqrt{1 + \frac{C_M}{C_P}} = 1/\sqrt{L_M \frac{C_M C_P}{C_M + C_P}} . \end{aligned} \quad (2.16)$$

## 2.1 Modeling of Piezoelectric Actuators

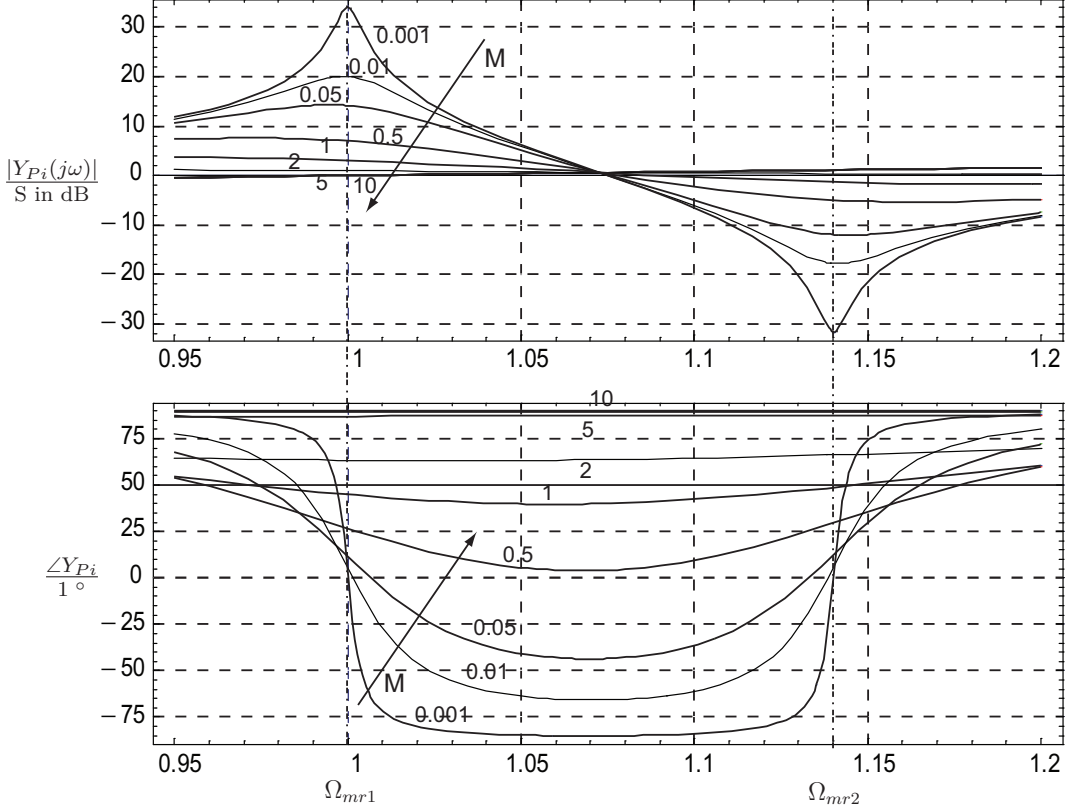


Figure 2.4: Normalized frequency characteristic of a piezoelectric actuator with  $M = 0.001, 0.05, 0.01, 0.5, 1, 2, 5, 10$

The series-resonance frequency  $\omega_{mr1}$  is the resonance frequency of the mechanical equivalent circuit, which is determined only by mechanical parameters. In contrast to  $\omega_{mr1}$ , the parallel-resonance frequency is determined additionally by the capacitance of the piezoelectric ceramics. We should note that  $\omega_{mr1} \ll \omega_{mr2}$ , and at parallel-resonance frequency high input voltage and low input current are required.

In contributions [Sch04a] and [Gro04], the piezoelectric systems are classified into two classes by using the admittance ratio  $M$ . It indicates whether the input behavior of the system is determined by the mechanical resonant part or by the piezoelectric capacity of the actuator.

If  $M < 0.5$  holds, two frequencies exist, at which the imaginary part of the input admittance disappears and  $\angle Y_{Pi}(j\omega) = 0$  holds, see Fig. 2.4. As a result,

## 2. A HIGH-POWER AIRBORNE PIEZOELECTRIC BRAKE ACTUATOR

---

no reactive power is required by the actuator when operated at one of these frequencies. Condition  $M < 0.5$  normally exists for sonotrodes, where the actuator itself forms the oscillating structure.

In contrast at systems with  $M > 0.5$ , the input admittance is capacitive and shows a non-zero imaginary part for all frequencies. This is the case with traveling-wave type ultrasonic motors (TW-USM). For these motors a rather large volume of piezoelectric ceramics is required to excite oscillation of the stator disk, which causes a large piezoelectric capacitance. Consequently, these motors always have a high demand for reactive power.

### 2.2 Multi-Mass Ultrasonic Motor

In an EUREKA technology demonstrator project named PAMELA, the French company SAGEM and its partners demonstrated that high force density can be achieved for a multi-mass ultrasonic motor (MM-USM) by maximizing the stator-rotor contact surfaces [AB03] [SF01].

Considering the advantages of the multi-mass ultrasonic motor (MM-USM), they are expected as novel EMA technology for airborne brakes. Therefore, the EC funded project PIBRAC ([www.PIBRAC.org](http://www.PIBRAC.org)) was started to study, design and test a piezoelectric brake actuator based on a newly developed MM-USM [AAOW06] and its involved power supply and control electronics [LFWB06a] [WFB<sup>+</sup>06]. The yield should be distinct cuts in total weight and peak power demand when compared to brakes actuated by permanent magnet synchronous motors of rotary type.

The rotational motor under construction consists of four stator rings squeezing two rotor discs connected to the shaft. Stators and rotors are cylindrically shaped and mate together along their faces; its detail structure and assembly are shown in Fig. 2.5 and Fig. 2.6.

Each stator ring consists of eight metallic blocks alternating with multilayer piezoelectric actuators, which are placed in tangential and normal direction [AB03] [WFB<sup>+</sup>06]. This structure is excited on its resonating mode, so that each metallic block oscillates in the plane of the ring with a phase shift of  $180^\circ$  versus its neighbors (tangential mode).

## 2.2 Multi-Mass Ultrasonic Motor

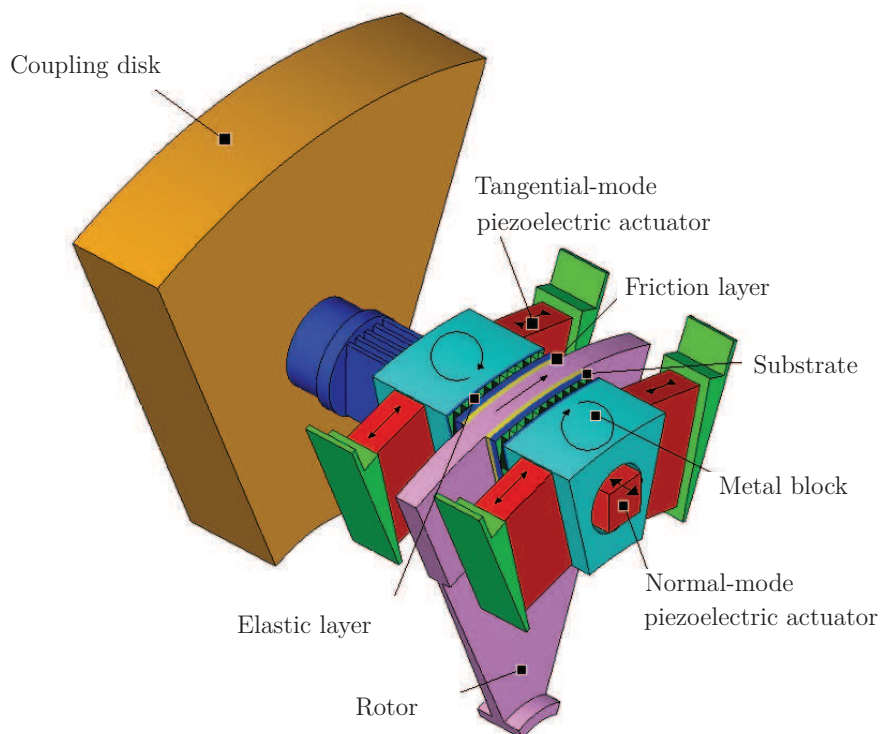


Figure 2.5: Detail structure of multi-mass ultrasonic motor

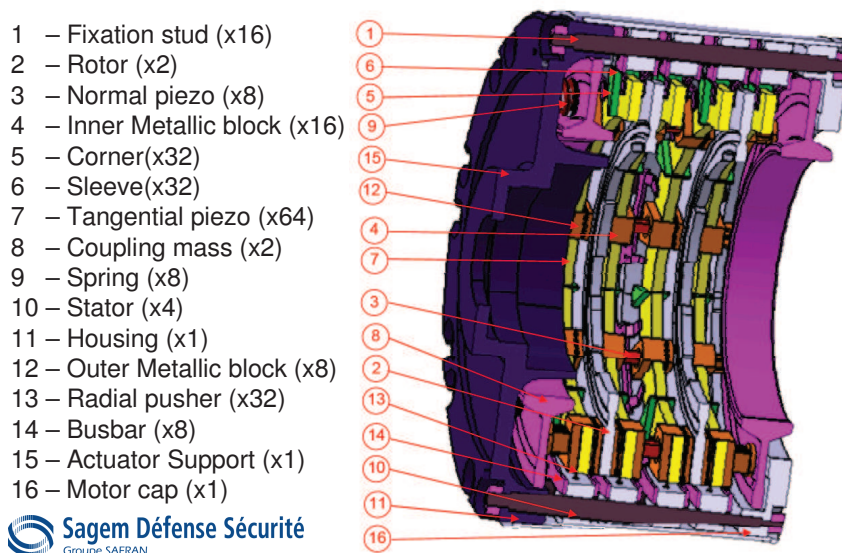


Figure 2.6: Assembly of multi-mass ultrasonic motor [Pib08a]

## 2. A HIGH-POWER AIRBORNE PIEZOELECTRIC BRAKE ACTUATOR

---

The structure including the four stators is able to oscillate also orthogonally to the surface of the stator rings and of the rotor disk (normal mode) at the same frequency as the tangential mode, but with an appropriate phase shift. The superposition of these two oscillation modes results in an elliptical motion of the metallic blocks that thrusts intermittently the rotor disk by utilization of the friction force between stator and rotor, see Fig. 2.7.

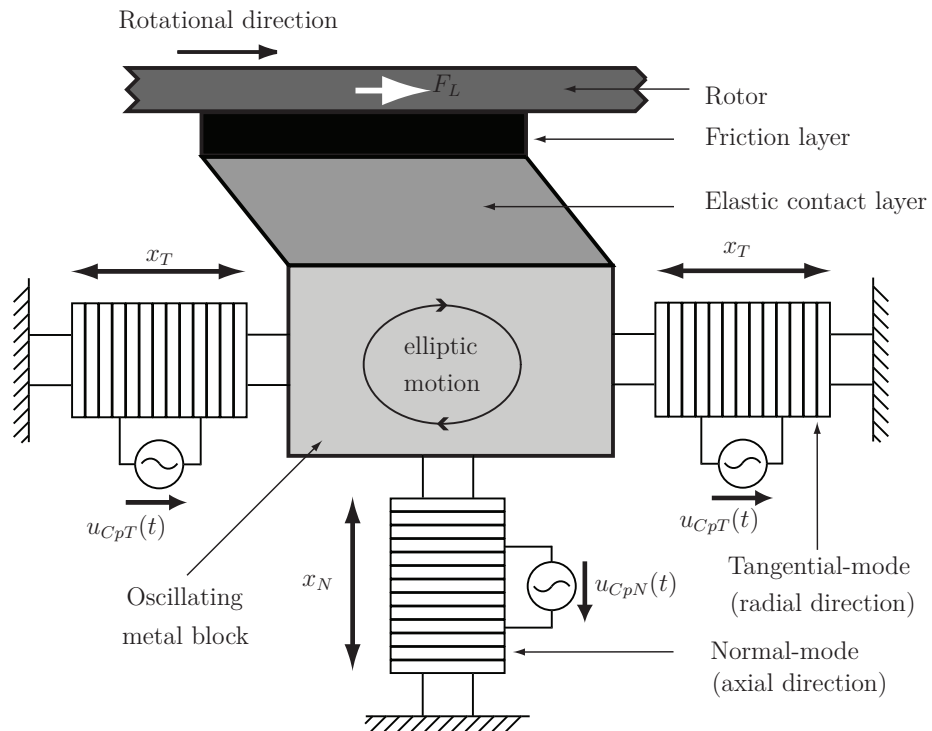


Figure 2.7: Operating principle of multi-mass ultrasonic motors (MM-USM)

This effect drives the rotor shaft thanks to the friction between the metallic blocks and the rotor. However the friction mechanism of piezoelectric motors is a significant reason of the relatively low efficiency of e.g. traveling-wave type ultrasonic motor(TW-USM) [AB03]. In order to reduce the motor losses significantly, a novel layer structure of the stator-rotor contact was developed. It consists of a tribologic layer enabling the frictional contact, and an elastic layer, see Fig. 2.5.

Like a spring-mass system, the elastic layer accumulates some elastic energy, which is later released into kinetic energy. The advantages of such a design

## 2.2 Multi-Mass Ultrasonic Motor

---

compared to the classical TW-USM are twofold: First, the contact area between stator and rotor is enlarged, and second, the friction loss is decreased during the thrust phase. By designing this interface properly, it is possible to double the peak efficiency  $\eta_{peak}$  to about 40 % for a MM-USM, compared to less than 20 % for a classical TW-USM [SF01] [AMC07].

The simplified series-resonant circuit  $L_M$ - $C_M$ - $R_M$  described in Chapter 2.1 is utilized to analyze the power consumption of a MM-USM. For this analysis, some simplifications of the piezoelectric actuator model are required:

- The dielectrical losses within the ceramics represented by  $R_p$  are ignored.
- The actual voltage-fed inverter topologies are firstly not considered, but replaced by a pure AC-voltage source.

Parameters	Tangential mode	Normal mode	Unit	
Block mass $m$	0.1626	0.0642	kg	
Stiffness $c$	6.989 E+09	2.760 E+09	N/m	
Damping $d$	3520	1328	Ns/m	
Force factor $A$	18.88	2.592	N/V	

Table 2.2: Parameters of mechanical part of MM-USM in PIBRAC

Parameters	Tangential mode	Normal mode
$C_p$	176 nF	4.96 nF
$L_M$	456 $\mu$ H	38.2 mH
$C_M$	51 nF	0.6 nF
$R_M$	25 $\Omega$	125 $\Omega$

Table 2.3: Parameters of electrical equivalent circuit of MM-USM

The parameters of the MM-USM for tangential-mode and normal-mode piezo-electric actuators are listed in Tab. 2.2. Values of tangential-mode parameters are calculated from 32 parallel-operated basic tangential motor elements, while normal-mode parameters derive from 16 normal motor elements operated in parallel, which constitute the total MM-USM together with its tangential counterparts.

## 2. A HIGH-POWER AIRBORNE PIEZOELECTRIC BRAKE ACTUATOR

---

In order to transfer the mechanical parameters to equivalent electrical variables, we attain the electrical circuit components listed in Tab. 2.3 using the method described in Chapter 2.1. There the value of the resistor  $R_M = R_L + R_m$  is calculated in case of a rated load of 1.5 kW with an efficiency of 39 %. If the effect of temperature changes is considered, a capacitance variation  $C_p$  of  $\pm 20$  % results.

The mechanical resonance frequency of the MM-USM is equal to the series-resonance frequency of equivalent circuit and derived as:

$$f_{mr1} = \frac{1}{2\pi\sqrt{C_M L_M}} = 33 \text{ kHz} \quad (2.17)$$

From Chapter 2.1 we know that the piezoelectric actuator admittance show an important role for the converter choice [Gro04] [Sch04a].

In Fig. 2.8 and Fig. 2.9 the MM-USM tangential and normal-mode admittance are plotted versus load variation  $R_M$  from no load (only losses in 2 tangential ceramics) to maximum load. At series-resonance frequency the admittance value becomes maximum, because the quality factor  $Q_M$  is decreased with increasing damping  $R_M$ , while the admittance factor  $M$  increases simultaneously.

Tab. 2.4 shows parameters of PIBRAC's MM-USM in comparison with other piezoelectric actuators and motors. As mentioned above in Chapter 2.1, piezoelectric actuators can be classified using the admittance factor  $M$ . But it is more complex here, since that  $M$  of PIBRAC's MM-USM is in a range of 0.3 - 1.0 and varies with the load. It is thus in a position between the two broad typically classes: sonotrodes which show a low damping, as compared to motors characterized by a large damping.

Additionally the load variation for PIBRAC's MM-USM presented in Fig. 2.8 indicates that the  $\angle Y_{Pi}(j\omega)$  curve is larger than  $0^\circ$  degree in condition of large load, and its impedance behavior is similar to an ultrasonic motor with respect to load variation. Hence, the novel motor PIBRAC MM-USM is classified into the group of traveling-wave type ultrasonic motors, rather than sonotrodes for ultrasonic machining.

The effect of temperature changes on the piezo-capacitance is studied and the resulting admittance variation is presented in Fig. 2.10. The power factor of PIBRAC MM-USM at resonance frequency  $\omega_{mr1}$  is larger than the typical

## 2.2 Multi-Mass Ultrasonic Motor

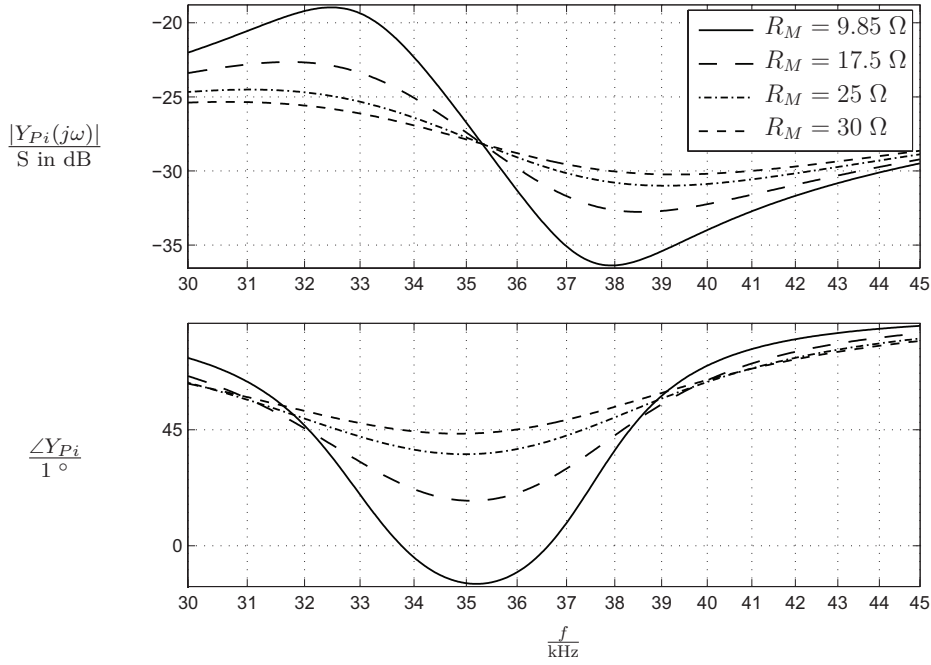


Figure 2.8: Frequency response of admittance of MM-USM tangential mode

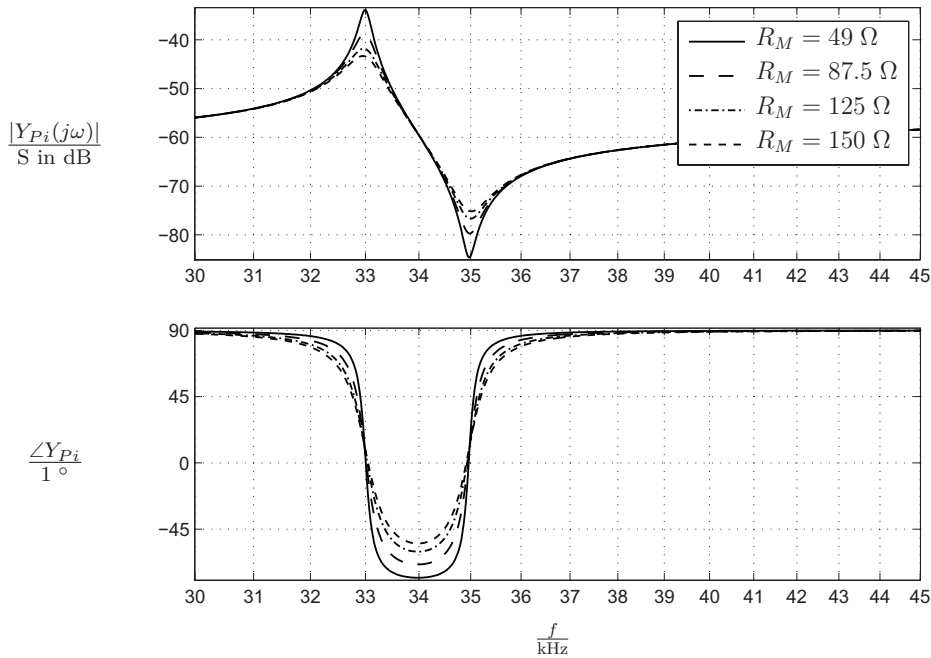


Figure 2.9: Frequency response of admittance of MM-USM normal mode

## 2. A HIGH-POWER AIRBORNE PIEZOELECTRIC BRAKE ACTUATOR

Oscillating unit	$C_p$ [nF]	$C_M$ [nF]	$L_M$ [mH]	$R_M$ [ $\Omega$ ]	$f_{mech}$ [kHz]	$\alpha_p$	$Q_M$	$M$	$\varphi_{max}$ [ $^\circ$ ]
Bonding sonotrode <sup>1</sup>	1.3	0.26	11.03	25.05	94.0	0.2	260	0.019	88.90
Atomising sonotrode <sup>1</sup>	10	0.005	12540	158.4	20.1	5e-4	1e4	0.2	78.23
Tooling sonotrode <sup>1</sup>	20	0.2	333.1	102.0	19.5	0.01	400	0.25	75.07
Travelling wave type piezoelectric motor <sup>1</sup>	7.5	0.0225	608.9	1828	43.0	0.003	90	3.7	-73.77
PAMELA2 <sup>2</sup>	1750	7	9	16	20.0	0.004	70	3.57	-74.06
PIBRAC	176	51	0.456	25	33	0.29	50	1.0 - 0.36	-32.5

- 1 and 2: source [Sch04a]  
 2 PAMELA2 motor: 32 basic motor elements in parallel, only tangential mode  
 3 PIBRAC motor: 32 basic motor elements in parallel, only tangential mode

Table 2.4: Comparison of different applications of piezoelectric actuators

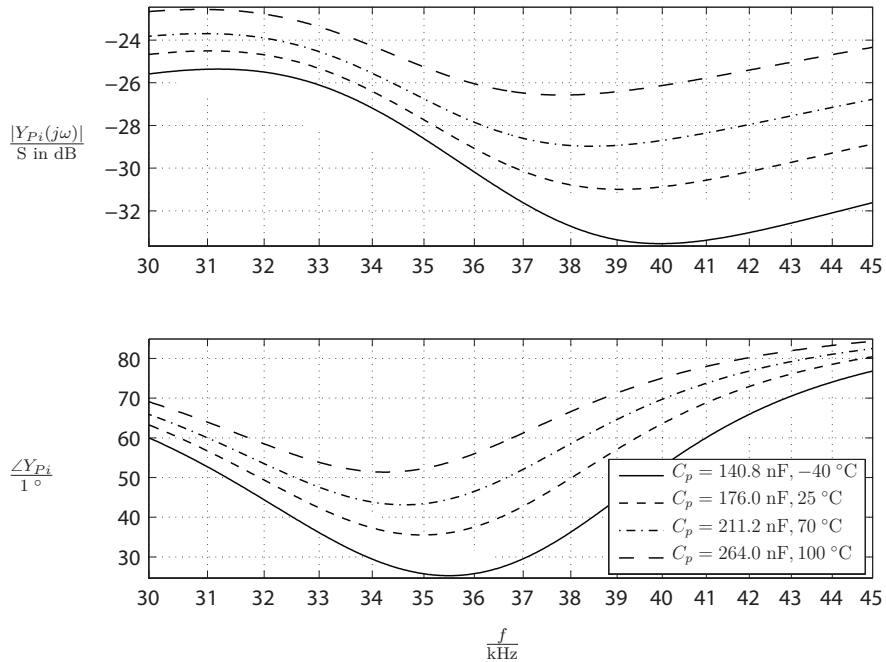


Figure 2.10: Frequency response of admittance of MM-USM tangential mode with varying  $C_p$

## 2.3 Power Consumption of a Brake Actuator

traveling-wave type motor or for the former PAMELA2 MM-USM [SF01], but still a large reactive power is to be produced.

Consequently, an increase of the required motor reactive power from some 600 VA up to 2 kVA is one effect of this temperature variation. Thus a reactive power compensation is accordingly an important aspect for the design of the power supply, due to its large impact on objectives such as weight, volume and electrical efficiency.

## 2.3 Power Consumption of a Brake Actuator

The brake actuator is operated in four modes as shown in Fig. 2.11 as: approach, load application, retraction and stand-by [Pib06a].

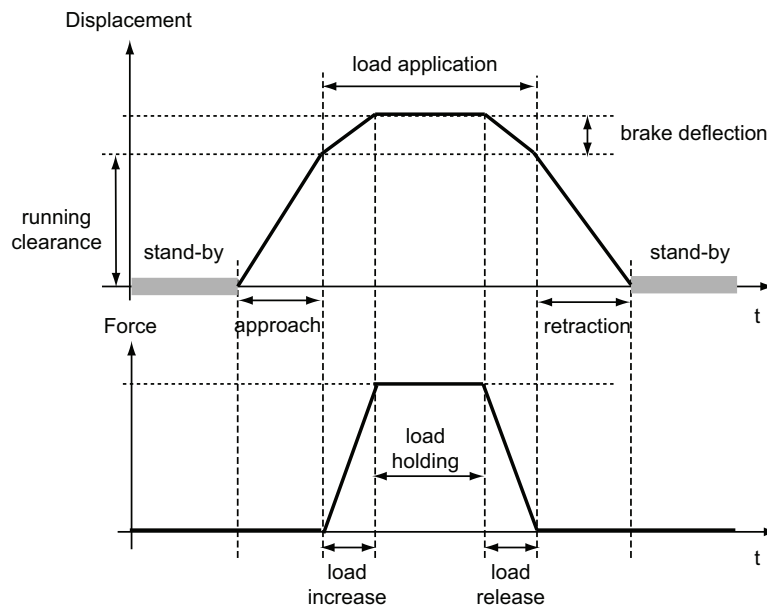


Figure 2.11: PIBRAC operating profile

The power consumption diagram of a PIBRAC actuator with MM-USM during this operation is illustrated in Fig. 2.12. It consists of active-power balance, reactive-power balance, supplemented by initial power requirement during the system start delivered by the power inverter to the brake actuator.

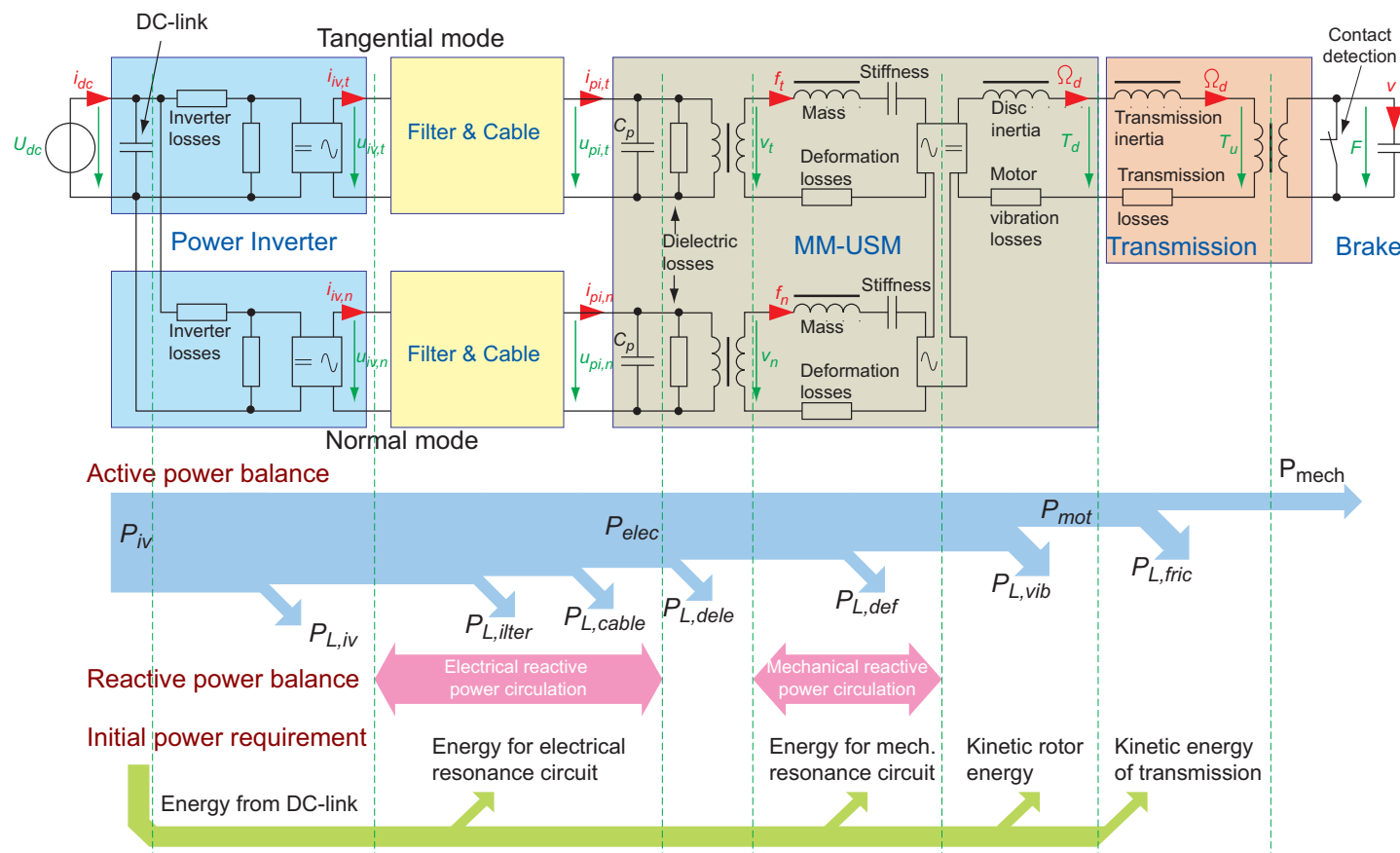


Figure 2.12: PIBRAC power balance

## 2.3 Power Consumption of a Brake Actuator

---

For best understanding the dynamic behavior of the PIBRAC actuator and best view of this effect, all of the mechanical variables are represented by equivalent electrical components.

The power consumption of the brake actuator depends heavily on the type of ABS (Anti-skid Brake Systems) modulation and on the mode of operation. The peak power consumption occurs at the beginning of the approach phase of the brake. The total power consumption can be calculated by superposition of the steady-state (static) and the dynamic power consumption.

Because the MM-USM performs the coupling between mechanical and electrical “building blocks” of the main power path, ratings concerning efficiency and operating condition are important in order to enable specification setting of electrical parameters. Hence, it is necessary to know the required motor power, before a power supply is developed.

The required power of the motor from the power supply can be determined as:

$$P_{elec} = P_{L,dele} + P_{L,def} + P_{L,vib} + P_{mot} , \quad (2.18)$$

where  $P_{mot}$  is the required mechanical power delivered to the brake through the transmission, and the three kinds of losses include dielectric losses ( $P_{L,dele}$ ), piezo-electric deformation losses ( $P_{L,def}$ ) and vibration conversion losses ( $P_{L,vib}$ ).

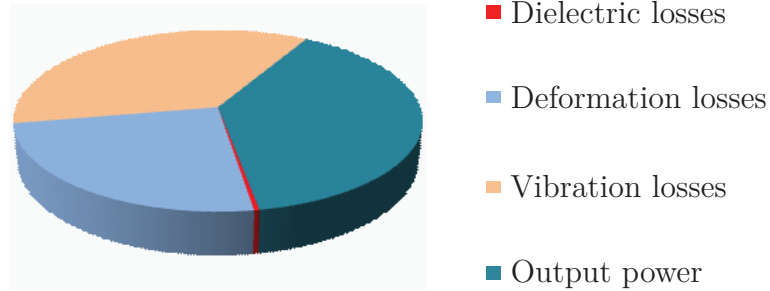


Figure 2.13: Power losses of MM-USM

For a motor output power of 550 W, the following power losses are listed in Tab. 2.5 [Pib06b]. The peak efficiency of the PIBRAC motor is with 39 % very low, compared to an EMA motor efficiency, which is generally about 90 %. Thus we have a considerable degradation of efficiency in this building block of the system.

## 2. A HIGH-POWER AIRBORNE PIEZOELECTRIC BRAKE ACTUATOR

MM-USM output power		550 W	
Losses	Dielectric losses	5 W	0.35 %
	Deformation losses	347 W	24.61 %
	Vibration losses	508 W	36.03 %
Total MM-USM losses		508 W	
Required electrical power		1410 W	
MM-USM efficiency			39.01 %

Table 2.5: Power consumption of MM-USM [Pib06b]

### 2.4 Requirement of Power Supply and Control

Fig. 2.14 presents the simplified PIBRAC driving scheme, where both driving AC voltages ( $u_{CpT}$  and  $u_{CpN}$ , see Fig. 2.7) have to be adjusted as requested by the outer control loop [Pib07a] [Pib07b]. Hence, the task of the power supply is to feed the MM-USM with appropriate voltages with respect to three parameters:

1. amplitude: exciting expected oscillating amplitude.
2. frequency: matching the excitation frequency to the mechanical resonance frequency.
3. phase shift: yielding best torque/thrust.

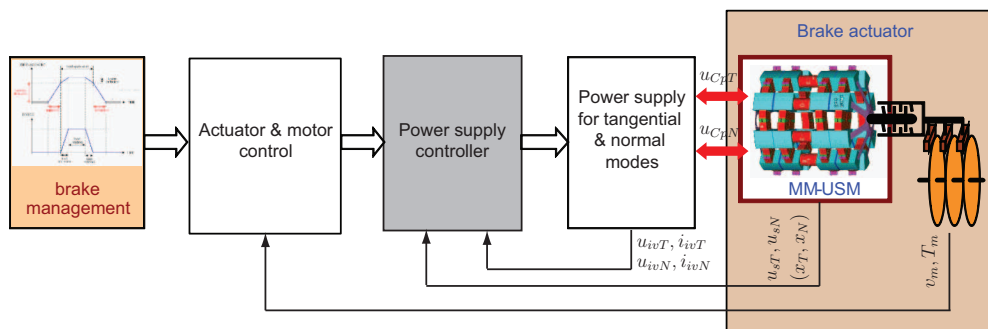


Figure 2.14: Power supply and control system structure

Variations of the frequency are expected, however, only in a narrow band around the nominal mechanical resonance frequency. In practice a superposition of a resonance-frequency shift and the reduction of the mechanical oscillation can

## 2.4 Requirement of Power Supply and Control

---

be observed, and in order to ensure setting the optimal operating point, the resonance frequency must be tracked and controlled [Sch04a] [Mas98].

The considered power supply is composed of inverter and filter, the inverter can only be designed individually, because the output filter is inserted between inverter and motor for various reasons.

Concluding from the above discussion, the challenge of an appropriate power-supply design arises from following reasons:

- Due to the piezoelectric effect, the output filter of a power supply is highly influenced by the mechanical oscillation system. A closer inspection reveals that the electrical behavior depends on the frequency-dependent interactions between the MM-USM and the load, i.e. the mechanical subsystem of the brake.
- Piezoelectric actuators are known to exhibit a distinct capacitive behavior. The piezoelectric capacitance should be part of the output filter, but the motor capacitance originating from the large number of piezoelectric elements of the MM-USM varies with temperature, thus is also dependent on operating conditions.
- Both active power and reactive power are to be delivered by the power supply to the MM-USM. The high operating frequency results in high switching losses of the power supply and in lots of EMI issues. Thus, the power ratio and the efficiency are determined by the working condition of ultrasonic motor.

Using power-supply terminology, the aforementioned circuit should provide a robust and highly dynamic operating behavior, so that a variation of the piezoelectric capacitance, caused by changing operating points, is taken care of in a properly designed control range. Of course, design of control and filter should also take into account the above mentioned requirements.

Normally the mechanical resonance frequency is designed in a range of 20 to 40 kHz. The fundamental frequency of the power inverter can be chosen in the proximity of the resonance frequency of the mechanical vibration  $\omega_{mr1}$ , in order to reduce the stress of the mechanical part and the high supply voltage. This

## **2. A HIGH-POWER AIRBORNE PIEZOELECTRIC BRAKE ACTUATOR**

---

decides about the switching frequency of the power inverter. Hence it is important to choose the appropriate modulation method, because the switching frequency determines the total harmonic distortion (THD), losses and EMI, and has great impact on volume and weight of the filter components.

## Chapter 3

# Power Supply Topologies for High-Power Piezoelectric Actuators

According to the discussion in Chapter 2, a piezoelectric ultrasonic motor is constructed of piezoelectric actuators, and the power supply of a ultrasonic motor is composed by the power supplies for each piezoelectric actuator and their control unit. Therefore topologies of power supply for ultrasonic motor are based on power-supply topologies for high-power piezoelectric actuators.

First section of this chapter will summarize the state-of-the-art of power supplies for piezoelectric actuators, and further it will focus on the state-of-the-art of power supplies for medium to large power (several 100 W to several kW) resonant-mode piezoelectric actuators, which means that they are operated in the near of their mechanical resonance frequency.

In the second section an advanced novel concept of a power supply consisting of a PWM controlled inverter and a LLC-type filter is proposed to supply piezoelectric actuators in the power range of some kW.

### 3. POWER SUPPLY TOPOLOGIES FOR HIGH-POWER PIEZOELECTRIC ACTUATORS

---

## 3.1 State-of-the-Art of Power Supplies for Piezoelectric Actuators

### 3.1.1 Classification of Power Supplies for Driving Piezoelectric Actuators

As mentioned above in previous Chapter 2.4, the power supply consists of two basic parts: inverter and filter circuit. The specification of power supplies will change, if the combinations of these basic components are varied, or when different modulation schemes for the inverter are employed.

According to the operating mode of piezoelectric actuators, its power supplies can be classified broadly into quasi-static-type and resonant type. A structure diagram shows the classification of these supplies shown in Fig. 3.1.

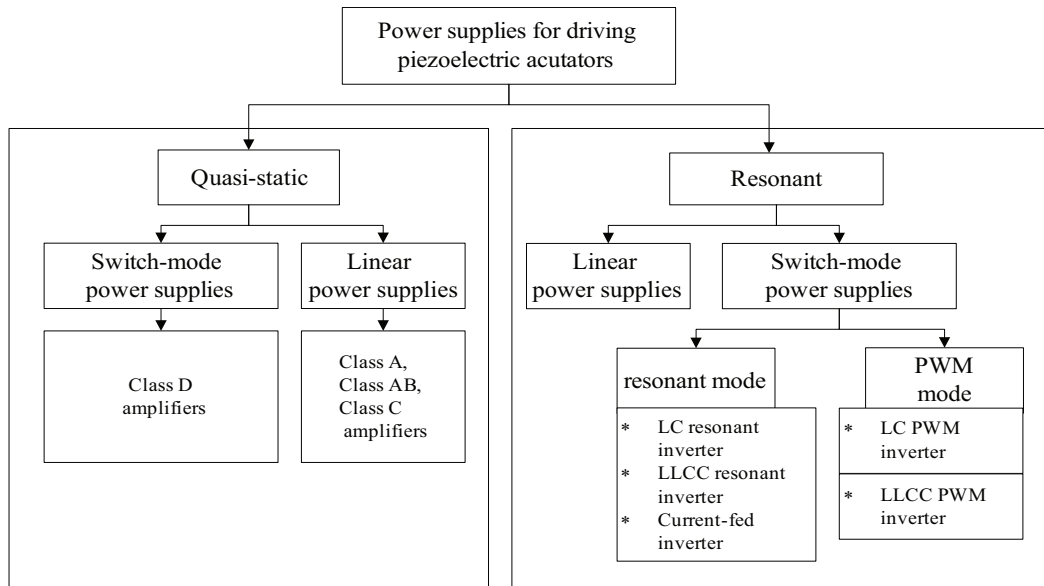


Figure 3.1: Classification of power supplies for driving piezoelectric actuators

The quasi-static-type power supplies are applied in particular with large piezoelectric actuators with high capacitance. These actuators are operated far below their first resonant frequency with high dynamic, for example, in the diesel injection technology. In literature such as [Gna05] [CU01] [STJ01] power-supply topologies and its control concepts are described in detail.

### 3.1 State-of-the-Art of Power Supplies for Piezoelectric Actuators

Different to quasi-static-type power supplies, the output voltage of resonant-type power supplies is regulated near to the mechanical resonance frequency of the piezoelectric actuators. Due to the advantages of resonant-mode piezoelectric actuators mentioned in Chapter 2, this work focuses on the resonant-type power supplies.

Due to the notably large energy dissipation of linear amplifiers, large heat sinks are required. So they do not qualify for weight-sensitive applications, especially if an electric isolation is a must. In comparison, switching power amplifiers usually termed as switching power converters are possible to achieve high efficiency and power density. Hence they are very commonly used as power supplies of today's hand-held devices, micro- and optoelectronic applications e.g. [LZS<sup>+</sup>02] [LZVL02] [ZL98] [ADC<sup>+</sup>00].

Therefore the switching power amplifiers are considered as promising alternatives for driving resonantly operated piezoelectric actuators and ultrasonic motors. The development of switching power amplifiers has to be investigated to employ different industry applications [MKFG95] [LDL99] [LLBC01] [SJ00] [JQ02] [SBT04].

When a piezoelectric actuator is operated at the mechanical resonance frequency, the equivalent electrical circuit can be simplified to a pure resistor  $R'_p = R_M$  shown in Fig. 3.2 [Gro04] [Sch04a]. This  $C_p - R'_p$  is used in the following investigation to represent the piezoelectric actuator.

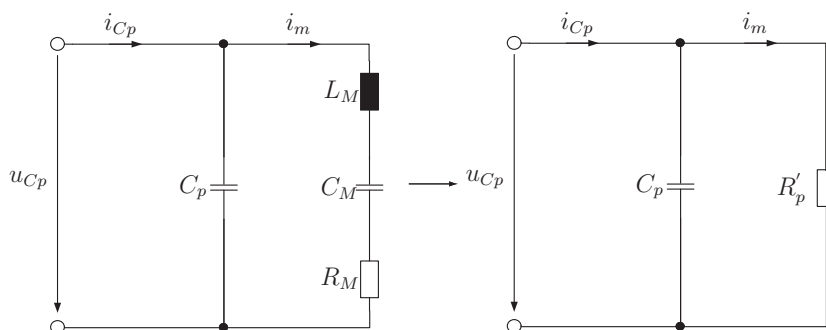


Figure 3.2: Simplified electric equivalent circuit when  $\omega_{OP} \approx \omega_{mech}$

### 3. POWER SUPPLY TOPOLOGIES FOR HIGH-POWER PIEZOELECTRIC ACTUATORS

---

#### 3.1.2 Resonant Switching Power Supply for Driving High-Power Piezoelectric Actuators

In applications of some tens to hundreds Watts, resonantly operated power supplies were developed to drive ultrasonic motors. Two types of resonant-converter concepts, which consist of a LC-type or a LLC-type resonant circuit, were used to supply piezoelectric motors and designed to operate in the resonance frequency range of the motor [Gro04] [LDH99]. The essential difference between these exists in the structure of the output resonant circuits.

##### 3.1.2.1 Inverter Topologies and Square-wave Modulation

###### A. Inverter Topologies

Based on the operating principle of piezoelectric actuators, the topology chosen is a single-phase inverter as illustrated in Fig. 3.3.

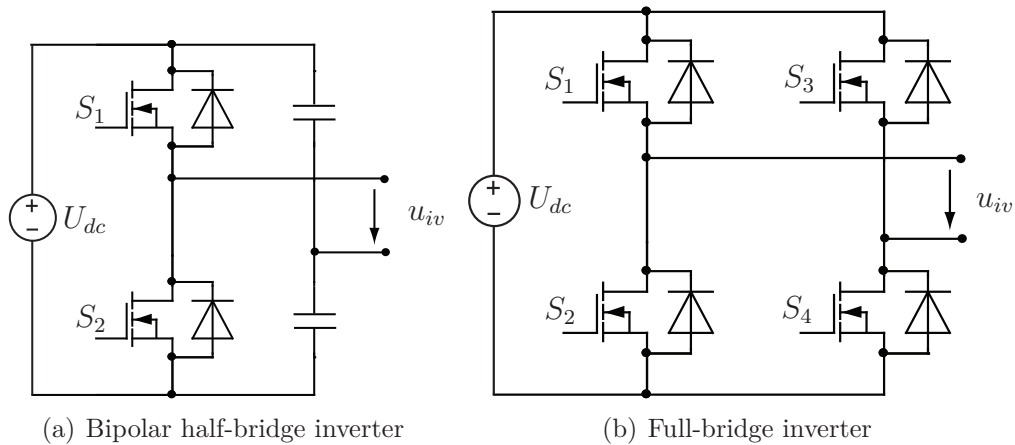


Figure 3.3: Inverter circuits

The half-bridge inverter is composed only by one switching leg with two switch components, and generates bipolar output voltage. The half-bridge inverter could be followed by a transformer to provide galvanic isolation and required voltage ratio transformation.

The limitation of this topology is that the output voltage  $u_{iv}(t)$  amplitude is only half of the input voltage. Consequently, the two switching components must

### 3.1 State-of-the-Art of Power Supplies for Piezoelectric Actuators

---

handle two times of current than those of the full-bridge inverter with same output power. So the half-bridge topology is normally applied at low-power applications.

A full-bridge inverter shown in Fig. 3.3(b) consists of four controllable switches, used preferably in applications with a power consumption in the range of several kilowatts. The advantage of this topology is that three levels of output voltage level are generated by turning on and off the diagonal switches at different time and using the free-wheeling over the internal body-diodes without increasing the voltage stress of components, which equals the input DC-link voltage. Consequently, the possible switching frequency could be as more than 500 kHz with help of MOSFETs as switching devices. Moreover, some kinds of modulation schemes were studied already for this topology in order to utilize switching devices most efficiently and economically.

In case an electrical isolation is required, a transformer is located at the output side. Due to bipolar excitation, the magnetic core of the transformer can be utilized to a higher extent; but the problem of saturation caused by control unsymmetries has to be taken into account.

#### ***B. Square-wave Modulation***

In the publications [MKFG95] [LDL99] [SFG00] the full-bridge and the half-bridge topologies are employed using square-wave modulation for the inverter circuit. To control the output voltage amplitude and its frequency corresponding to the desired working frequency of the piezoelectric motor, the switching transistors are driven with a proper gating pulse sequence shown in 3.4, in which  $\alpha_1$  is the turn-on phase angle of driver signal  $S_1$  and  $S_2$  ( $S_1 = \bar{S}_2$ ), and  $\alpha_2$  is the turn-on phase angle of driver signal  $S_3$  and  $S_4$  ( $S_3 = \bar{S}_4$ ); then the difference  $\alpha_2 - \alpha_1$  is known as the phase shift between drivers signals of  $S_1$  and  $S_3$ .

The driver signals  $S_1$  and  $S_3$  are generated by comparing two sinusoidal signals  $u_{sin1}(t)$  and  $u_{sin2}(t)$  with a triangular carrier signal  $u_{tri}(t)$  presented in Eq. 3.1, Eq. 3.2 and Eq. 3.3. The electrical stress and switching losses of the switching

### 3. POWER SUPPLY TOPOLOGIES FOR HIGH-POWER PIEZOELECTRIC ACTUATORS

---

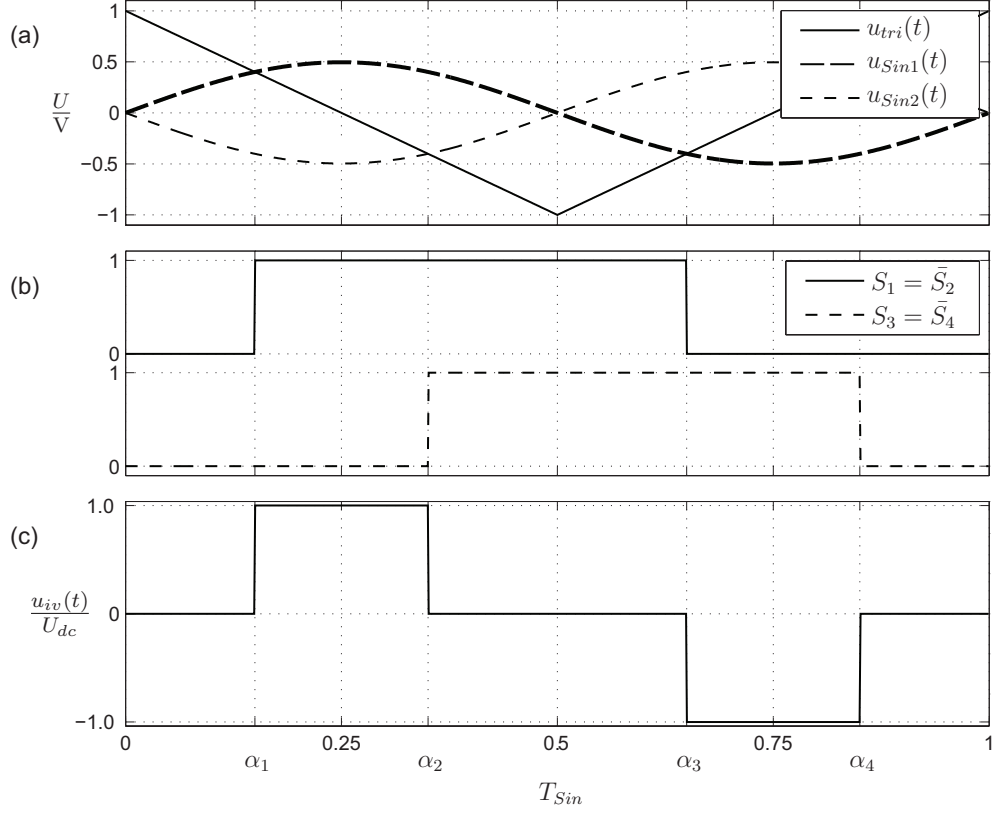


Figure 3.4: Square-wave modulation  
(a) Sinusoidal signals and triangular carrier signal  
(b) Driver signals  
(c) Normalized inverter output voltage

transistors are allotted equally using this modulation.

$$u_{sin1}(t) = u_{set} \sin\left(\frac{2\pi}{T_{sin}}t\right) \quad (3.1)$$

$$u_{sin2}(t) = -u_{set} \sin\left(\frac{2\pi}{T_{sin}}t\right) \quad (3.2)$$

$$u_{drei}(t) = \begin{cases} \left(1 - \frac{4}{T_{sin}}t\right) \text{ V} & 0 \leq t < \frac{T_{sin}}{2} \\ \left(-3 + \frac{4}{T_{sin}}t\right) \text{ V} & \frac{T_{sin}}{2} \leq t < T_{sin} \end{cases} \quad (3.3)$$

In Eq. 3.1, Eq. 3.2 and Eq. 3.3,  $u_{set}$  is the normalized set value of the fundamental component of the inverter output voltage. The RMS amplitude of the fundamental component is varied by phase shift  $\alpha_2 - \alpha_1$  presented in Fig.

### 3.1 State-of-the-Art of Power Supplies for Piezoelectric Actuators

3.5(a), and is calculated as:

$$\hat{U}_{1iv} = \frac{4}{\pi} \cos(\alpha_1) \quad (3.4)$$

In order to trace the voltage set signal, the variation of phase shift  $\alpha_1$  is calculated by the modulation of the respective sinus signal amplitudes. Note that as shown in Fig. 3.5(b) there is a nonlinear relationship between  $U_{1iv}$  and set value  $u_{set}$ .

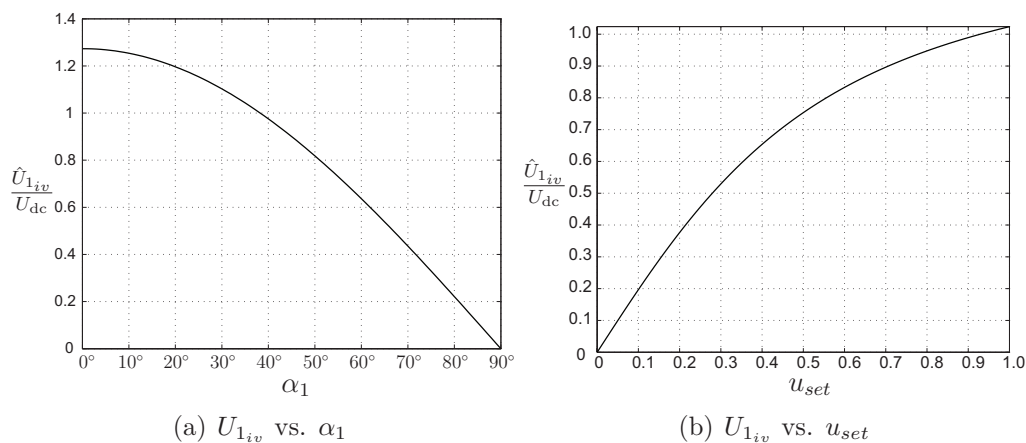


Figure 3.5: Characteristic curve of fundamental component

We see the pulse number  $n_p$  of voltage  $u_{iv}(t)$  is two per period, while the switching transistors  $S_1$ - $S_4$  are turned on and off only one time per period. Moreover the ZVS (zero voltage switched) turn-on operation can be achieved for some operating conditions. Consequently, switching losses of the inverter are low on one hand, but on the other hand the total harmonic distortion cannot be neglected. This is indicated by the spectrum analysis of the inverter output voltage shown in Fig. 3.6.

Because the inverter output voltage  $u_{iv}(t)$  is a periodic symmetric signal, and satisfies the condition of  $u_{iv}\left(\frac{2\pi}{T_{sin}}t + \pi\right) = -u_{iv}\left(\frac{2\pi}{T_{sin}}t\right)$ , all of the even harmonic components are zero. It is important to see that the 3<sup>rd</sup>, 5<sup>th</sup>, 7<sup>th</sup>, 9<sup>th</sup> and 11<sup>th</sup> harmonic frequency dominate the harmonic distortion in the spectrum diagram, which must be damped by a filter in order to supply the piezoelectric motors with a sufficiently pure sinusoidal voltage at the fundamental frequency  $F_0$ . It

### 3. POWER SUPPLY TOPOLOGIES FOR HIGH-POWER PIEZOELECTRIC ACTUATORS

---

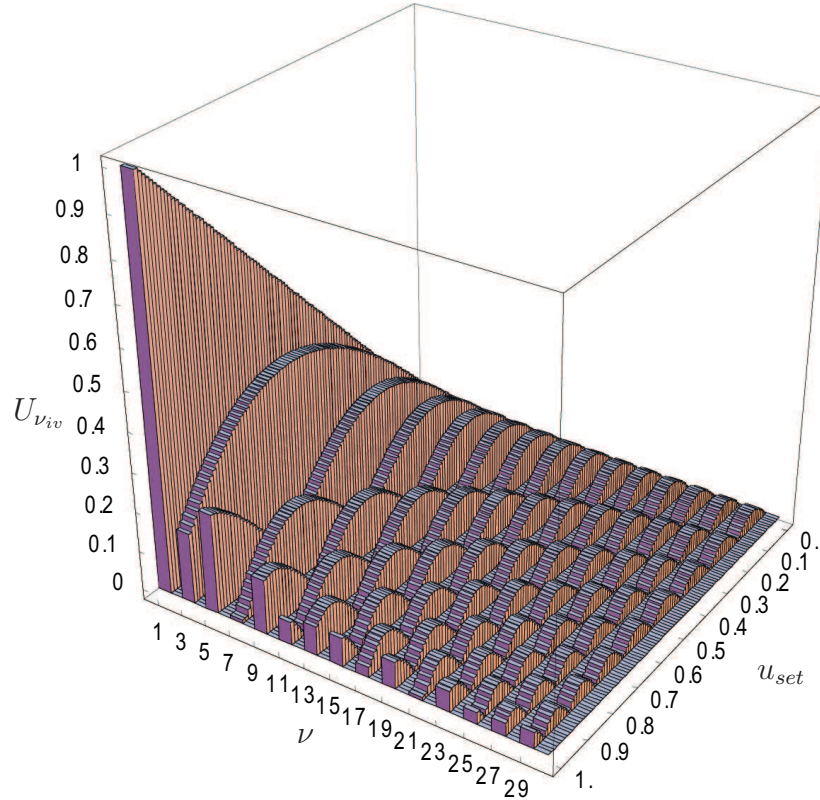


Figure 3.6: Frequency spectrum of inverter output voltage using square-wave modulation

aims on increasing the life-cycle of piezoelectric elements and avoiding undesired oscillations.

In order to satisfy the filter requirements, a large variety of filter circuits were employed, wherein the series and parallel LC filter, LCC, LLC and LLCC circuit were investigated in various contributions [LZS<sup>+</sup>02] [LFWB06b] [MSG97] [LÖ6]). The analysis of LC and LLCC-resonant inverter are described in the next section.

#### 3.1.2.2 LC-Resonant Inverter

LC-resonant converters shown in Fig. 3.7 are investigated and utilized to supply piezoelectric actuators for different applications [Sch04a]. LC-resonant converters are defined by the form of the output filter, consisting of an additional series inductor  $L_s$  and a parallel capacitor supplied here as the equivalent piezoelectric capacitor  $C_p$  by the piezoelectric actuator [MKFG95] [CJ93].

### 3.1 State-of-the-Art of Power Supplies for Piezoelectric Actuators

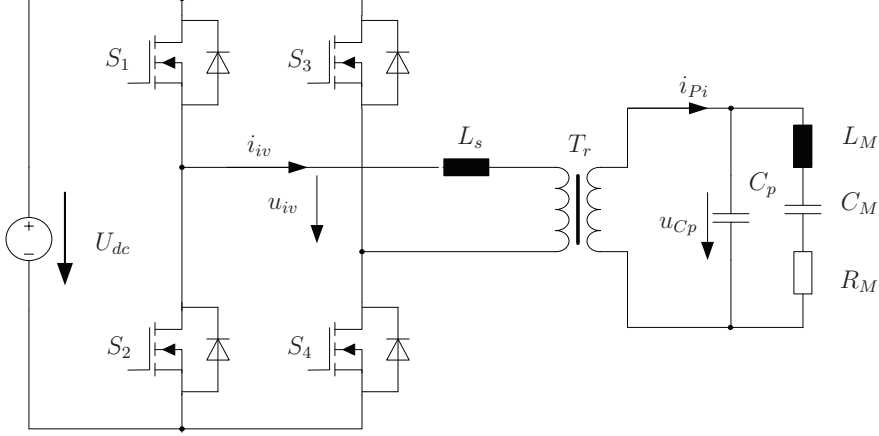


Figure 3.7: LC-resonant converter

The series inductor  $L_s$  has two tasks. First it forms together with the piezoelectric capacitor  $C_p$  a second-order low-pass filter and second it limits the current of the inverter. The electrical resonance frequency is calculated as:

$$f_{elr} = \frac{1}{2\pi\sqrt{L_s C_p}} \quad (3.5)$$

Using LC-resonant converters to drive piezoelectric actuators, the mechanical resonance frequency  $f_{mr1}$  of the actuator is set to be the same as the switching frequency  $f_s$  of the resonant converter, and it is considered to attain the proper voltage transfer ratio of filter input and output. However, the electrical resonance frequency  $f_{elr}$  is located lower as  $f_{mr1}$  by a value of  $\Delta f = 4 - 6$  kHz, in order to keep from sensitizing behavior of piezoelectric actuator when exciting the LC-resonant filter at  $f_{mr1}$  [Mas98].

$$f_{mr1} = f_{elr} + \Delta f \quad (3.6)$$

In typical applications the piezoelectric actuator is given, whereby the nominal value of  $C_p$  is determined. After determining the value of  $C_p$ , the series inductor is calculated by the following equation:

$$L_{s,LC} = \frac{1}{C_p(2\pi(f_{mr1} - \Delta f))^2} \quad (3.7)$$

In the target application of the PIBRAC motor, the parameters of the piezoelectric actuator built for tangential mode are given in Tab. 3.1.

### 3. POWER SUPPLY TOPOLOGIES FOR HIGH-POWER PIEZOELECTRIC ACTUATORS

---

Parameter		Value
Mechanical resonance frequency	$f_{mr1}$	33000 Hz
Piezoelectric equiv. capacitor	$C_p$	176 nF
Electrical resonance frequency	$f_{elr}$	29 kHz
Series inductor	$L_s$	171.1 $\mu$ H

Table 3.1: Components for the design of LC-resonant converter

The impedance of the LC-resonant circuit calculates as:

$$Z_{LC}(s) = sL_s + \frac{1}{sC_p + 1/Z_m(s)}, \quad (3.8)$$

with the piezoelectric motor being represented by a simple equivalent resistive load  $R'_p$  at resonant state. So the voltage transfer function of LC filter is:

$$G_{LC}(s) = \frac{u_{C_p}(s)}{u_{iv}(s)} = \frac{1/sC_p + 1/Z_m(s)}{sL_s + \frac{1}{sC_p + 1/Z_m(s)}} \quad (3.9)$$

The frequency response is shown in Fig. 3.8, keeping in mind that the voltage  $u_{C_p}(t)$  is influenced by variations of the equivalent mechanical load  $R'_p$  and capacitance  $C_p$ , because the operating frequency is near to the resonance frequency [Mas98]. Hence the robustness of the voltage transfer function of the LC filter is very poor.

Obviously the variations of these parameters will detune and deteriorate the filter characteristics as shown in Fig. 3.8. Practically  $C_p$  varies in a range of  $\pm 30\%$  influenced by temperature, production spreading etc.

From the spectrum in Fig. 3.6, we know that the first appearing harmonic component is the 3<sup>rd</sup> harmonic. In order to attain a well sinusoidal AC-voltage  $u_{C_p}(t)$ , it is necessary to realize high suppression of low-order harmonics. As the frequency response of LC-type filters decays with a ratio of  $-40$  dB/dec at frequency higher than 40 kHz, an attenuation of  $-15$  dB compared with the fundamental component can be attained. But one drawback cannot be avoided, that  $|G_{LC}|$  is reduced with accounts of  $-3.5$  dB at actuator operating frequency  $f_{Op}$ , therefore the inverter output voltage must be regulated higher than the required piezoelectric actuator voltage, in order to attain satisfactory mechanical oscillation amplitude.

### 3.1 State-of-the-Art of Power Supplies for Piezoelectric Actuators

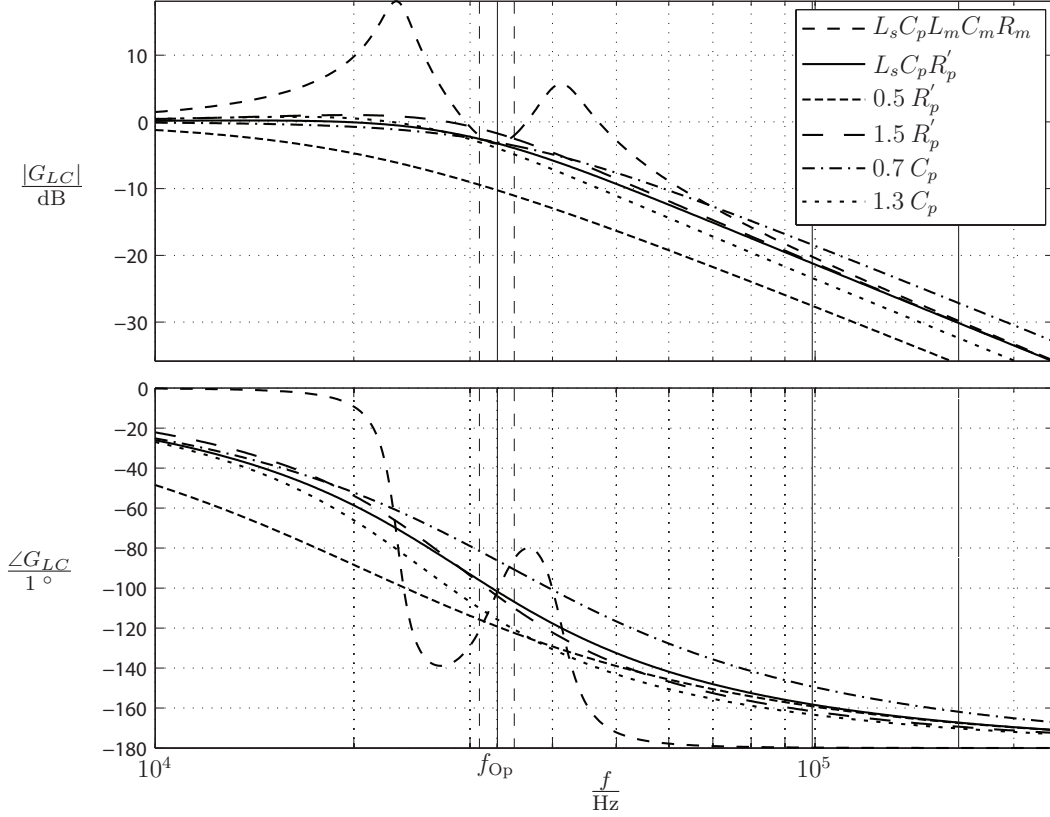


Figure 3.8: Frequency response of LC-resonant converter

Another disadvantage of a LC-type filter is that its transfer function is very sensitive to the variation of filter and load parameters. So it is difficult to control a stable actuator voltage. One solution presented in [KSF02] is adding a discrete capacitor parallel to  $C_p$  in order to reduce detrimental effects. This solution stabilizes the filter characteristic and results in a more robust operating behavior on the one hand. However, it is paid with higher currents and higher reactive power charging the filter components on the other hand. This again causes the usage of bulky and expensive inductors.

The admittance diagram of a resonant LC-type filter is presented in Fig. 3.9 indicating the variation of  $C_p$  and  $R'_p$ . Note that the phase angle  $\angle Y_{LC}$  is near to  $\varphi = -60^\circ$  at the operating frequency  $f_{Op}$  ( $f_{Op} = f_{mr1}$ ) and the condition is becoming worse with decreasing  $R'_p$ . This means there is large phase shift between inverter output voltage  $u_{iv}(t)$  and current  $i_{iv}(t)$ , which results in a large reactive power to be delivered to the LC filter, which goes along with increasing inverter

### 3. POWER SUPPLY TOPOLOGIES FOR HIGH-POWER PIEZOELECTRIC ACTUATORS

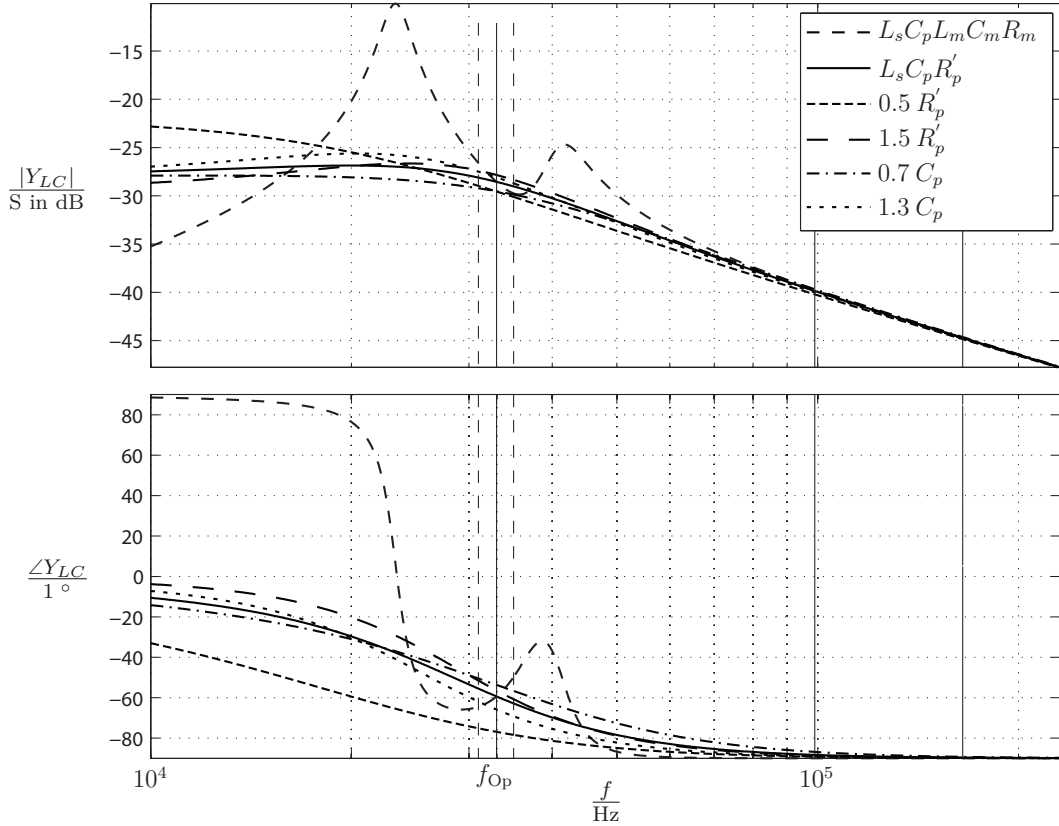


Figure 3.9: Admittance diagram of resonant controlled LC-type filter

losses, while the power factor is reduced.

#### 3.1.2.3 LLCC-Resonant Inverter

Consequences of varying piezoelectric capacitances are investigated in [Sch04a], which led to the development of a resonant inverter with LLCC-type filter [SF01] [KSF02] [SFG00]. Originally it was introduced in [LDL99] [LDH99].

The schematic circuit of a LLCC-type filter is shown in Fig. 3.10. Contrasting to the LC-type filter in the LLCC-type filter a series-resonant circuit consisting of capacitor  $C_s$  and inductor  $L_s$  and a parallel-resonant circuit consisting of inductor  $L_p$  and equivalent piezoelectric capacitor  $C_p$  are required.

The modulation principle of the LLCC-resonant converter corresponds with that of the LC-resonant converter, then the control of transistors and therefore the output signal of the inverter stage are identical.

### 3.1 State-of-the-Art of Power Supplies for Piezoelectric Actuators

A detailed comparison in [Sch04a] revealed that the LLC-resonant inverter shows advanced characteristics and best-suited properties in respect to efficiency, stationary and dynamic behavior, control and commissioning efforts, except volume and weight aspects for ultrasonic resonating actuators with low electromechanical quality factor  $Q_m$ .

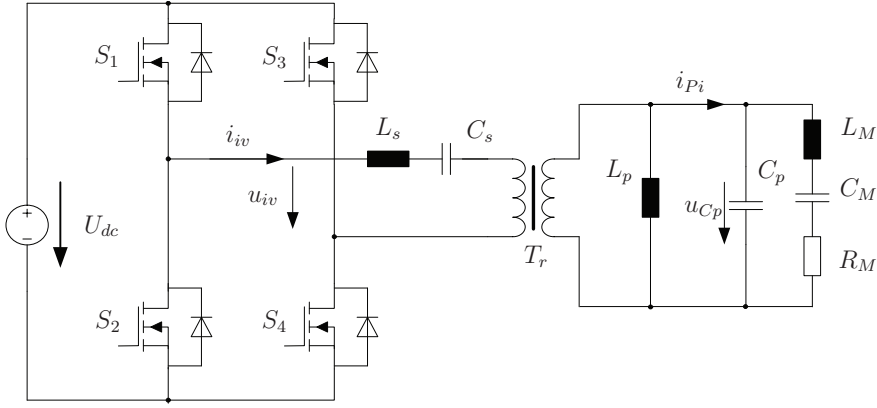


Figure 3.10: LLC-resonant inverter

As mentioned above the essential difference exists in the structure of the output filter. The LLC-resonant inverter consists a series-resonant circuit consisting of capacitor  $C_s$  and inductor  $L_s$  and a parallel resonant circuit consisting of inductor  $L_p$  and equivalent piezoelectric capacitor  $C_p$  [KSF02] [SFG00] [KSF02]. Note that besides the higher part count, the circuit can make use of the parasitics of the transformer: Part of  $L_s$  is contributed by the leakage inductance of the transformer, while  $L_p$  can be donated by a wider air-gap of the transformer.

Then the impedance of the LLC-resonant circuit is

$$Z_{LLCC}(j\omega) = j\omega L_s + \frac{1}{j\omega C_s} + \frac{1}{\frac{1}{j\omega L_p} + j\omega C_p + \frac{1}{Z_M(j\omega)}}, \quad (3.10)$$

where  $Z_M(j\omega)$  is the equivalent impedance of the piezoelectric motor, which represents a mechanical resonant part (for the calculation ref. section 2.8).

In publication [Sch04a] the piezoelectric motor is represented by its equivalent resistive load at resonant state  $Z_M(j\omega) = R_p'$ . Therefore the transfer function of

### 3. POWER SUPPLY TOPOLOGIES FOR HIGH-POWER PIEZOELECTRIC ACTUATORS

---

the LLCC filter is derived as:

$$\begin{aligned}
 G_{LLCC}(s) &= \frac{u_{C_p}(s)}{u_{iv}(s)} \\
 &= \frac{1}{\frac{1}{sL_p} + sC_p + \frac{1}{Z_M(s)}} \\
 &= \frac{1}{sL_s + \frac{1}{sC_s} + \frac{1}{\frac{1}{sL_p} + sC_p + \frac{1}{Z_M(s)}}}
 \end{aligned} \tag{3.11}$$

In order to attain a robust behavior of the piezoelectric actuator under resonant operation, in [Sch04a] and [LDH99] the LLCC filter circuits were designed to satisfy the following condition:

$$|G_{LLCC}(j\omega)| \Big|_{\omega=\omega_{mr1}} = 1 \text{ and } \angle G_{LLCC}(j\omega) \Big|_{\omega=\omega_{mr1}} = 0 \tag{3.12}$$

The mean operating frequency of the LLCC-resonant inverter should equal the mechanical resonance frequency  $\omega_{mr1} = 1/\sqrt{(L_M C_M)}$ , which is given by the actuator characteristics.

Solving Eq. 3.12, the results confirm the relationship of serial and parallel resonance frequency:

$$\omega_{OP} = \frac{1}{\sqrt{C_s L_s}} = \frac{1}{\sqrt{C_p L_p}} = \omega_{mr1} \tag{3.13}$$

Parallel inductor  $L_p$  compensates the reactive power generated by  $C_p$ , hence

$$L_p = \frac{1}{C_p \omega_{mr1}^2} \tag{3.14}$$

A design parameter  $\alpha_{LLCC}$  was applied to determine the relationship of the filter components:

$$\alpha_{LLCC} = \frac{C_s}{C_p} = \frac{L_p}{L_s} \tag{3.15}$$

In case of LLCC-resonant inverter, in order to compromise the nonsensitive behavior of parameter variation and the permissible content of harmonics,  $\alpha_{LLCC}$

### 3.1 State-of-the-Art of Power Supplies for Piezoelectric Actuators

is chosen as 1 [Sch04a], therefore the series resonance inductor and capacitor are calculated by:

$$L_s = L_p, C_s = C_p \quad (3.16)$$

$$|G_{LLCC}(j\omega)| = 1 \quad (3.17)$$

The operating frequency of the PIBRAC motor is 33 kHz, when  $L_M = 456 \mu\text{H}$  and  $C_M = 51 \text{ nF}$ . For driving the tangential-mode piezoelectric actuator of the PIBRAC motor, the calculated components of the LLCC filter are given in Tab. 3.2.

Parameter		Value
Mechanical resonance frequency	$f_{mr1}$	33000 Hz
Piezoelectric equiv. capacitor	$C_p$	176 nF
Series capacitor	$C_s$	176 nF
Parallel inductor	$L_p$	132 $\mu\text{H}$
Series inductor	$L_s$	132 $\mu\text{H}$

Table 3.2: Components for the design of LLCC-resonant inverter

Frequency responses of the LLCC-resonant circuit are depicted in Fig. 3.11, with capacitance  $C_p$  varied in a range of  $\pm 30\%$  and  $R'_p$  varied in a range of  $\pm 50\%$ . The operating frequency range of the piezoelectric motor is located near to the geometric mean frequency of the LLCC circuit. From Bode plots in Fig. 3.11 we observe that the gain of voltage amplitudes is close to 0 dB, and phase  $\angle G_{LLCC}$  is near  $0^\circ$  within the operating range of the motor.

The advantages of LLCC-resonant filters are obvious: First, the required robustness of the transfer characteristic against parameter variation is clearly seen. From Fig. 3.11 we see that  $G_{LLCC}(s)$  does not vary in the operating point when  $C_p$  and  $R'_p$  are changed.

Power analyses of LLCC-resonant inverter were carried out, and the results are presented in Fig. 3.12, where the relative set value of the inverter output voltage is varied from 0 to 1.0. Due to the inverter output voltage being a rectangular waveform, the nonactive power is larger than with only the fundamental component.

### 3. POWER SUPPLY TOPOLOGIES FOR HIGH-POWER PIEZOELECTRIC ACTUATORS

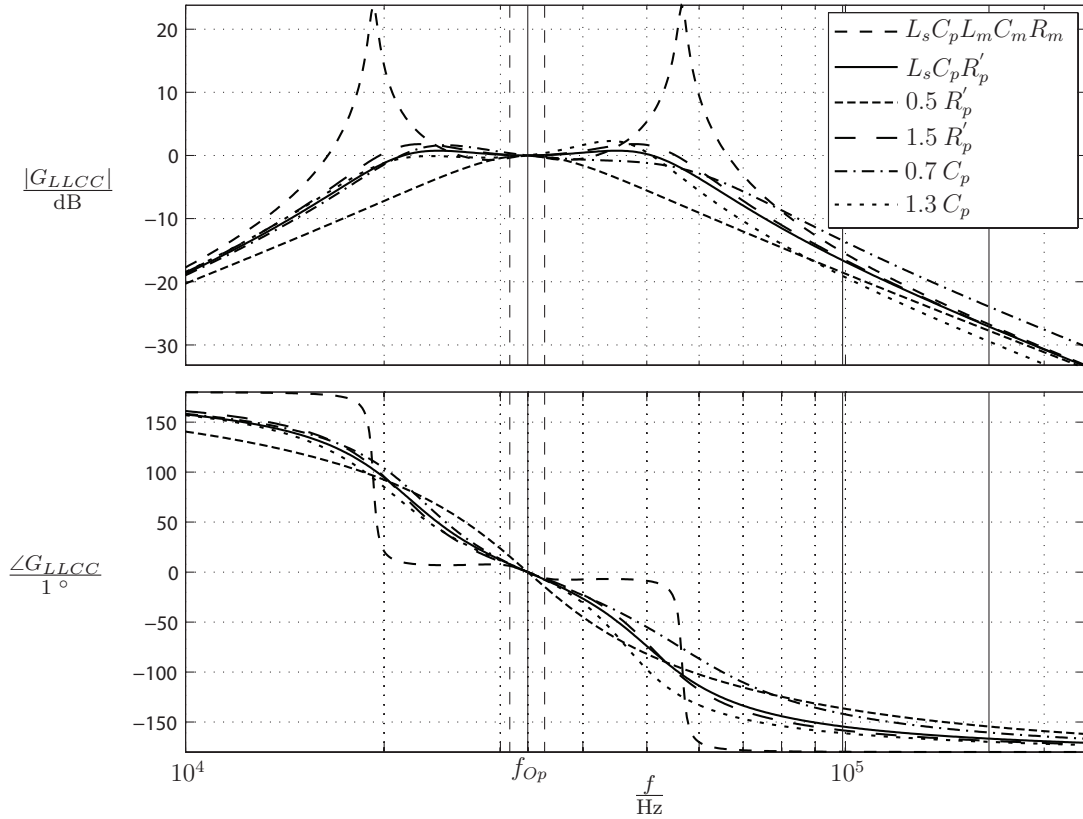


Figure 3.11: Frequency response of LLCC-resonant inverter

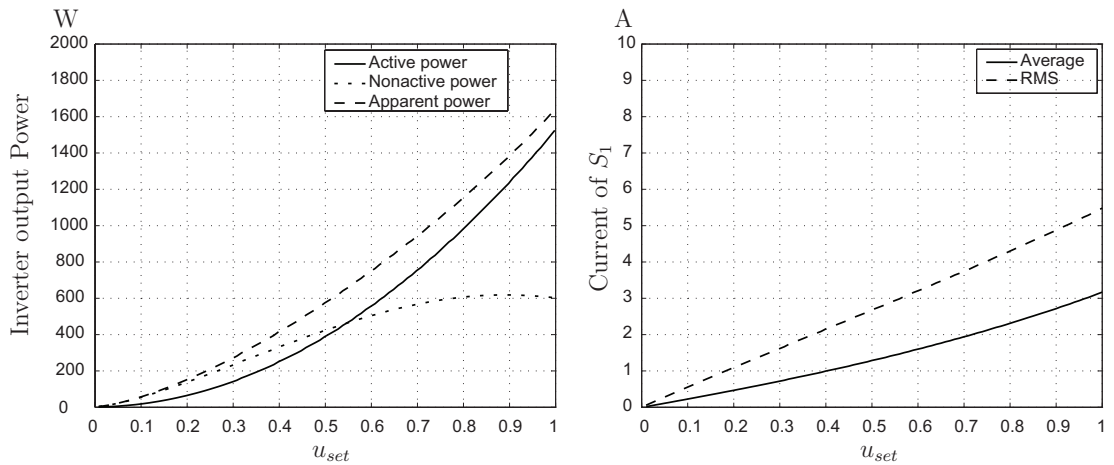


Figure 3.12: Powers of LLCC-resonant inverter vs. normalized inverter voltage and switch-current average and RMS values

Another advantage is clear from Tab. 3.3 and Fig. 3.13 that the phase shift

### 3.1 State-of-the-Art of Power Supplies for Piezoelectric Actuators

Parameter		Value
Active power	$P$	1545 W
Apparent power	$S$	1750 VA
Power factor	$PF$	0.88
RMS current of $L_s$	$I_{L_s}$	8.54 A
Current of switch $S_1$	$I_{S1,Average}$	3.2 A
	$I_{S1,RMS}$	5.8 A

Table 3.3: Operating parameters of LLCC-resonant inverter

between inverter output voltage  $u_{iv}(t)$  and current  $i_{iv}(t)$  is zero (phase  $\angle Y_{LLCC}$  is zero, see Fig. 3.13) at the operating point. Hence the power factor of the LLCC-resonant inverter is much higher than that of the LC-resonant inverter.

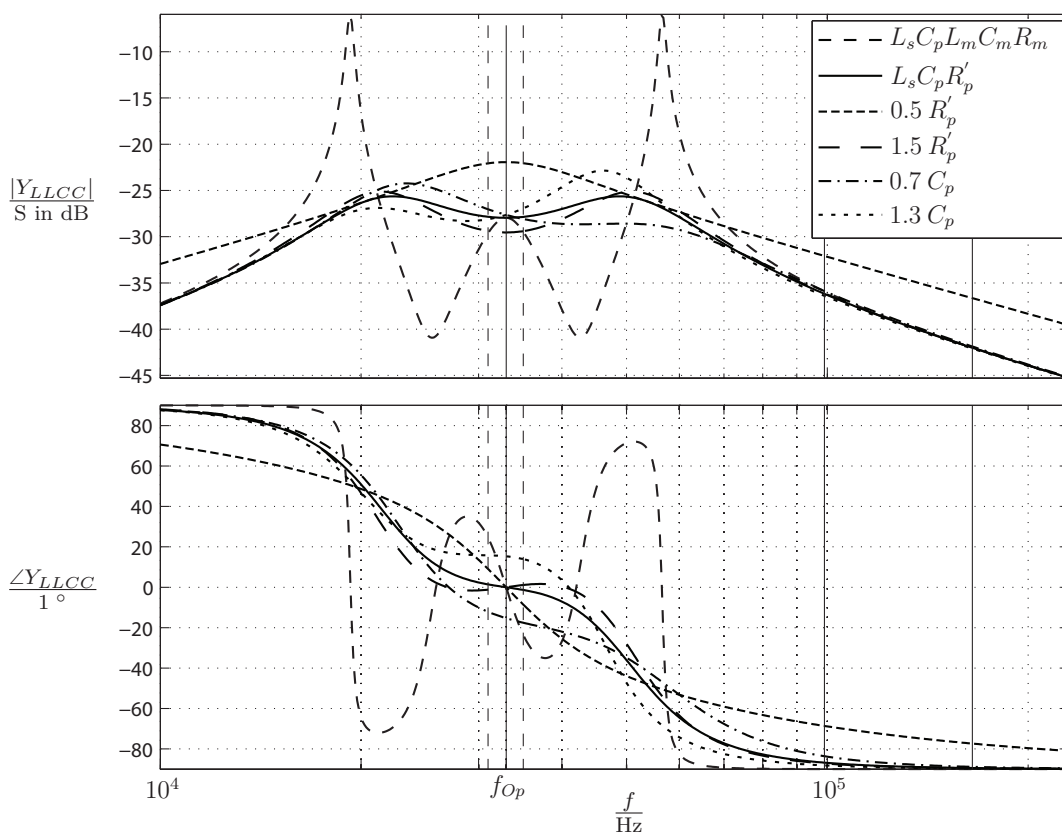


Figure 3.13: Admittance diagram of resonant controlled LLCC-type filter

Moreover the former benefits from the potential of local reactive-power compen-

### 3. POWER SUPPLY TOPOLOGIES FOR HIGH-POWER PIEZOELECTRIC ACTUATORS

---

sation by  $L_p$ : The series-resonant circuit composed by  $L_s$  and  $C_s$ , transformer and inverter provides mainly active power. Consequently, the current stress of inverter, series inductor and transformer is reduced considerably compared with the LC-type filter. Lower losses and hence smaller cooling means of the inverter are also attained.

#### 3.1.3 PWM-Controlled Inverter with LC Filter

##### 3.1.3.1 Inverter Topology and Pulse Width Modulation

A PWM-controlled inverter with LC filter (LC-PWM inverter) is shown in Fig. 3.14. This topology and its operating principle is described in various articles [EM00] [Hol03]. The topology is seemingly similar to the LC-resonant inverter, but it is driven by a different modulation scheme and a different filter characteristic results consequently.

In contrast to the resonant inverter, the LC-PWM inverter is operated with the switching frequency much higher than the mechanical resonance frequency of the piezoelectric motor or actuator. This means, during one period of the fundamental voltage the switching components are turned on and off several times (normally  $\geq 5$ ), which yields a PWM-controlled voltage for supplying the motor via the LC-type filter circuit.

The carrier-based PWM with pulse number  $n_p = 10$  per period is presented in Fig. 3.15. The principle of this method is that the switching signals are modulated by comparing a sinus signal and two triangular carrier signals with a frequency of five times higher. The frequency of the sinusoidal signal is decided by the operating frequency of the piezoelectric actuator. And the triangular carrier signals depends on the allowable switching frequency of the inverter limited by switching losses, EMC issue and the tolerable total harmonic distortion (THD). Hence, a compromise between switching frequency and switching losses has to be made during the inverter design.

### 3.1 State-of-the-Art of Power Supplies for Piezoelectric Actuators

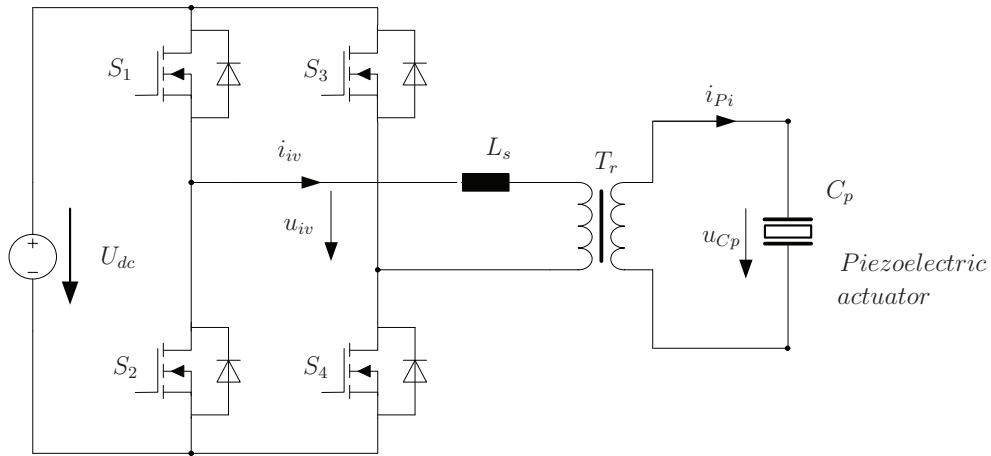


Figure 3.14: LC-PWM inverter

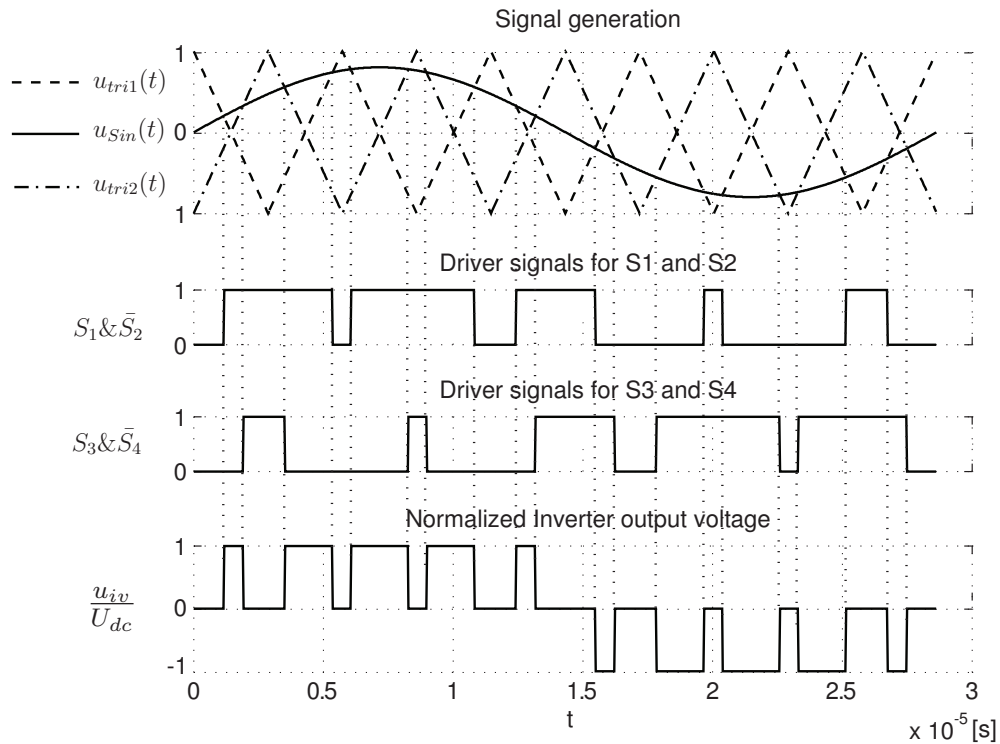


Figure 3.15: Carrier-based PWM modulation output voltage and its fundamental components

With the PWM shown in Fig. 3.15 the inverter is operated at raised switching frequency, approximately five times of mechanical resonance frequency, as com-

### 3. POWER SUPPLY TOPOLOGIES FOR HIGH-POWER PIEZOELECTRIC ACTUATORS

---

pared with the inverter using square-wave modulation (in Fig. 3.4). Hence, the switching losses of the power semiconductor components of PWM-controlled inverter are larger than the switching losses of the resonant inverter at equal power level. From the spectrum diagram shown in Fig. 3.17 we see that the harmonic components are moved to higher frequency, and the 3<sup>rd</sup> and 5<sup>th</sup> harmonics are reduced largely.

#### 3.1.3.2 LC-PWM Inverter

The main drawbacks of resonant inverters treated in section 3.1.2 are the large volume and the heavy weight of the resonant-filter magnetic components such as transformer and inductor [NF01]. In [KF04] [Sch04a] the LC-PWM inverter was investigated in order to reduce the size and weight of the inductive filter component. These investigations are focused on driving schemes for piezoelectric transducers again with low electromechanical quality factor and a output-filter characteristic weakly influenced (robust) by the varying capacitance of the piezoelectric stacks.

The LC low pass filter is indicated in Fig. 3.16, which consists of a series inductor  $L_s$ , piezoelectric capacitor  $C_p$  and equivalent load . The transfer function is described by:

$$G_{LC}(s) = \frac{u_{C_p}(s)}{u_{i_v}(s)} = \frac{1/C_p L_s}{s^2 + s/R'_p C_p + 1/C_p L_s} \quad (3.18)$$

The electrical resonance frequency is  $\omega_{elr} = 1/\sqrt{C_p L_s}$  .

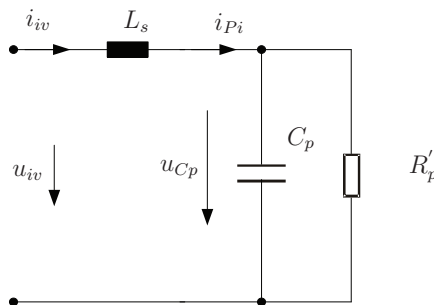


Figure 3.16: LC low pass filter

### 3.1 State-of-the-Art of Power Supplies for Piezoelectric Actuators

When the harmonic components justify the inequality  $\omega_H \gg \omega_{elr}$ , the expression for the amplitude of  $|G_{LC}(j\omega)|$  is simplified by:

$$20 \log |G_{LC}(j\omega)| \approx -40 \log\left(\frac{\omega}{\omega_{res,el}}\right) \quad (3.19)$$

This means, it is reduced with a slope of  $-40$  dB/decade, thus if the expected harmonic components  $\omega_H$  should be damped by  $\alpha_H$  dB, then  $\omega_{elr} = \omega_H \cdot 10^{\alpha_H/40}$ , and  $L_s > 1/\omega_{elr}^2 C_p$ .

The task of designing the inductor  $L_s$  can aim at damping the first appearing harmonic components. For example, using this approximation and setting the 5<sup>th</sup> harmonic to be damped by  $-20$  dB, then  $\alpha_{H5} = -20$ , then  $\omega_{elr} = \omega_{H5} 10^{-20/40}$ ,  $L_s \geq 53 \mu\text{H}$ .

Another criterion to be considered when designing  $L_s$  is the ripple of current  $i_{L_s}$ . In order to keep  $\Delta i_{L_s, max} \leq i_{L_s, Peak}/2$ , under full load operating condition,  $\Delta i_{L_s, max} = 8$  A, the inductor  $L_s$  is approximated as  $L_s \geq \frac{U_{dc} T_s / 2}{\Delta i_{max}} \approx 48 \mu\text{H}$ , where  $U_{dc}$  is the DC-link voltage and  $T_s$  is the switching period.

The components of the LC filter are given in Tab. 3.4. Comparing it to Tab. 3.1, the series inductance is reduced to a value of one fourth at unchanged ratings of  $f_{mr1}$  and  $C_p$  by driving the inverter by means of PWM instead of square-wave modulation. This cuts of course weight and volume for inductor  $L_s$  accordingly.

The advantages of LC-PWM inverter are therefore evident in contrast with resonant inverters. The essential drawback of resonant inverters is their relatively large and heavy filter component  $L_s$ , which limits its application in the case that volume and weight of the power supply are restricted, as for example the equipment in aircraft or handheld devices.

Parameter		Value
Mechanical resonance frequency	$f_{mr1}$	33000 Hz
Piezoelectric equiv. capacitor	$C_p$	176 nF
Electrical resonance frequency	$f_{elr}$	52.18 kHz
Series inductor	$L_s$	53 $\mu\text{H}$

Table 3.4: Component design of non resonant inverter with LC filter

The respective frequency response of filter input and output voltage is shown in Fig. 3.18, with capacitance  $C_p$  and  $R'_p$  varied in a range of 30 % and 50 %

### 3. POWER SUPPLY TOPOLOGIES FOR HIGH-POWER PIEZOELECTRIC ACTUATORS

---

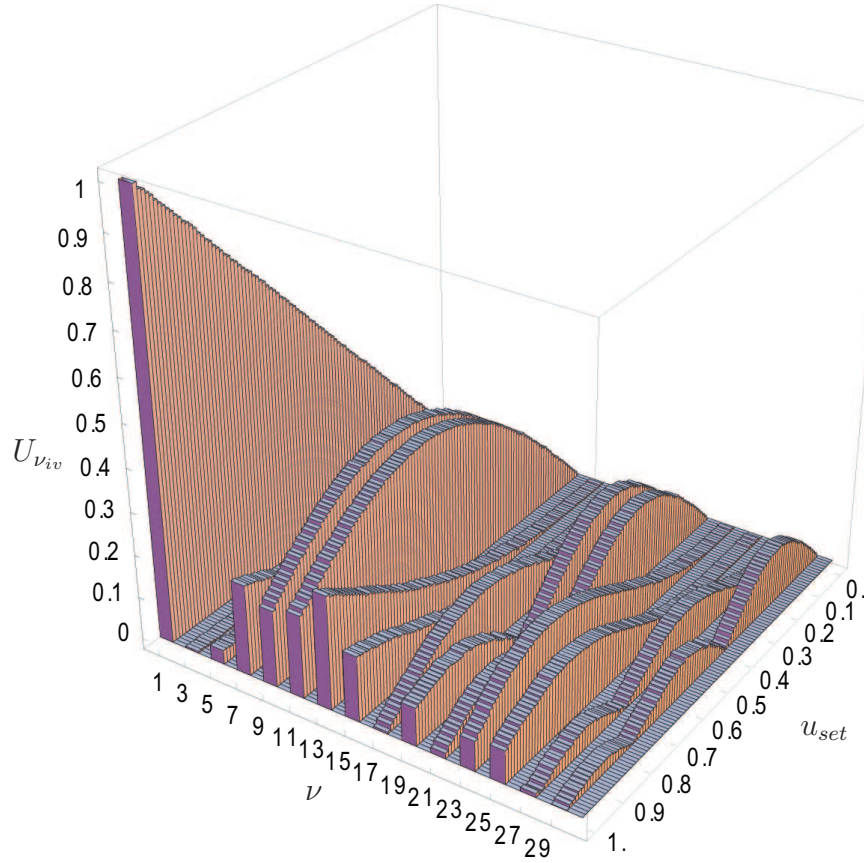


Figure 3.17: Frequency spectrum of inverter output voltage using carrier-based PWM

respectively. Fig. 3.18  $f_{Op} = 5 f_{mr1}$ . It is clearly visible that the 5<sup>th</sup> harmonic occurs now at a frequency of 175 kHz and it is damped nearly with ratio  $-20$  dB.

It can be observed that in Fig. 3.18,  $G_{LC}$  has a phase angle of  $-30^\circ$  to  $-60^\circ$  with the variation of  $C_p$  and  $R'_p$  at mechanical resonance frequency. Then due to the reactive power requirement of the piezoelectric motor, the shortcoming is also obvious and is highlighted in Tab. 3.5. The power factor of the LC-PWM inverter is of course higher than for the LC-resonant inverter, but lower than for the LLC-resonant inverter, due to the missing reactive-power compensation.

The results of power analysis of LC-PWM inverter are studied and presented in Fig. 3.19, where the set value of inverter output voltage is varied from 0 to 0.76. Because  $|G_{LC}(j\omega_{mr1})|$  is larger than 0 dB, so when the voltage  $u_{Cp}(t)$  arrives at 270 V, the set value  $u_{set}$  is still less than 1.0.

### 3.1 State-of-the-Art of Power Supplies for Piezoelectric Actuators

To compare with results of LLCC-resonant inverter in Fig. 3.12, the nonactive power - now mainly reactive power - and the apparent power of the LC-PWM inverter are larger than that of the LLCC-resonant inverter. Therefore the average and the RMS current values of the power MOSFET  $S_1$  are larger than that in Fig. 3.12.

Parameter		Value
Active power	$P$	1532 W
Apparent power	$S$	2028 VA
Power factor	$PF$	0.756
RMS current of $L_s$	$I_{L_s}$	10.7 A
Current of switch $S_1$	$I_{S1,Average}$	3.8 A
	$I_{S1,RMS}$	6.9 A

Table 3.5: Operating parameters of LC-PWM inverter

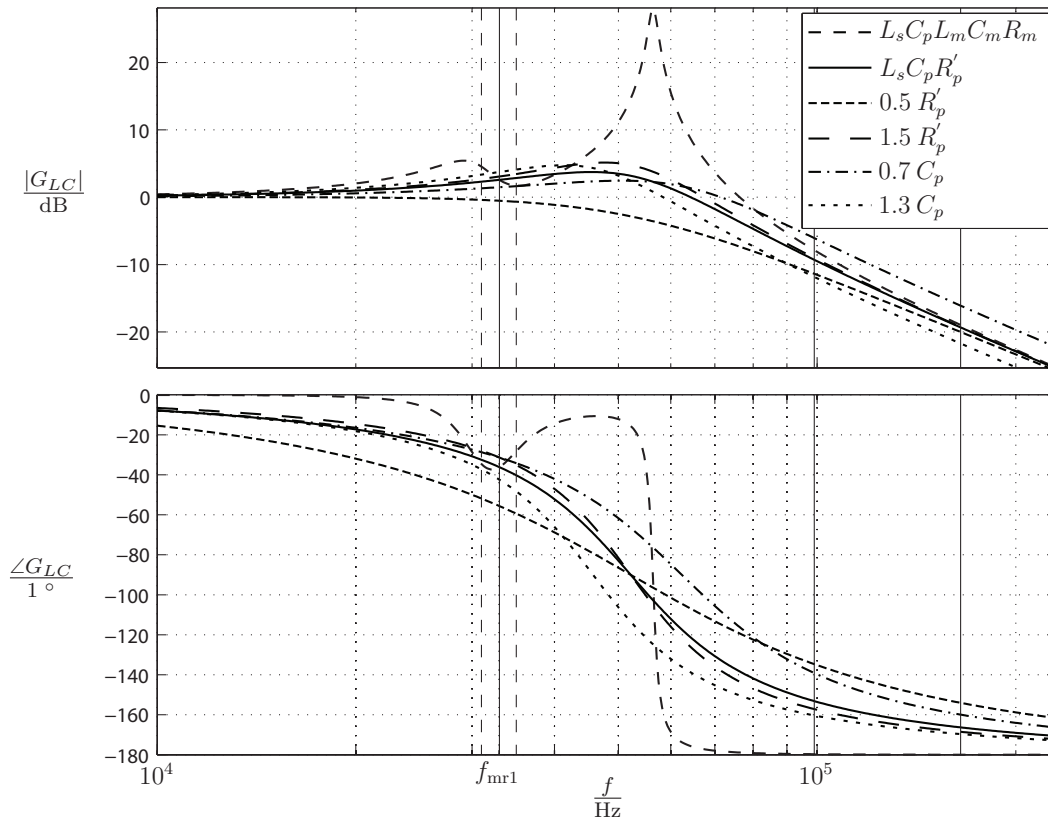


Figure 3.18: Frequency response of PWM-controlled LC filter

### 3. POWER SUPPLY TOPOLOGIES FOR HIGH-POWER PIEZOELECTRIC ACTUATORS

---

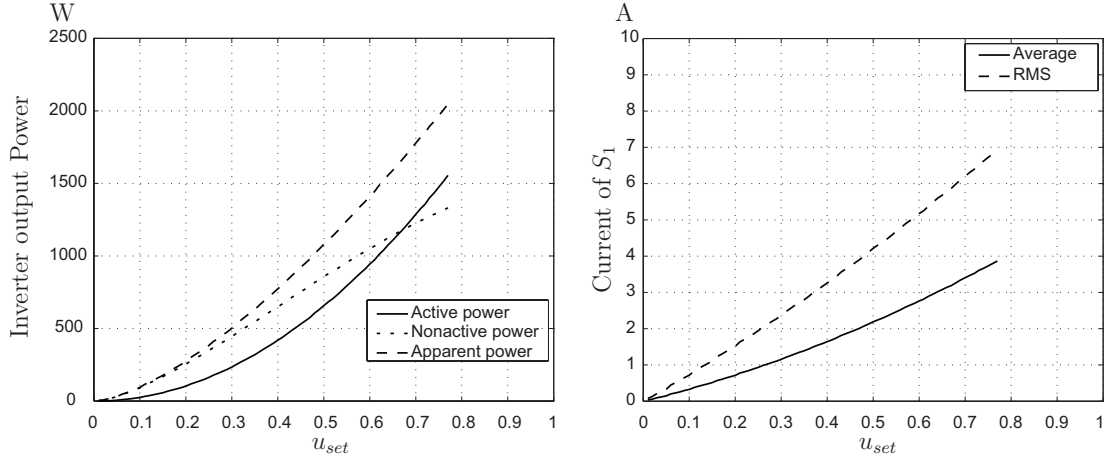


Figure 3.19: Power and switch-current of LC-PWM inverter

Thus, the nonactive power is provided via the full power "path", comprising full-bridge inverter and transformer. Consequently, volume and weight of the transformer are increased, more apparent power stresses the inverter side, producing not only additional conduction losses within the inverter, but also increased switching losses at the correspondingly higher switching frequency, compared to resonant-mode operation.

From these, it can be concluded that LC-PWM inverters are more suitable for weakly-damped piezoelectric vibration systems such as bond sonotrodes, where no or small reactive power is delivered at the operating point by the inverter. This conclusion was also proved in few publications [KF04].

## 3.2 Advanced Power Supply Concepts

From the operating principle of the MM-USM explained in Chapter 2, it is known that the MM-USM is to be supplied by a system with two-phase output for the tangential-mode and the normal-mode piezoelectric actuators. The amplitudes of both driving AC-voltages are required as 270 V peak at a frequency of 33 kHz. The input DC-link voltage of 270 V is supplied from the aircraft power grid. The total required power by one motor is up to 1.5 kW.

Under power supply aspects the aforementioned circuit should thus provide a robust and highly dynamic operating behavior in order to stabilize the proper

## 3.2 Advanced Power Supply Concepts

---

operation within a certain frequency and capacitance range. Thus, design of control and filter should take into account the above mentioned requirements.

Considering the analysis in Chapter 3.1, the state-of-the-art of power supplies developed to drive the piezoelectric actuators needs to be improved, in order to satisfy the application requirements of the MM-USM optimally.

A resonant inverter with LLC-type output filter shows advanced characteristics and best-suited properties with respect to efficiency, stationary and dynamic behavior, as well as control and commissioning effort. The drawback of these resonant inverters is the large volume, heavy weight and high cost of the magnetic components of the resonant filter such as transformer and inductor, especially in case of driving high-power piezoelectric actuators.

Therefore, power converters which do not require heavy inductors are of great interest. The carrier-based PWM-controlled inverter with LC filter investigated in [Sch04a] [KF04] provides the possibility to reduce the size and the weight of magnetic components. However, it was shown that LC-PWM inverters are only suitable for weakly damped piezoelectric vibration systems such as bond sonotrodes, because the resonant filter and transformer have to provide large reactive power. Moreover the high switching frequency of PWM inverter results in consequently more switching losses and eventually conflicts with EMC issues.

The other mentioned criterion gains also importance, if we imagine that the MM-USM is located in a larger distance from the inverter, connected by cables. Then these cables as part of the power path would be stressed by the larger current, too, generating a large impact on weight.



## Chapter 4

# PWM-Controlled Driving Concept with LLCC-Filter Circuit

In this chapter, an advanced driving concept is studied to supply the multi-mass ultrasonic motor (MM-USM) for the piezoelectric brake actuator. In contrast to the LLCC-resonant inverter, the LLCC-type filter is controlled by pulse width modulation (PWM) instead of square-wave modulation in the proposed driving concept. Therefore it is named as LLCC PWM inverter. Combining the LLCC-type filter with a PWM-controlled inverter makes best use of the advantages of both.

Considering the high operating frequency of ultrasonic motor, it is unavoidable to use a proper technique to limit the switching losses and address EMC issues. Hence, a PWM inverter using harmonic eliminating technique and a three-level carrier-based PWM (CBM) inverter are investigated and employed in this application.

In order to characterize the different modulation schemes controlling inverter and filter topologies, a comparison in respect to weight and volume of magnetic components, power factor and losses of power supplies, the total harmonic distortion (THD) of the motor voltage and the dynamic behavior of the power supply are carried out.

## 4. PWM-CONTROLLED DRIVING CONCEPT WITH LLCC-FILTER CIRCUIT

### 4.1 LLCC-Filter Circuit Design Fed by PWM Inverter

#### 4.1.1 Design Consideration

The proposed LLCC PWM inverter is shown in Fig. 4.1. Main objectives for the power supply to be applicable for driving an aircraft brake are: Reduction of weight and volume, increase of efficiency, dynamic response and robustness.

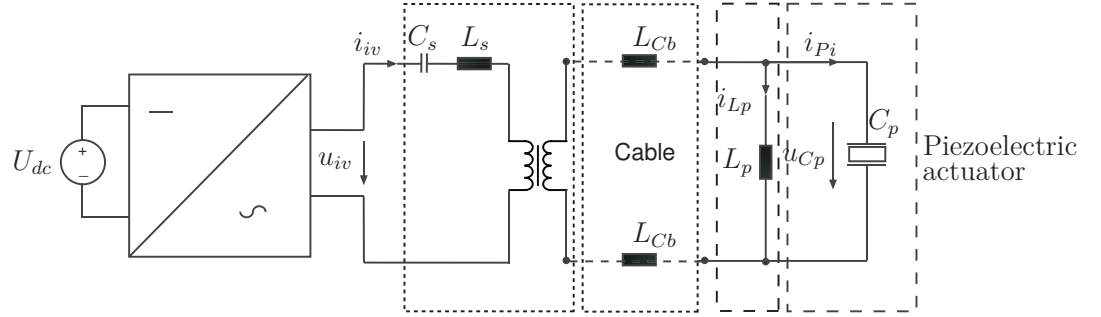


Figure 4.1: PWM-controlled LLCC filter topology

Fig. 4.1 displays the LLCC filter, subdivided into three sections: the left section shows the discrete components forming the series part of the resonant tank and the transformer; the central section consists of the series equivalent inductance of the cable connection between the inverter and the actuator; and in the right section there is the parallel part of the resonant tank.

The LLCC-filter circuit is characterized by two electrical resonance frequencies as calculated in Eq. 4.1 and Eq. 4.2. They represent the effects of the sum of the series-resonant tank and of the parallel-resonant tank. The first resonance frequency  $\omega_{er1}$  is calculated by the sum of  $L_p$  and  $L_s$  and  $C_s$ , while the second resonance frequency  $\omega_{er2}$  is given by the capacitance of  $C_p$  and  $C_s$  and the series inductor  $L_s$ .

$$\omega_{er1} \approx \frac{1}{\sqrt{(L_s + L_p)C_s}} \quad (4.1)$$

$$\omega_{er2} \approx \frac{1}{\sqrt{\frac{C_s C_p}{C_s + C_p} L_s}} \quad (4.2)$$

## 4.1 LLCC-Filter Circuit Design Fed by PWM Inverter

Considering the requirement described in Eq. 3.12 and its solution in Eq. 3.13 for attaining robustness of the LLCC filter, these resonance frequencies can be simplified using the design parameter  $\alpha_{LLCC} = C_s/C_p = L_p/L_s$ , which is given in Eq. 3.15, as follows:

$$\omega_{er1} \approx \frac{\omega_{mr1}}{\sqrt{1 + \alpha_{LLCC}}} \quad (4.3)$$

$$\omega_{er2} \approx \omega_{mr1} \sqrt{1 + \alpha_{LLCC}} \quad (4.4)$$

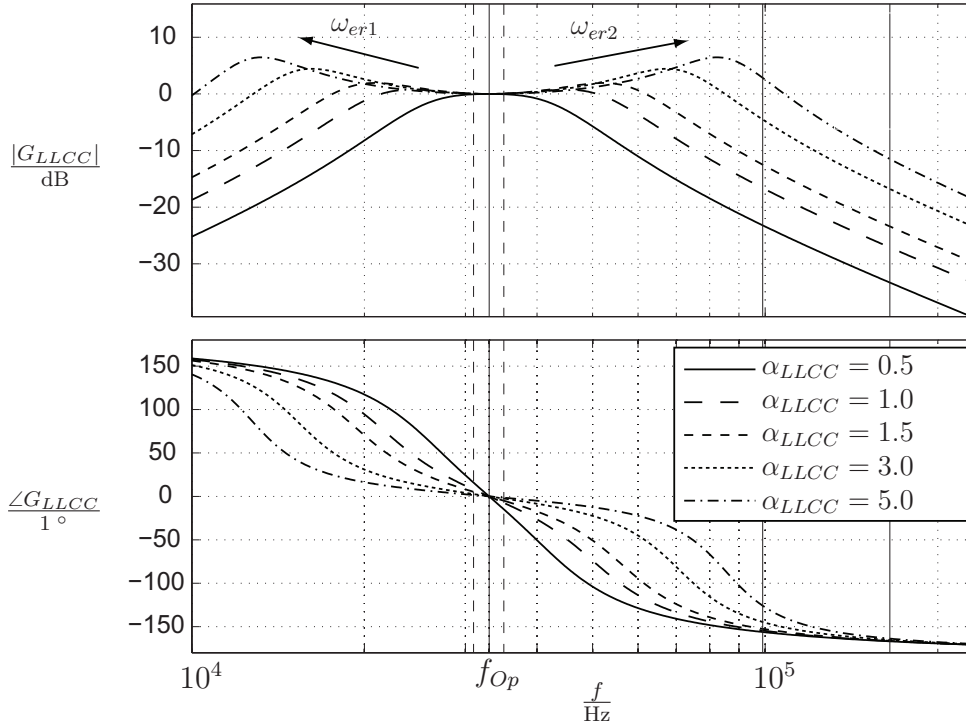


Figure 4.2: Frequency response of LLCC filter with varied  $\alpha_{LLCC} = [0.5, 1.0, 1.5, 3.0, 5.0]$

Hence the series-resonant inductance is calculated by

$$L_s = \frac{L_p}{L_p C_p \omega_{er2}^2 - 1} = \frac{L_p}{\alpha_{LLCC}} \quad (4.5)$$

$$C_s = \frac{C_p L_p}{L_s} = \alpha_{LLCC} C_p$$

## 4. PWM-CONTROLLED DRIVING CONCEPT WITH LLCC-FILTER CIRCUIT

---

Then using Eq. 4.5 the transfer function of the LLCC filter  $G_{LLCC}(s)$  in Eq. 3.11 can be simplified and represented using  $\alpha_{LLCC}$  as:

$$\begin{aligned} G_{LLCC}(s) &= \frac{u_{C_p}(s)}{u_{iv}(s)} \\ &= \frac{\alpha_{LLCC} C_p L_p R'_p s^2}{R'_p + L_p s + (2 + \alpha_{LLCC}) C_p L_p R'_p s^2 + C_p L_p^2 s^3 + C_p^2 L_p^2 R'_p s^4} \quad (4.6) \end{aligned}$$

The frequency response of the LLCC filter with parameter  $\alpha_{LLCC} = [0.5, 1.0, 1.5, 3.0, 5.0]$  is shown in Fig. 4.2. Increasing  $\alpha_{LLCC}$ , the first resonance frequency  $\omega_{er1}$  is decreased and the second  $\omega_{er2}$  is increased, without changing the operating frequency of the piezoelectric actuator  $f_{Op}$ .

If a larger  $\alpha_{LLCC}$  is used, the required  $L_s$  becomes smaller, and at the same time a larger  $C_s$  has to be employed according to Eq. 3.12. When  $\alpha_{LLCC}$  increases, the gain of transfer function  $G_{LLCC}$  is also increased at the frequency  $\omega \geq \omega_{er2}$ , then the suppression of harmonic components of inverter output voltage will be decreased. Specially stronger influence takes place at the 3<sup>rd</sup>, 5<sup>th</sup>, 7<sup>th</sup> and 9<sup>th</sup> harmonic components, which dominate the harmonics of inverter voltage with square-wave modulation.

So if the 3<sup>rd</sup>, 5<sup>th</sup>, 7<sup>th</sup> and 9<sup>th</sup> harmonic components of the inverter output voltage are to be reduced by the method of PWM, a larger  $\alpha_{LLCC}$  can be applied, and the second electrical resonant point of the filter can be set at higher frequency than for the resonant converters, in order to reduce the weight and volume of the magnetic filter components.

### 4.1.2 Design of Filter Parameters

The procedure for designing the LLCC filter is described as follows.

As we know the damping of harmonic components is represented by the gain of the filter transfer function. For a  $n^{\text{th}}$  harmonic component of the filter voltage, the transfer function is calculated from Eq. 4.6 as:

$$G(n, \alpha_{LLCC}) = \frac{j^2 \alpha_{LLCC} n^2}{j^4 n^4 + \frac{j^3 n^3}{2\pi C_p R'_p f_{mr1}} + j^2 (2 + \alpha_{LLCC}) n^2 + \frac{jn}{2\pi C_p R'_p f_{mr1}} + 1} \quad (4.7)$$

## 4.1 LLCC-Filter Circuit Design Fed by PWM Inverter

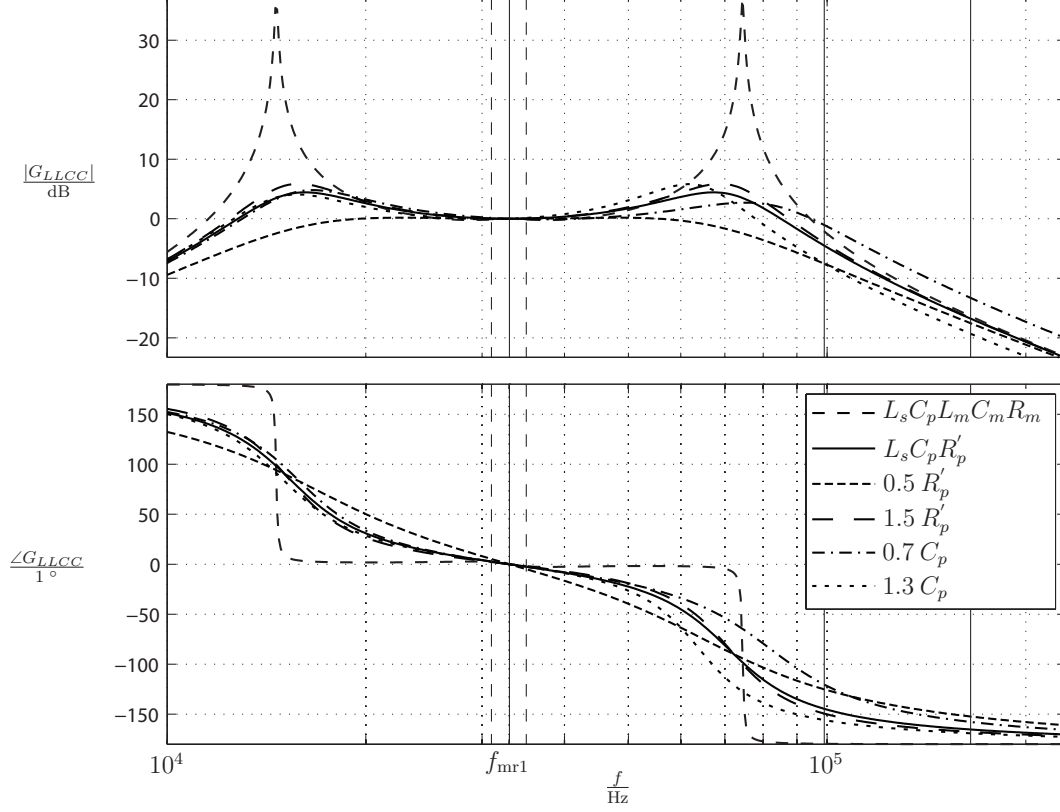


Figure 4.3: Frequency response of PWM-controlled LLCC filter

So the first step of designing LLCC filter is to choose the value  $\alpha_{LLCC}$ , which is determined by the required damping of the dominating harmonic component. For example, if the 3<sup>rd</sup> harmonic is the dominating one and is to be attenuated by  $-5$  dB:

$$\begin{aligned} |G(n, \alpha_{LLCC})| \Big|_{n=3} &= -5 \text{ dB}, \\ \text{then } \alpha_{LLCC} &\approx 3 \end{aligned} \quad (4.8)$$

Normally the first appearing lower-harmonic component is to be reduced. Therefore the choice of  $\alpha_{LLCC}$  is determined by the inverter topology and its modulation scheme, and of course the switching frequency.

Secondly consider  $C_p$  as equivalent capacitance of the load. In order to compensate for the reactive power of the capacitive load and minimize the electric

#### 4. PWM-CONTROLLED DRIVING CONCEPT WITH LLCC-FILTER CIRCUIT

stress of cable, transformer, series-resonant filter consisting of  $C_s$  and  $L_s$  and inverter, the parallel inductor  $L_p$  is calculated by

$$L_p = \frac{1}{C_p \omega_{mr1}^2} \quad (4.9)$$

where  $\omega_{mr1}$  is the mechanical resonance frequency calculated in Eq. 2.10.

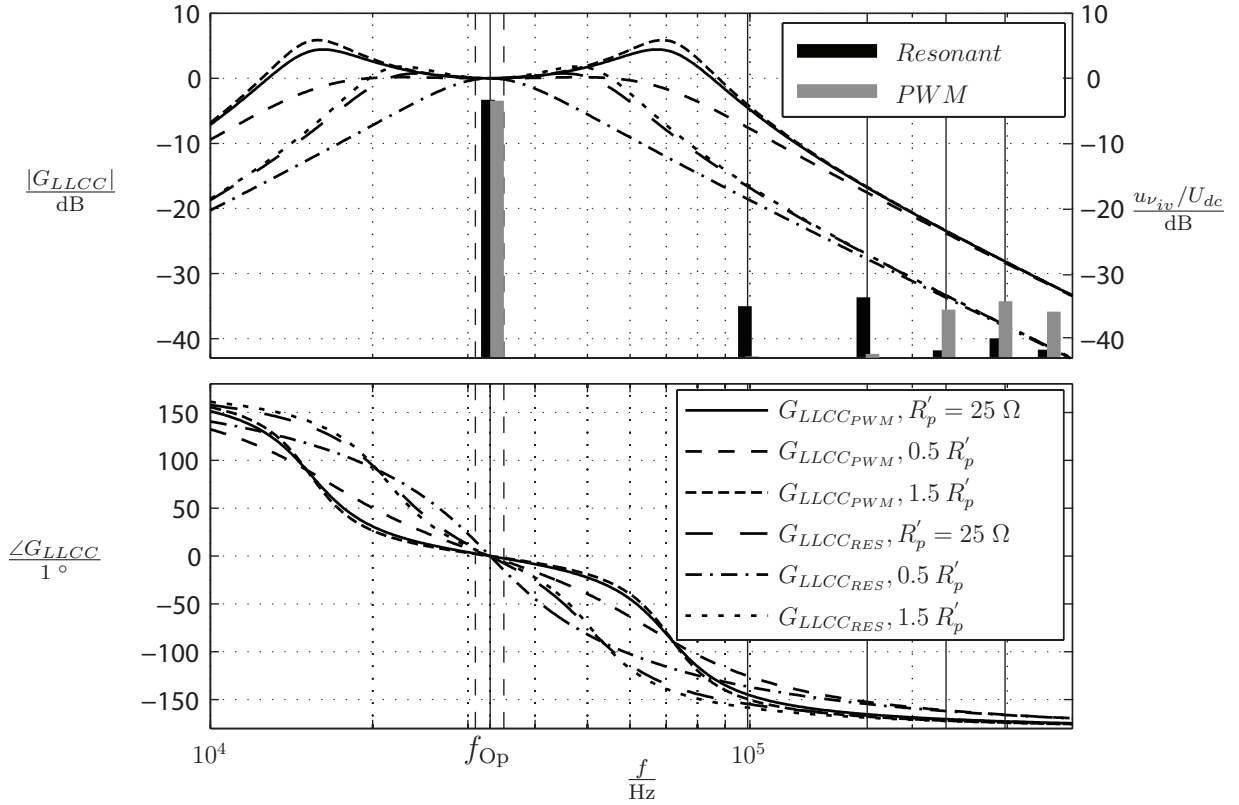


Figure 4.4: Comparison of frequency response of LLCC filter

With results of the example in Eq. 4.8, where  $\alpha_{LLCC}$  equals 3, the second electrical resonance frequency  $\omega_{er2}$  is approximated by  $2\omega_{mr1}$ . Consequently, a largely reduced rating for  $L_s$  results, which is only  $\approx 1/3$  of the LLCC-resonant inverter. This yields in a small and light series-resonant inductive components.

The frequency response of LLCC filter is shown in Fig. 4.3. By its inspection the advantages of LLCC filters, such as robustness to parameter fluctuations, e.g. the piezoelectric capacitance, and simple controllability compared with LC-filters become obvious.

---

## 4.2 Advanced Pulse Width Modulation Design

In order to compare the transfer function of the square-wave modulation controlled and the PWM-controlled LLCC filter, the frequency response of both are presented in Fig. 4.4, as well as the harmonic spectrum of the normalized inverter voltage  $u_{\nu_{iv}}/U_{dc}$  using square-wave modulation and PWM (5 pulses per half-period, see Fig. 3.15).

The second resonant frequency  $\omega_{er2}$  of the LLCCC filter is set at a higher frequency compared with the inverter with square-wave modulation, since the important 3<sup>rd</sup> and 5<sup>th</sup> harmonics are largely reduced by the PWM strategy so there is no need to suppress these frequencies by the filter. As a result, smaller and lighter filter components can be used, and the dynamic response is improved.

Moreover, the Bode diagrams of Fig. 4.4 show that the operating frequency of designed PWM-controlled LLCC-type filter can be varied within a range of 20 kHz – 50 kHz without any need to adopt the filter components, compared to narrow band 30 kHz – 40 kHz with the design of the resonant controlled inverter. This advantageous property can be utilized, if an actuator is to be characterized or driven versus a large frequency bandwidth.

## 4.2 Advanced Pulse Width Modulation Design

### 4.2.1 Introduction

Considering the analysis in Chapter 4.1, the pulse number of the inverter output voltage can be increased, if the switching frequency of the PWM-controlled inverter is increased, resulting in lighter and smaller magnetic filter components.

The reason for that can be explained through the bandpass characteristics of the LLCC filter and the relationship between RMS value of each harmonic and the switching frequency. The fundamental component and the first six harmonic components from  $\nu = 3$  to 13 are presented in Fig. 4.5. With increasing the switching frequency the first appearing harmonic components are moved towards higher frequency position, and the less harmonic components occur in the voltage of the piezoelectric actuator, because the harmonic components at higher frequency are suppressed by a higher attenuation ratio.

#### 4. PWM-CONTROLLED DRIVING CONCEPT WITH LLCC-FILTER CIRCUIT

---

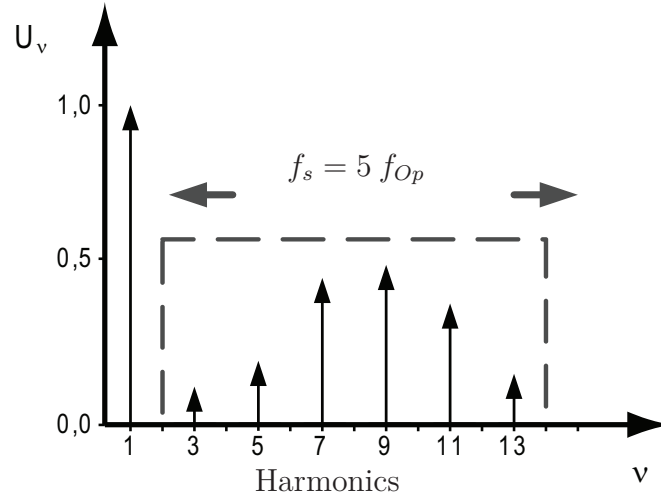


Figure 4.5: Effect between fundamental and switching frequency  $f_s$

But when applying piezoelectric actuators the mechanical resonance frequency, which equals the operating frequency of the actuator, is in a frequency range from 20 kHz to 40 kHz. This means the inverter switching frequency should be increased to a range from 140 kHz to 300 kHz, generating more switching losses and possibly EMI problems.

To overcome these shortcomings of two-level carrier-based PWM technology, two kinds of advanced technologies, which are the selected harmonic elimination modulation and multilevel modulation technology, were chosen to be employed for the inverter development. In the following chapters, both technologies are studied and employed to feed the multi mass ultrasonic motor (MM-USM) via the LLCC-type filter designed using method in Chapter 4.1.

#### 4.2.2 LLCC Two-Level Inverter Using Selected Harmonics Elimination Technique

The proposed LLCC two-level inverter shown in Fig. 4.6 is investigated to excite the high-power piezoelectric actuator, in which a LLCC-filter circuit is utilized and operated in PWM-controlled mode using harmonic elimination modulation (HEM) [LFB08]. Of course the inverter resembles the LLCC-resonant inverter, but due to the different modulation scheme, these inverters behave differently,

and show a better performance which is presented later.

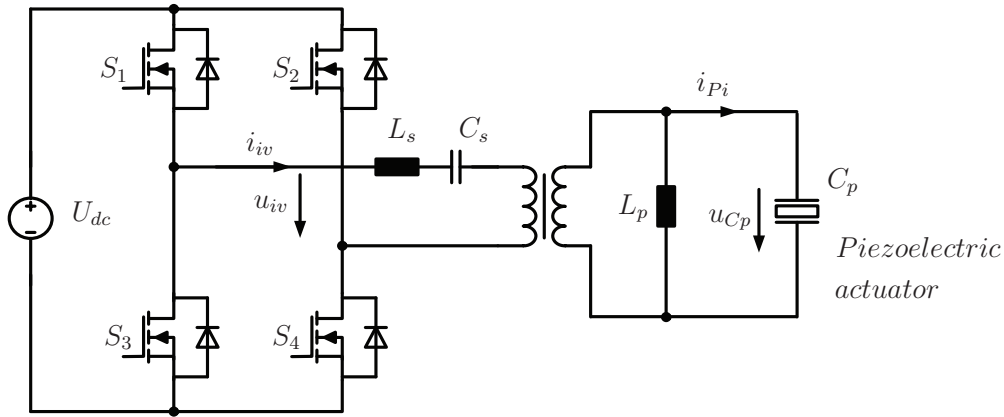


Figure 4.6: Optimal pulse modulated 2-level inverter with LLCC filter

### 4.2.2.1 PWM with Elimination of Selected Harmonics

Harmonic elimination techniques are described in [Dau72] [PH73] [PH74] [SBG94] [SBG96]. The difference between harmonic elimination modulation (HEM) and carrier-based modulation (CBM) is that, according to a preceding Fourier Series analysis the switching angles are pre-calculated in order to eliminate some appointed harmonic components instead of comparing simply a sinusoidal reference signal and triangular signals of higher frequency, as described in Chapter 3.1.3 .

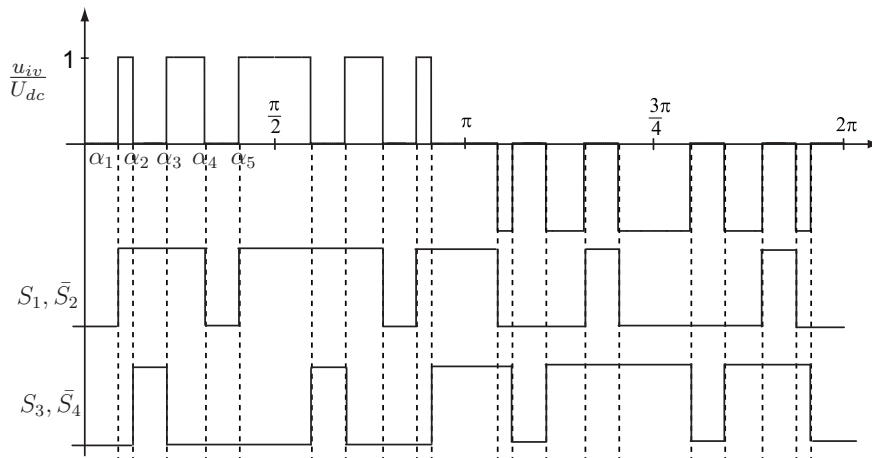


Figure 4.7: Normalized inverter output voltage and switching signals after HEM

#### 4. PWM-CONTROLLED DRIVING CONCEPT WITH LLCC-FILTER CIRCUIT

---

The modulated inverter output voltage  $u_{iv}(t)$  produced by harmonic elimination modulation (HEM) is shown in Fig. 4.7, which is normalized to input DC-link voltage  $U_{dc}$ . A pulse pattern with five switching angles, which are generated by the elimination of the harmonics of orders 3, 5, 7, and 9, is applied in a quarter period as depicted in Fig. 4.7. The group of angle in one full period can be described as:

$$\begin{cases} \alpha_i = \alpha_i \\ \alpha_{n+i} = \pi - \alpha_{n+1-i} \\ \alpha_{2n+i} = \pi + \alpha_i \\ \alpha_{3n+i} = 2\pi - \alpha_{n+1-i} \end{cases}, \quad i = 1 \dots n \quad (4.10)$$

with  $n = 5$ . A set of solutions for switching angles satisfying criterion

$$0 \leq \alpha_1 \leq \alpha_2 \leq \dots \leq \alpha_n \leq \frac{\pi}{2} \quad (4.11)$$

has to be obtained for each increment of the fundamental reference signal for voltage control with simultaneous elimination of harmonics.

By using Fourier analysis the inverter output voltage normalized to  $U_{dc}$  is calculated as follows:

$$U_{\nu_{iv}} = \begin{cases} \frac{2}{\nu\pi} \sum_{i=1}^n (-1)^{i+1} \cos(\nu\alpha_i), & \nu = \{\dots, -3, -1, 1, 3, \dots\} \\ 0 & \text{other} \end{cases} \quad (4.12)$$

From the quarter-symmetry we know that only odd harmonics exist. Fourier coefficients are given by,

$$\hat{U}_{\nu_{iv}} = \frac{4}{(2\nu - 1)\pi} \sum_{i=1}^n (-1)^{i+1} \cos((2\nu - 1)\alpha_i), \quad \forall \nu \in \mathbb{N} \quad (4.13)$$

which can be formulated in the matrix form as follows,

$$\begin{bmatrix} \hat{U}_{1_{iv}} \\ \hat{U}_{2_{iv}} \\ \vdots \\ \hat{U}_{n_{iv}} \end{bmatrix} = \begin{bmatrix} \frac{4 \cos(\alpha_1)}{\pi} - \frac{4 \cos(\alpha_2)}{\pi} + \dots (-1)^{n+1} \frac{4 \cos(\alpha_n)}{\pi} \\ \frac{4 \cos(3\alpha_1)}{3\pi} - \frac{4 \cos(3\alpha_2)}{3\pi} + \dots (-1)^{n+1} \frac{4 \cos(3\alpha_n)}{3\pi} \\ \vdots \\ \frac{4 \cos(n\alpha_1)}{n\pi} - \frac{4 \cos(n\alpha_2)}{n\pi} + \dots (-1)^{n+1} \frac{4 \cos(n\alpha_n)}{n\pi} \end{bmatrix} \quad (4.14)$$

## 4.2 Advanced Pulse Width Modulation Design

---

In order to eliminate the 3<sup>rd</sup>, 5<sup>th</sup>, 7<sup>th</sup>,  $\dots$ ,  $n^{\text{th}}$  harmonic components, non-linear equations with the required modulation amplitude  $\mathbf{M}_a$  have to be solved using suitable numerical methods [SBG96]:

$$\boldsymbol{\alpha}^{(j+1)} = \boldsymbol{\alpha}^{(j)} - (\nabla \hat{U}_{iv}(\boldsymbol{\alpha}^{(j)}))^{-1} (\hat{U}_{iv}(\boldsymbol{\alpha}^{(j)}) - \mathbf{M}_a), \quad (4.15)$$

in which  $j$  represents the iteration counter of the loop, and  $\boldsymbol{\alpha}$  is a vector containing the switching points:

$$\boldsymbol{\alpha} = \begin{pmatrix} \alpha_1 \\ \alpha_2 \\ \vdots \\ \alpha_n \end{pmatrix} \quad (4.16)$$

$\mathbf{M}_a$  is the expected modulation amplitude of the fundamental and harmonic components normalized by  $U_{dc}$ :

$$\mathbf{M}_a = \begin{pmatrix} \hat{U}_{1iv}^* \\ 0 \\ \vdots \\ 0 \end{pmatrix} \quad (4.17)$$

and  $(\nabla \hat{U}_{iv}(\boldsymbol{\alpha}))$  is the Jacobian matrix of  $(\hat{U}_{iv}(\boldsymbol{\alpha}))$ :

$$\begin{aligned} \nabla \hat{U}_{iv}(\boldsymbol{\alpha}) &= \frac{\partial \hat{U}_{iv}(\boldsymbol{\alpha})}{\partial (\alpha_1, \dots, \alpha_n)} \\ &= \begin{pmatrix} -\frac{4 \sin(\alpha_1)}{\pi} & \frac{4 \sin(\alpha_2)}{\pi} & \dots & (-1)^n \frac{4 \sin(\alpha_n)}{\pi} \\ -\frac{4 \sin(3\alpha_1)}{\pi} & \frac{4 \sin(3\alpha_2)}{\pi} & \dots & (-1)^n \frac{4 \sin(3\alpha_n)}{\pi} \\ \vdots & \vdots & \ddots & \vdots \\ -\frac{4 \sin(n\alpha_1)}{\pi} & \frac{4 \sin(n\alpha_2)}{\pi} & \dots & (-1)^n \frac{4 \sin(n\alpha_n)}{\pi} \end{pmatrix} \end{aligned} \quad (4.18)$$

The calculated switching angles for minimizing the 3<sup>rd</sup>, 5<sup>th</sup>, 7<sup>th</sup>, 9<sup>th</sup> harmonic components are presented in Fig. 4.8 versus the modulation amplitude. The modulation amplitude  $u_{set} = U_{1iv}^*$  is plotted on the horizontal axis and the switching angles for a quarter-period are on the vertical axis. The initial value begins with  $u_{set} = 0.01$ .

#### 4. PWM-CONTROLLED DRIVING CONCEPT WITH LLCC-FILTER CIRCUIT

---

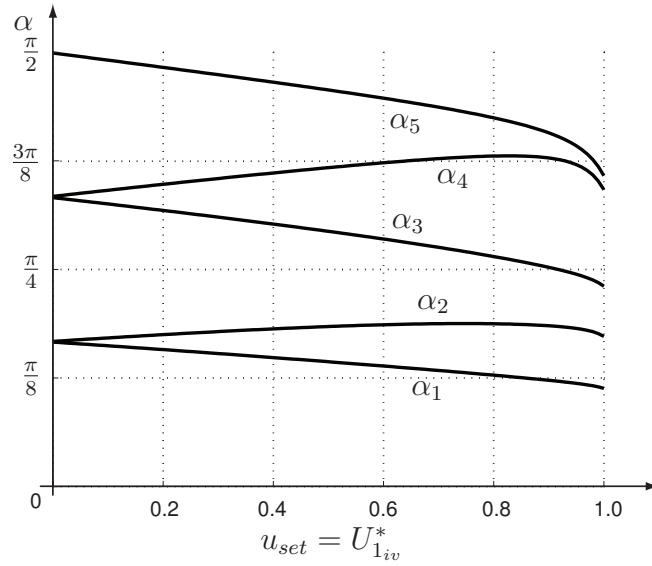


Figure 4.8: Switching angles for eliminating 3<sup>rd</sup>, 5<sup>th</sup>, 7<sup>th</sup>, 9<sup>th</sup> harmonic vs. modulation index

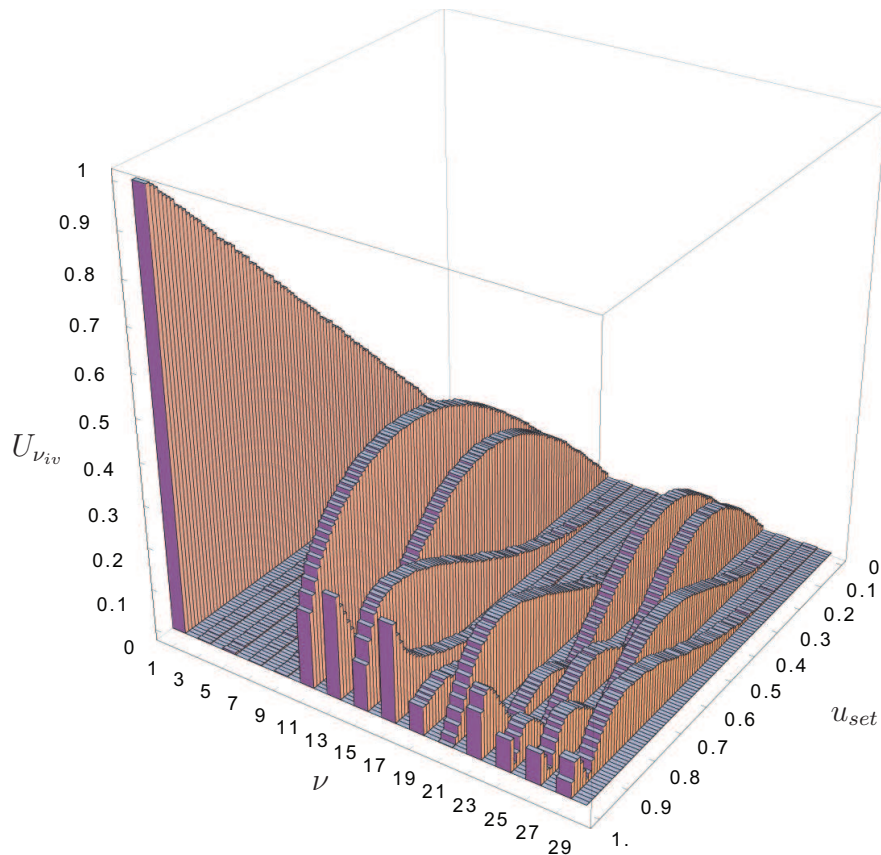


Figure 4.9: Spectrum of output voltage using two-level HEM

## 4.2 Advanced Pulse Width Modulation Design

---

The spectrum of the inverter output voltage is shown in Fig. 4.9. As expected the 3<sup>rd</sup>, 5<sup>th</sup>, 7<sup>th</sup>, 9<sup>th</sup> harmonic components do not occur, even though the switching frequency is the same as with carrier-based PWM (see Fig. 3.17). Hence the harmonic components of inverter output voltage are moved to the higher frequency range.

Therefore it is useful to apply selected harmonics elimination PWM for generating switching signals without increasing the switching frequency, so that the first dominating harmonic component is shifted towards higher frequency, where it is damped largely via the filter. The low-order harmonic content of the voltage applied to the load is eliminated or largely reduced.

### 4.2.2.2 Effects on LLCC Filter

Using HEM an output voltage with low THD is provided and a lighter and smaller series inductor  $L_s$  can be used in the LLCC-filter circuit on the one hand. On the other hand a smaller  $L_s$  will allow efficiency enhancement.

Considering that the dominating harmonic components occur at 11th and 13th order with a frequency of more than 300 kHz, a light and small inductor  $L_s$  is sufficient. The design process of filter components differs from the filter design of LC-PWM and LLCC-resonant inverters, and is described in section 4.1.

Considering the possible delay time of switching signals generated by MOS-FET drivers, low-order extra harmonics can occur in the inverter output voltage. Therefore alike the example in Eq. 4.8, the damping of 3<sup>rd</sup> harmonic is chosen at  $-5$  dB, so that a design parameter  $\alpha_{LLCC} \approx 3$  is taken here.

Parameter		Value
Mechanical resonance frequency	$f_{mr1}$	33000 Hz
Piezoelectric equiv. capacitor	$C_p$	176 nF
Series capacitor	$C_s$	528 nF
Parallel inductor	$L_p$	132 $\mu$ H
Series inductor	$L_s$	44 $\mu$ H

Table 4.1: Components design of LLCC filter fed by two-level HEM inverter

For driving the piezoelectric elements in the tangential mode of the PIBRAC motor, the components of the LLCC filter of the HEM inverter are given in Tab. 4.1.

#### 4. PWM-CONTROLLED DRIVING CONCEPT WITH LLCC-FILTER CIRCUIT

---

Parameter		Value
Active power	$P$	1519 W
Apparent power	$S$	1709 VA
Power factor	$PF$	0.89
RMS current of $L_s$	$I_{Ls}$	7.6 A
Current of switch S1	$I_{S1,RMS}$	5.4 A
	$I_{S1,Average}$	3.2 A

Table 4.2: Operating parameters of LLCC filter fed by two-level HEM inverter

Selected meaningful design variables are listed in Tab. 4.2 for the HEM inverter with LLCC filter at rated load.

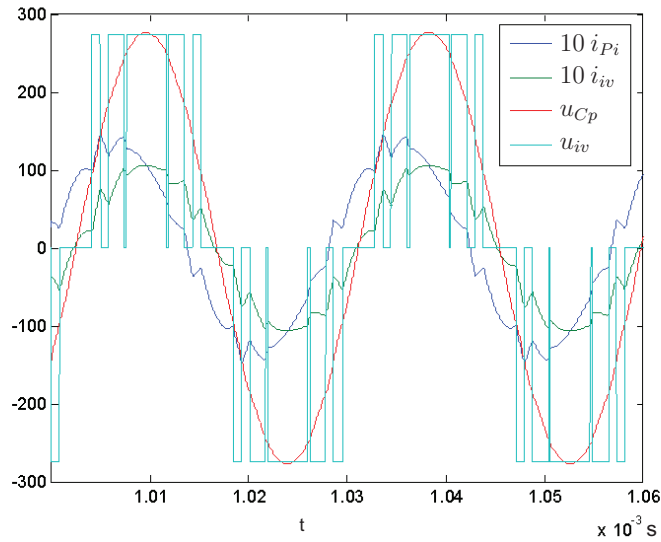


Figure 4.10: Currents and voltages of filter input and output

The simulated results of currents and voltages of filter input and output are shown in Fig. 4.10. Because the magnitude of the transfer function at the operating frequency  $f_{Op}$  is kept at 0 dB (see Fig. 4.3), the amplitude of the piezoelectric actuator voltage equals the amplitude of the fundamental component of the inverter output voltage.

A positive factor visible from simulation waveforms is that the phase shift between  $i_{iv}(t)$  and  $u_{iv}(t)$  is close to zero. This improves the power factor of the HEM inverter, but expectedly the inverter losses have increased corresponding

## 4.2 Advanced Pulse Width Modulation Design

the higher switching frequency, which is clearly a disadvantage emerging from using pulse width modulation. A detailed power analysis of the LLC-resonant inverter was carried out, results are presented in Fig. 4.11.

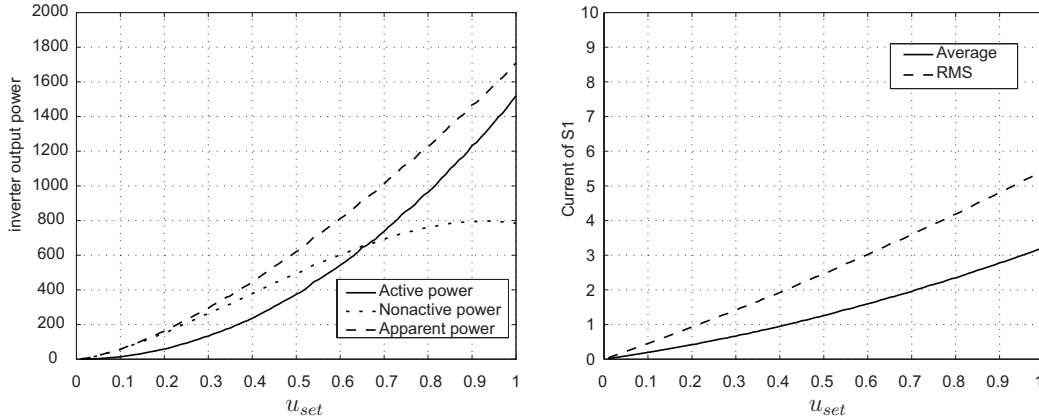


Figure 4.11: Power of LLC HEM inverter vs. set value  $u_{set}$  of normalized fundamental component of the inverter output voltage and switch-current average and RMS values

### 4.2.3 LLC Three-Level Carrier-Based PWM Inverter

In the field of inverter development the two-level voltage-fed inverter topology is the dominant topology used for all low- and medium-voltage systems for energy conversion. Special applications impose higher performance requirements on the converter such as highly dynamic performance, reduction of total harmonic distortion of output voltage and current, low electromagnetic interference and low weight. Therefore, multi-level inverters were investigated, selected and developed to satisfy these requirements for high power and high voltage applications [NTA81] [BS83] [Hol03] [BH05], especially if high filtering standards are set.

Contrasting to the advantages, the complexity of this topology is increased by the higher number of components. Nevertheless the single-phase three-level inverter is a reasonable solution for AC power supply in the power range of few kW, where the output quantity is an ultrasonic sinusoidal voltage.

#### 4. PWM-CONTROLLED DRIVING CONCEPT WITH LLCC-FILTER CIRCUIT

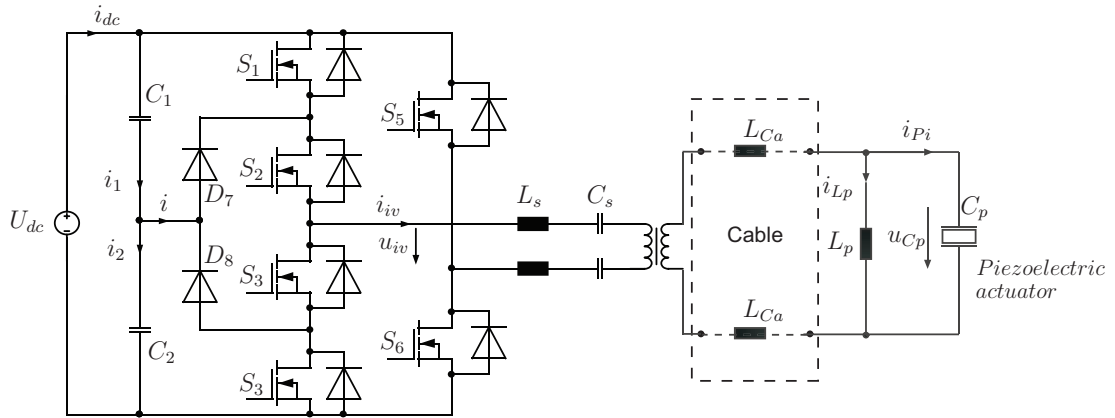
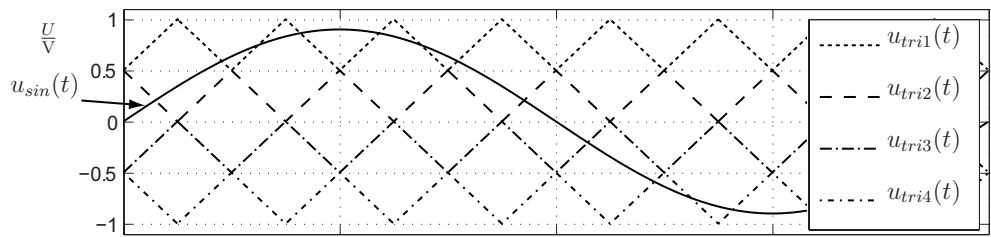
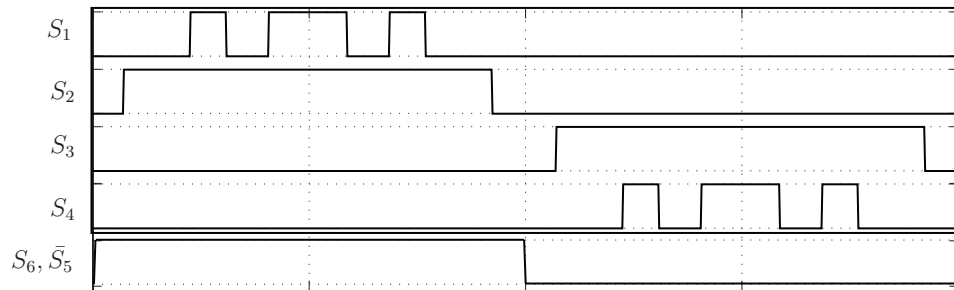


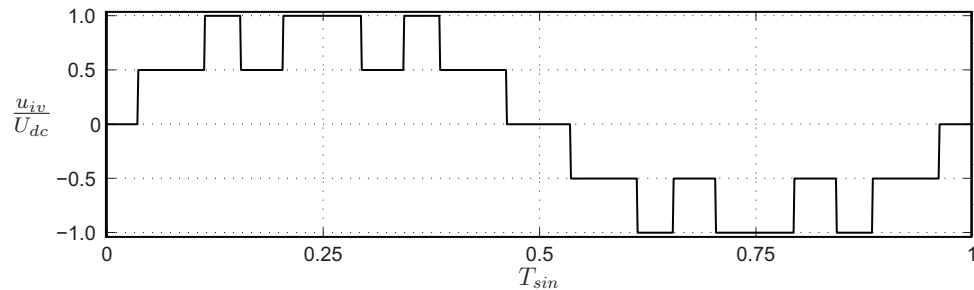
Figure 4.12: Hybrid three-level PWM inverter with LLCC filter



(a) Sinusoidal signal and triangular signals



(b) Driver signals



(c) Normalized inverter output voltage

Figure 4.13: Three-level carrier-based PWM scheme with waveforms, generated switching signals  $S_1 \dots S_6$  and inverter output voltage  $u_{iv}(t)$  for the case of power factor  $PF = 1$

## 4.2 Advanced Pulse Width Modulation Design

---

According to the analysis and design in Chapter 4.1.2, the transfer function of the designed LLCC filter has a magnitude equals 1 and a phase equals  $0^\circ$ , if the inverter is controlled to operate at the mechanical resonance frequency ( $f_{Op} = f_{mr1}$ ). Consequently the equivalent load of inverter behaves resistive and power factor  $PF$  is recognized as 1 for the analysis in the following chapter.

### 4.2.3.1 Three-Level PWM Inverter and its Carrier-Based PWM

Due to the rigid volume and weight limitation of the power supply in the airborne application, the proposed topology shown in Fig. 4.12 consists of a simplified three-level PWM inverter followed by a LLCC filter with an isolating transformer being integrated as part of the filter. This simplified three-level PWM inverter is constructed by a asymmetric topology, where the left leg of the PWM inverter is composed of four MOSFETs ( $S_1 - S_4$ ) used to generate high frequency PWM output voltage, while  $S_5$  and  $S_6$  forming the right two-level leg of the PWM inverter are employed to switch only the fundamental frequency of the mechanical vibration (as shown in Fig. 4.13).

Five voltage levels are generated across the LLCC filter and transformer by different switching states; even then the voltage stress of each device is only half of the input voltage. The multi-level circuit generates the piezoelectric actuator voltage with low THD and cuts down weight and volume of filter components by reducing the volt-second-product. The latter objective is largely weighted, as the appliance is for the aircraft market.

The driver signals of MOSFETs  $S_1$ ,  $S_2$ ,  $S_3$  and  $S_4$  are generated by three-level carrier-based PWM. The sinusoidal signal is defined using the set value  $u_{set}$  of the fundamental component as:

$$u_{sin}(t) = u_{set} \sin(\omega_{Op}t), \quad (4.19)$$

where  $\omega_{Op}$  approximates  $\omega_{mr1}$  according to the actuator operation condition. The triangular signals are defined as:

$$\begin{aligned} u_{tri1}(t) &= -0.25 u_{tri}(t) + 0.75 \\ u_{tri2}(t) &= 0.25 u_{tri}(t) + 0.25 \\ u_{tri3}(t) &= -0.25 u_{tri}(t) - 0.25 \\ u_{tri4}(t) &= 0.25 u_{tri}(t) - 0.75 \end{aligned} \quad (4.20)$$

#### 4. PWM-CONTROLLED DRIVING CONCEPT WITH LLCC-FILTER CIRCUIT

---

$$u_{tri}(t) = \sum_{i=1}^{n_p} u_{tri}^* \left( t - \frac{(i-1)T_{sin}}{n_p} \right) \quad (4.21)$$

$$u_{tri}^*(t) = \begin{cases} \left(1 - \frac{4n_p}{T_{sin}}t\right) V & 0 \leq t < \frac{T_{sin}}{2n_p} \\ \left(-3 + \frac{4n_p}{T_{sin}}t\right) V & \frac{T_{sin}}{2n_p} \leq t < \frac{T_{sin}}{n_p} \\ 0 V & \text{other} \end{cases} \quad (4.22)$$

where  $T_{sin} = 1/f_{sin} = 2\pi/\omega_{Op}$ , and the pulse number per period is  $n_p$ . Note that the frequency of the four triangular signals equals  $n_p f_{sin}$ . For example in Fig. 4.13  $n_p$  equals 8.

The driver signal of the switches  $S_1$ ,  $S_2$ ,  $S_3$  and  $S_4$  are attained in Eq. 4.23 by comparison of the respective triangular signals and the sinusoidal signal. Note that because the inverter output voltage and current are in phase ( $PF = 1$ ), there is no need to switch  $S_3$  complementally to  $S_1$  in the positive half-period ( $u_{sin}(t) > 0$ ), the current commutates between  $S_1$  and  $D_7$ , when  $S_1$  switches only. Due to the same reason  $S_2$  does not switch complementally to  $S_4$  in the negative half-period ( $u_{sin}(t) < 0$ ). Thus the switching frequencies of  $S_2$  and  $S_3$  are reduced comparing with the normal three-level PWM described in [NTA81].

$$\begin{aligned} S_1(t) &= \begin{cases} 1 & u_{sin}(t) > u_{tri1}(t) \\ 0 & \text{other} \end{cases} \\ S_2(t) &= \begin{cases} 1 & u_{sin}(t) > u_{tri2}(t) \\ 0 & \text{other} \end{cases} \\ S_3(t) &= \begin{cases} 1 & u_{sin}(t) < u_{tri3}(t) \\ 0 & \text{other} \end{cases} \\ S_4(t) &= \begin{cases} 1 & u_{sin}(t) < u_{tri4}(t) \\ 0 & \text{other} \end{cases} \end{aligned} \quad (4.23)$$

Contrary, the driver signals of switches  $S_5$  and  $S_6$  depend only on the sinusoidal signal  $u_{sin}(t)$ .

$$\begin{aligned} S_5(t) &= \begin{cases} 1 & u_{sin}(t) < 0 V \\ 0 & \text{other} \end{cases} \\ S_6(t) &= \begin{cases} 1 & u_{sin}(t) > 0 V \\ 0 & \text{other} \end{cases} \end{aligned} \quad (4.24)$$



#### 4. PWM-CONTROLLED DRIVING CONCEPT WITH LLCC-FILTER CIRCUIT

---

Fig. 4.14 shows the resulting switching signals and circuit states, in which the set value  $u_{set}$  equals 0.9 V and the LLCC filter and load have a power factor  $PF = 1$ . In 4.14(a) the state numbers represent the corresponding circuit state shown in Fig. 4.14(b-i). Except in the commutations between state 1 and state 3 and between state 5 and state 7, in the other commutations only the voltage stress of  $U_{dc}/2$  is to withstand for the switches  $S_1 - S_4$ . This allows reduction of the switching losses of the components. Note that during commutation from  $S_6$  to  $S_5$  three states are initiated: state 3  $\rightarrow$  state 4  $\rightarrow$  state 7. Later intervals between these states are decided by the load conditions, which determines the inverter output current  $i_{iv}(t)$  and phase shift between  $i_{iv}(t)$  and  $u_{iv}(t)$ .

It is the same situation during the commutation from  $S_5$  to  $S_6$  where another three states come into play, which are state 7  $\rightarrow$  state 8  $\rightarrow$  state 3. The frequency spectrum inverter output voltage using three-level carrier-based PWM is illustrated in Fig. 4.15 with pulse frequency  $f_p = 8 f_{sin}$  and  $f_p = 16 f_{sin}$ .

When the set value  $u_{set}$  is between 0 V – 0.5 V, the switches  $S_1$  and  $S_4$  are always turned off, while the switches  $S_2$  and  $S_3$  are turned on/off with the frequency of  $f_{sin}$ . These operating states are the same as in case of two-level CBM, but the output voltage has 8 pulses per period (if  $f_p = 8 f_{sin}$ ) or 16 pulses per period (when  $f_p = 16 f_{sin}$ ) and an amplitude of  $U_{dc}/2$  only. As comparison the two-level CBM (see Chapter 3.1.3) has only 10 pulses per period.

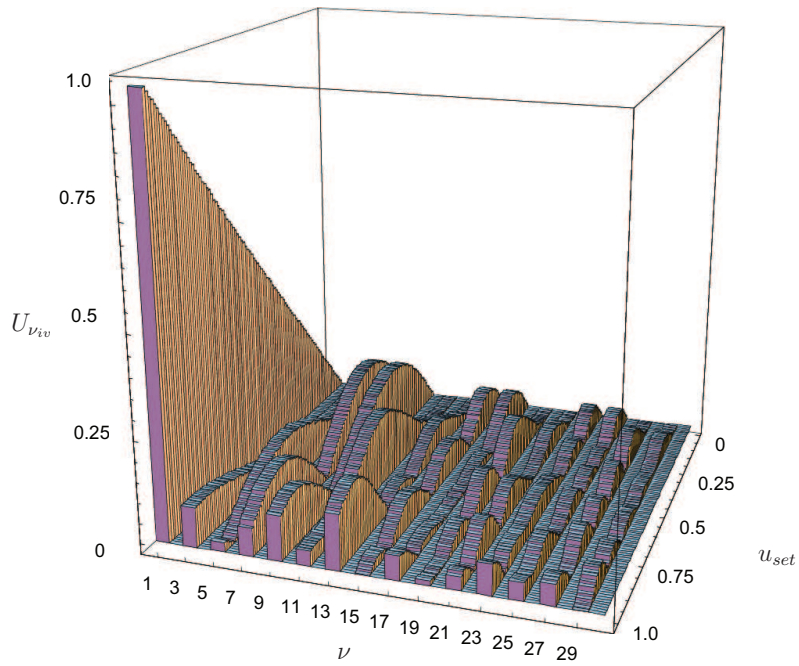
If the set value  $u_{set}$  is larger than 0.5 V, the switches  $S_1$  and  $S_4$  are also turned on/off, and the effective switching frequency of  $S_2$  and  $S_3$  is reduced. Additionally the inverter voltage is a sum of two voltage waveforms. Therefore the Fourier coefficient in Eq. 4.25 is the sum of the Fourier coefficients of each waveform.

$$u_{iv} = u_{1iv} + u_{2iv} \implies U_{\nu_{iv}} = U_{1\nu_{iv}} + U_{2\nu_{iv}} \quad (4.25)$$

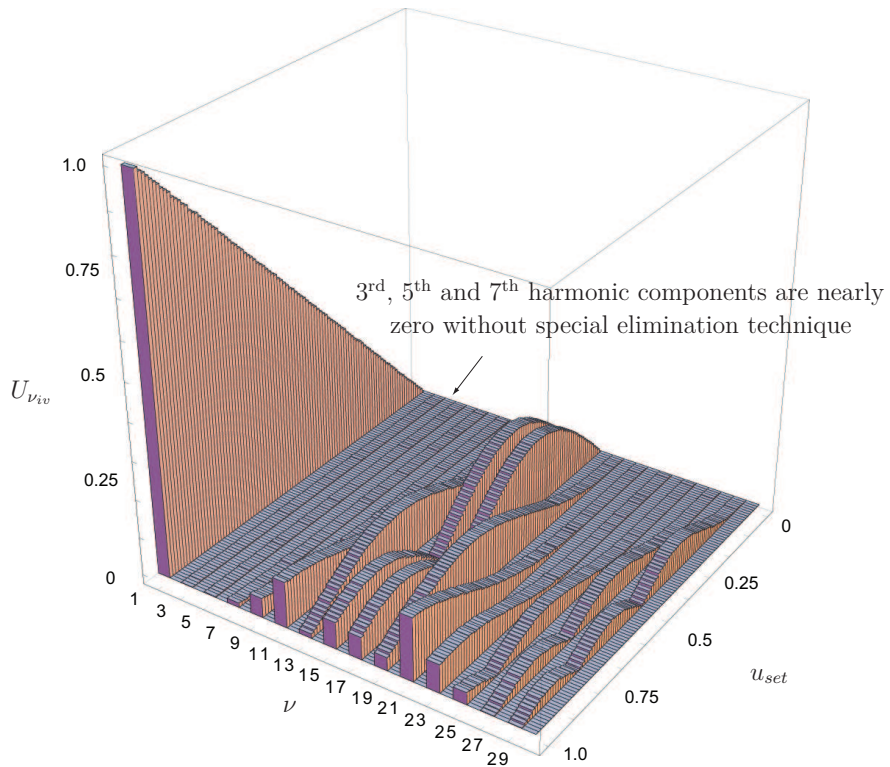
where  $u_{1iv}$  is generated when  $S_1$  and  $S_4$  are turned on/off, while  $u_{2iv}$  is produced when only  $S_2$  and  $S_3$  are turned on/off.

The switching frequency of each voltage  $u_{1iv}$  and  $u_{2iv}$  is lower than the original modulation frequency, consequently, more harmonic components are generated corresponding to the respective real switching frequency of each voltage waveform. Hence in case of  $f_p = 8 f_{sin}$  the harmonic 3<sup>rd</sup> and 5<sup>th</sup> are larger than those of

## 4.2 Advanced Pulse Width Modulation Design



(a) Pulse frequency ( $f_p = 8 f_{sin}$ )



(b) Pulse frequency ( $f_p = 16 f_{sin}$ )

Figure 4.15: Spectrum of output voltage using three-level CBM

## 4. PWM-CONTROLLED DRIVING CONCEPT WITH LLCC-FILTER CIRCUIT

---

two-level CBM described in Fig. 3.17, but the 7<sup>th</sup>, 9<sup>th</sup> and 11<sup>th</sup> harmonic are smaller.

### 4.2.3.2 Effects on LLCC Filter

The 3<sup>rd</sup> harmonic appearing in the inverter output voltage must be suppressed by the LLCC filter. However, using Eq. 4.7, the 3<sup>rd</sup> harmonic is expected to be reduced by  $-10$  dB:

$$\begin{aligned} |G(n, \alpha_{LLCC})| \Big|_{n=3} &= -10 \text{ dB} \\ \Rightarrow \alpha_{LLCC} &\approx 2 \end{aligned} \quad (4.26)$$

Parameter		Value
Mechanical resonance frequency	$f_{mr1}$	33000 Hz
Piezoelectric equiv. capacitor	$C_p$	176 nF
Series capacitor	$C_s$	352 nF
Parallel inductor	$L_p$	132 $\mu$ H
Series inductor	$L_s$	66 $\mu$ H

Table 4.3: Components design of LLCC filter fed by hybrid three-level inverter

Parameter		Value
Active power	$P$	1532 W
Apparent power	$S$	1615 VA
Power factor	$PF$	0.95
RMS current of $L_s$	$I_{Ls}$	8.1 A
Current of switch S1	$I_{S1,RMS}$	4.6 A
	$I_{S1,Average}$	2.1 A
Current of switch S2	$I_{S2,RMS}$	5.7 A
	$I_{S2,Average}$	3.5 A
Current of diode D7	$I_{D7,RMS}$	3.3 A
	$I_{D7,Average}$	1.4 A

Table 4.4: Operating parameters of LLCC three-level CBM inverter

For driving tangential-mode piezoelectric elements of PIBRAC motor, the filter components of the LLCC three-level CBM inverter are given in Tab. 4.3. The values of  $C_p$  and  $L_p$  are equal to those of the LLCC-resonant inverter and the

## 4.2 Advanced Pulse Width Modulation Design

LLCC two-level HEM inverter. The series inductor  $L_s$  becomes the smallest of compared inverter topologies, but the series capacitor has to be increased in order to attain the necessary robust behavior.

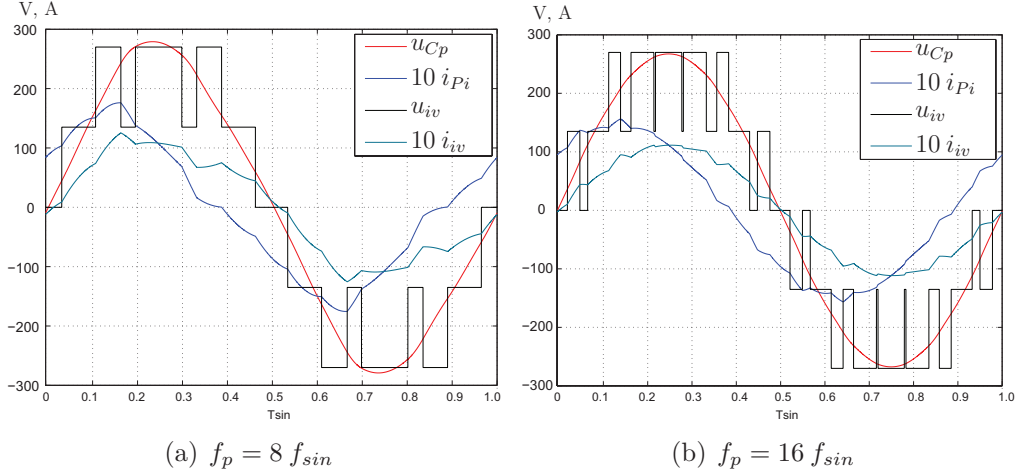


Figure 4.16: Simulation results of LLCC three-level CBM inverter

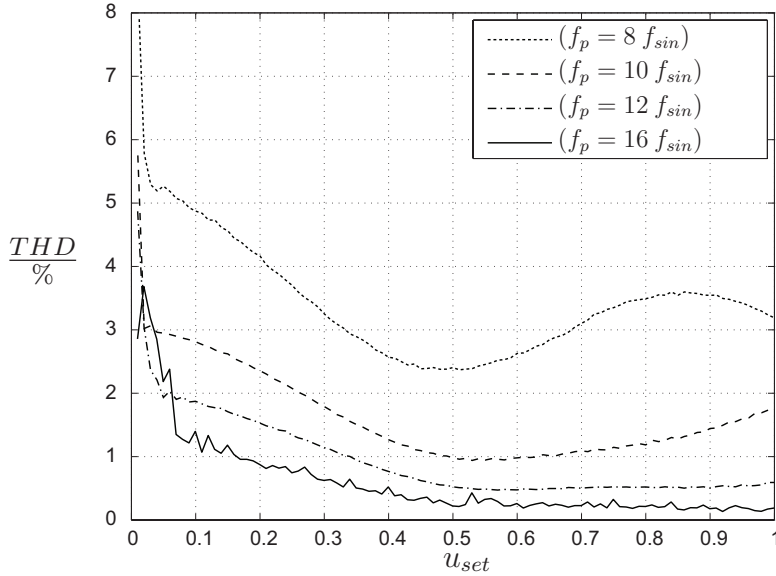


Figure 4.17: THD-characteristic curve of  $u_{Cp}(t)$  for different pulse frequencies

The simulations with rated load are carried out using two pulse frequencies at  $f_p = 8 f_{sin}$  and  $f_p = 16 f_{sin}$ . Results are shown in Fig. 4.16, wherefrom we observe that the ripple of inverter current  $i_{iv}(t)$  is smaller than the results of

## 4. PWM-CONTROLLED DRIVING CONCEPT WITH LLCC-FILTER CIRCUIT

LLCC two-level HEM inverter shown in Fig. 4.10, but there are more harmonics in  $u_{Cp}(t)$  and  $i_{Pi}(t)$  in case of low switching frequency (Fig. 4.16(a)). In Fig. 4.17 the total harmonic distortion (THD) values of the filter output voltage  $u_{Cp}(t)$  are compared using four of pulse frequencies.

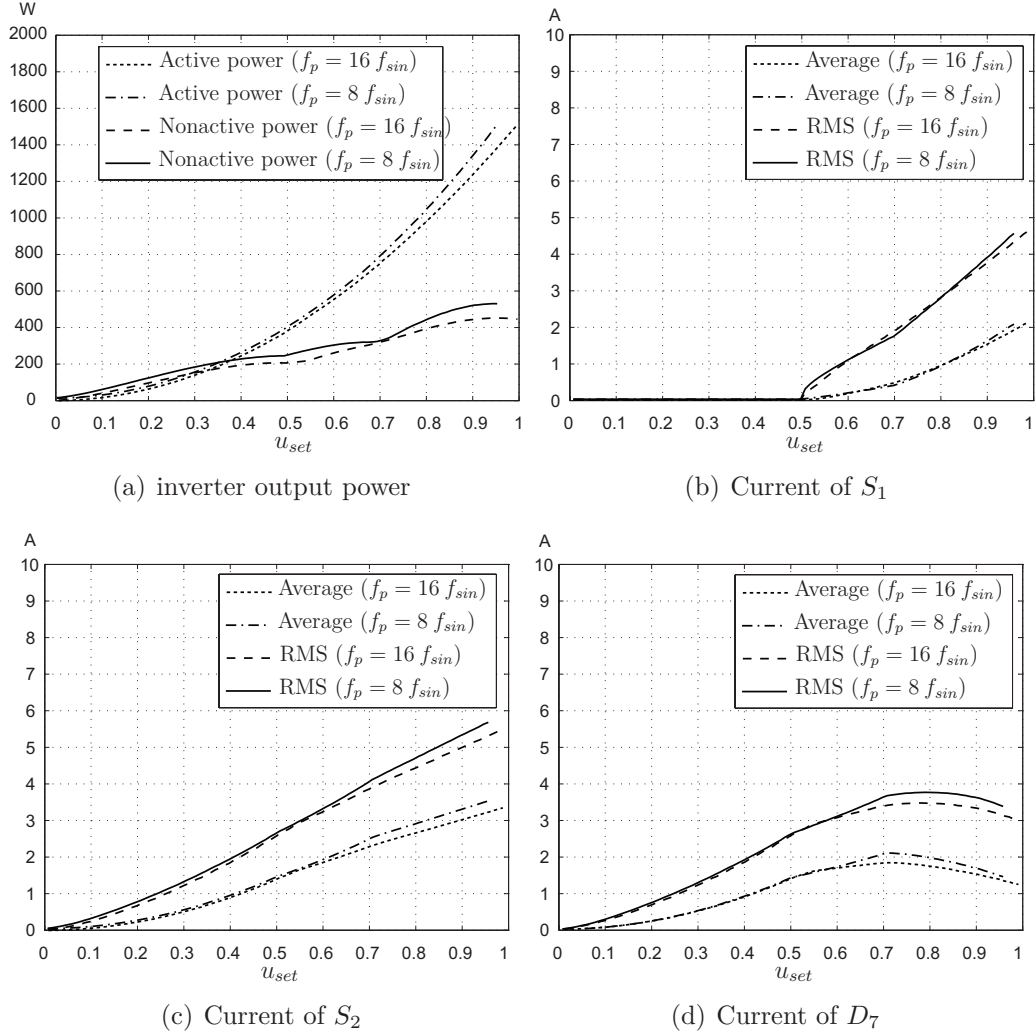


Figure 4.18: Calculated power and current loadings of LLCC three-level CBM inverter

A detailed power analysis of LLCC three-level inverter was carried out with  $u_{set}$  varied from 0 to 1.0, and the results of delivered power and current of components are presented in Fig. 4.18. For the reason of better comparison, the analysis is done for pulse frequencies  $8 f_{sin}$  and  $16 f_{sin}$ . With an increasing of the pulse

### 4.3 Evaluation and Comparison of Power Supply Topologies

frequency, on the one hand the nonactive power is decreased, due to the decreasing of harmonic components, on the other hand the set value  $u_{set}$  must be increased slightly, in order to achieve the same active power. For both frequencies the nonactive power of the LLCC three-level CBM inverter is smaller than that of the LLCC HEM inverter.

### 4.3 Evaluation and Comparison of Power Supply Topologies

In order to base the final decision about the inverter topology on a broad enough basis, a comparison including weight and volume of magnetic and capacitive components, total harmonic distortion (THD) of filter voltage and losses of power converters has to be conducted. These results are based on the discussion of the state-of-art power-supply topologies in Chapter 3.1 and the proposed driving concepts in Chapter 4; the selected power supplies are listed in Tab. 4.5.

		Filter		
		LC	LLCC	
Modulation	Resonant	-	Two-level topology	-
	CBM	Two-level topology	-	Three-level topology
	HEM	-	Two-level topology	-

Table 4.5: Selected power supplies for driving high-power piezoelectric actuators

Simulation results of selected power supplies with LC- or LLCC-type filter circuit at steady state are presented in Fig. 4.19 for one fundamental period, in which the voltage and current are simulated under the maximal active power of 1.5 kW.

#### 4.3.1 Switching Conditions

##### A. Two-level topology

The inverter topologies of a single phase 2-level full-bridge are depicted in Fig. 4.20, which is supplied by a DC-link voltage and consists of four MOSFETs arranged in two phase legs. To the centre point of each phase leg inverter the filter circuit is connected.

## 4. PWM-CONTROLLED DRIVING CONCEPT WITH LLCC-FILTER CIRCUIT

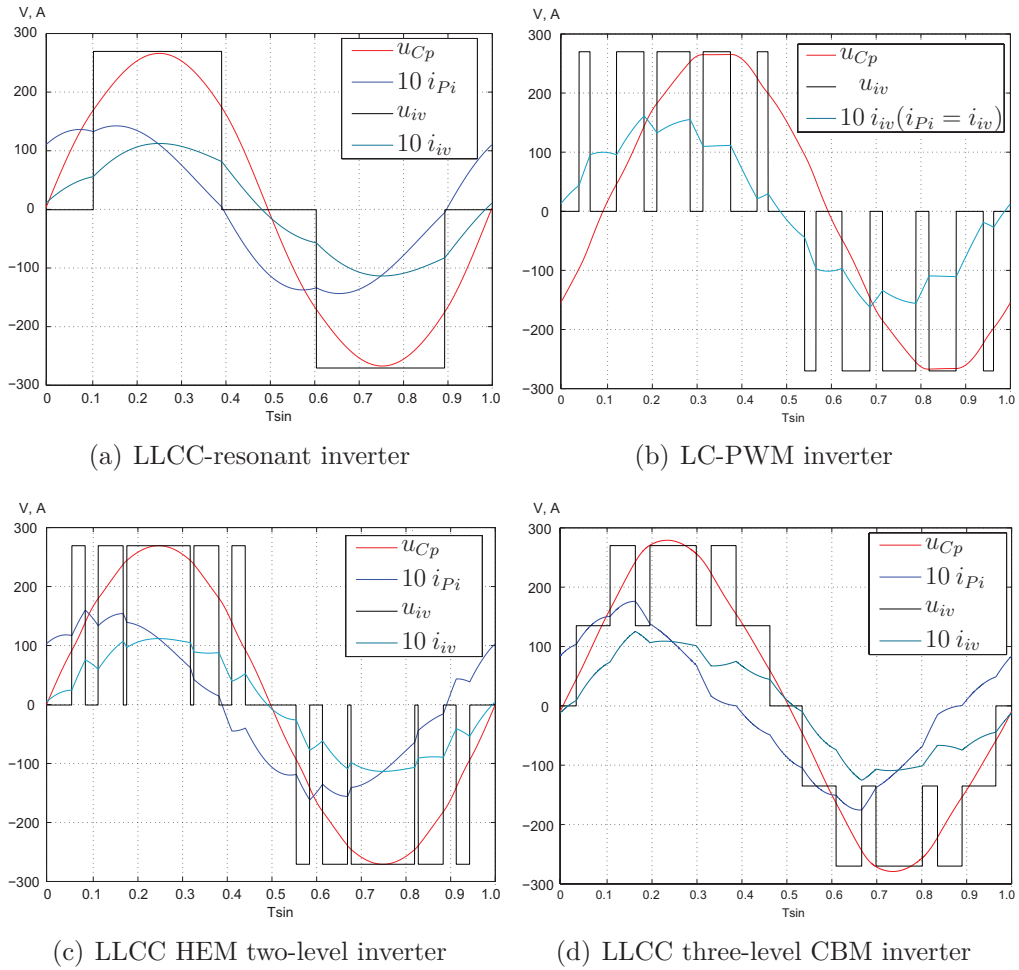


Figure 4.19: Simulation results of selected power supplies

A standard full-bridge inverter as shown in Fig. 4.20(a) is employed for designing the LC and LLCC-resonant inverter. With the maximum switching frequency of 33 kHz and the maximum power of 1.5 kW, one could have an option of choosing either MOSFETs or IGBTs for the switches.

To meet the design specifications of PIBRAC, the switching transistors need minimum ratings of 500 V and 20 A. In addition a switch is selected for producing minimum losses. Therefore, switches with lower resistance are more desirable.

For comparing the topologies, the inverters are designed using MOSFETs. A CoolMOS transistor (CoolMOS) SPP24N60C3 is chosen, which has the ratings of 650 V, 24 A and an on-state resistance of 0.16  $\Omega$  at a temperature of 25  $^{\circ}\text{C}$ .

### 4.3 Evaluation and Comparison of Power Supply Topologies

The body diode of the CoolMOS is used for free-wheeling of current instead of an extra parallel diode only in case of resonant-inverter operation.

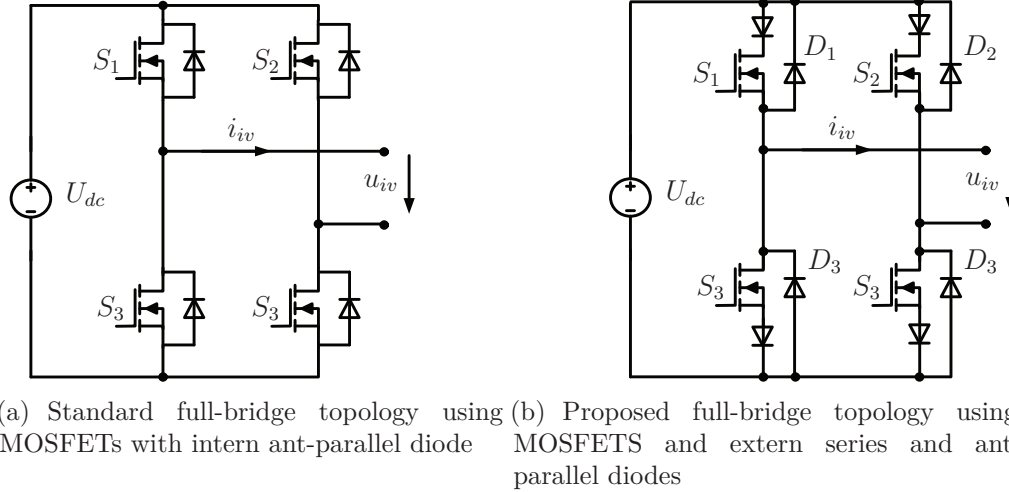


Figure 4.20: Single phase two-level full-bridge inverter

In case of PWM-controlled inverter, the full-bridge inverter with parallel diode as shown in Fig. 4.20(b) is applied. Because raising the switching frequency to the aforementioned range, the recovery time of the CoolMOSs body diode cannot be neglected, so an extra ultra-fast diode should be paralleled to the MOSFET and the body diode should be blocked by a series connected diode. For the parallel and series connected diodes the SiC Schottky diode IDT12S60C was selected.

#### B. Three-level topology

The hybrid three-level inverter topology is shown in Fig. 4.21. By using carrier-based PWM with a pulse number  $n_p$  per period, the switching frequency of  $S_1$  and  $S_4$  can be from 0 to  $(\frac{n_p}{2} - 1)f_{sin}$  varying with sinusoidal reference signal  $u_{sin}(t)$ , while the switching frequency of  $S_2$  and  $S_3$  can be from  $f_{sin}$  to  $(\frac{n_p}{2})f_{sin}$ . Differently, the  $S_5$  and  $S_6$  are switched only at  $f_{sin}$ , alternating only the polarity of the inverter voltage. Therefore IGBT or CoolMOS can be used for  $S_5$  and  $S_6$ , but for  $S_1 - S_4$  only CoolMOS can to be employed. Selected diodes  $D_7$  and  $D_8$  are SiC-Schottky diodes with very low reverse-recovery losses.

Note that there are nearly no commutations between  $S_1, S_4$  and their respective body diodes when  $S_1$  and  $S_4$  are turned off. The commutations from  $D_7$  and  $D_8$

## 4. PWM-CONTROLLED DRIVING CONCEPT WITH LLCC-FILTER CIRCUIT

to the body diodes of  $S_3$  and  $S_4$  (state 1 and state 3) and the commutations from  $D_8$  and  $S_3$  to the body diodes of  $S_1$  and  $S_2$  (state 5 and state 7) occur between one time to  $\frac{n_p}{2}$  times per period depending on  $u_{set}$ . In this application the required  $u_{set}$  is normally large enough, so these commutations are only one time per period (see Fig. 4.14). Hence the extra parallel diodes are not required for three-level topology. Moreover most of the switching components of the three-level topology have to sustain only half of the input DC-link voltage, yielding less voltage and switching stress and losses.

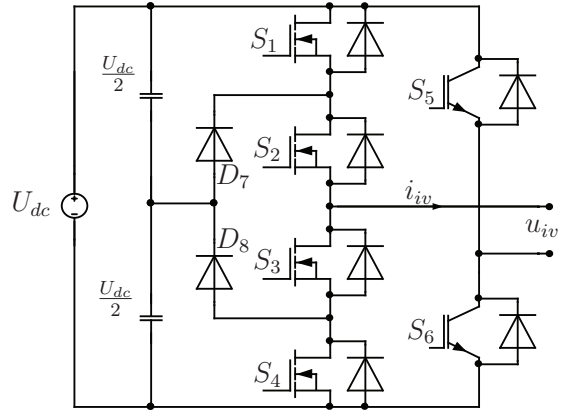


Figure 4.21: Three-level topology

The summary of the switching components required for each inverter is listed in Tab. 4.6.

	Resonant inverter	Two-level PWM inverter	Hybrid three-level PWM inverter
MOSFET (SPP24N60C3)	4	4	6
Diodes (IDT12S60C)	0	8	2

Table 4.6: Switching components

### 4.3.2 Preliminary Design of Filter Components

#### 4.3.2.1 Filter Components

Concluding from Chapter 3.1 and 4.1, two types of relevant filter topologies shown in Fig. 4.22, with isolating transformers being integrated into the resonant cir-

### 4.3 Evaluation and Comparison of Power Supply Topologies

circuits to provide galvanic isolation, qualify for the power-supply scheme. Both filter circuits can be operated either with square-wave modulation or with PWM modulation, as outlined above.

Power supply with LC-type filter is limited to combine with only PWM inverter, and the LC-resonant inverter is not considered for further investigation, because it requires largest inductive components and has the lowest power factor, and exhibits poor behavior in respect to robustness.

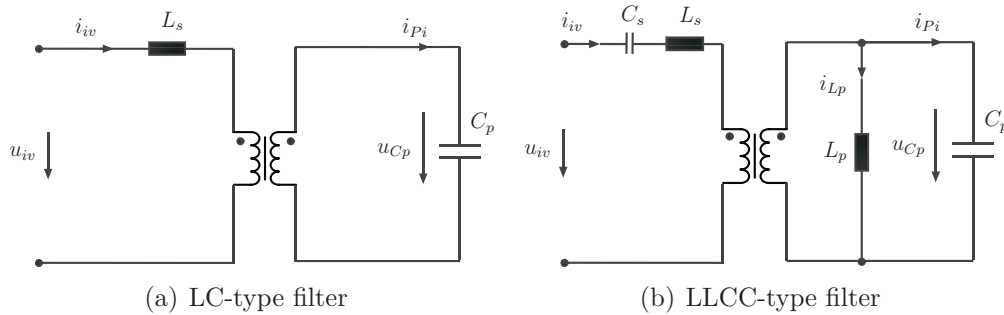


Figure 4.22: Filter Topologies

The design procedure of inductive components by using area products is illustrated in Appendix B.1. Volume and weight of magnetic components can be estimated by the core size appropriate for the application requirements. In Tab. 4.7 filter-component design parameters of selected power supplies are presented.

The LLCC-resonant filter requires a larger series inductor, compared with other PWM-controlled LLCC filters, but the capacitor  $C_s$  is smaller. As a result, this resonant inverter has a greater weight in summary.

Comparing the LLCC-resonant inverter and the LC-PWM inverter, the latter shows large reduction in size and weight of the inductive filter component. But unluckily this converter shows a poorer efficiency and larger transformer due to the missing reactive-power compensation, when driving a load with largely capacitive behavior.

From Tab. 4.7 we observe, that the LLCC-type filters driven by resonant inverter and the PWM inverter have the same transformer in size and volume, which is smaller than with PWM-controlled LC-type filter. This result is a benefit from the local reactive-power compensation. By comparing the series inductor

## 4. PWM-CONTROLLED DRIVING CONCEPT WITH LLCC-FILTER CIRCUIT

---

in the LLCC-PWM inverter and in the LLCC-resonant inverter, the former is reduced in volume and weight due to the higher switching frequency. Furthermore the core losses are reduced with the decreasing core size.

		LLCC-resonant inverter	LC-PWM inverter	LLCC two-level HEM inverter	LLCC three-level CBM inverter
Parallel capacitor	$C_p$	176 nF	176 nF	176 nF	176 nF
Series capacitor	$C_s$	176 nF	-	528 nF	352 nF
Series inductor	$L_s$	132 $\mu$ H	53 $\mu$ H	44 $\mu$ H	66 $\mu$ H
	Core	EE 55/28/21, 2*215 g	EE 42/21/20, 2*116 g	EE 32/16/11, 2*37 g	EE 36/18/11, 2*50 g
	Wire	407 g	315 g	80 g	80 g
	Loss	10 W	6 W	2 W	2 W
Parallel inductor	$L_p$	132 $\mu$ H		132 $\mu$ H	
	Core	EE 42/21/15, 2*88 g		EE 42/21/15, 2*88 g	
	Wire	64 g	-	64 g	
	Loss	3 W		3 W	
Transformer	Core	ETD 42/21/15, 2*88 g	ETD 55/28/25, 2*256 g	ETD 42/21/15, 2*88 g	
	Wire	214 g	198 g	214 g	
	Loss	6 W	8 W	6 W	
Filter weight		1.5 kg	1.3 kg	0.8 kg	0.8 kg

Table 4.7: Design results of filter components

### 4.3.2.2 Filter Performance

The highest robustness of the transfer function gain versus variations of operating conditions, influenced by temperature, mechanical load etc., can be achieved by using the LLCC-filter circuit.

The LLCC PWM-controlled inverter is characterized by a faster dynamic response compared with the LLCC-resonant inverter. If the LLCC-filter circuit is driven by a PWM inverter, it is evident that the dynamics are improved largely (see Chapter 6.2.4).

#### 4.3.3 Power Factor

Power factor (see Appendix A.1) is one of the major criteria for evaluating the performance of a power supply, due to its significance for the electrical grid and prediction of losses. In Fig. 4.23 the power factors of the selected power supplies are presented for comparison.

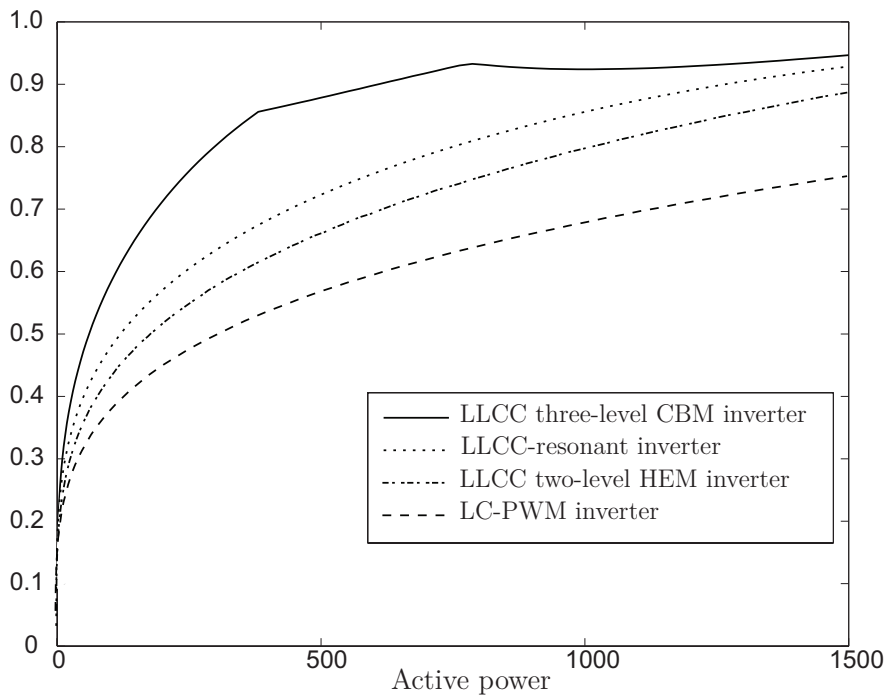


Figure 4.23: Power factors of selected power supplies

The LC-PWM inverter shows the largest phase delay between inverter voltage  $u_{iv}(t)$  and current  $i_{iv}(t)$ , which is known from simulation results in Fig. 4.19. This implies largest reactive power to be delivered by the inverter. In contrary, the LLCC filter provides local reactive-power compensation, so that the supplies with LLCC filter have better power factor compared with LC-PWM inverter. The low reactive power results in reduced current stress of inverter and cable.

The three-level topology provides five voltage levels to the LLCC filter. This voltage waveform enables a reduction of nonactive power and thus of the volume of the filter components compared to that of the two-level topology, due to smaller

## 4. PWM-CONTROLLED DRIVING CONCEPT WITH LLCC-FILTER CIRCUIT

---

volt-seconds across the inductors. So the LLCC three-level CBM inverter provides the best power factor of the selected power supplies.

Compared with the resonant inverter, the nonactive powers of LLCC HEM inverter is a little bit larger than that of LLCC-resonant inverter, when the same active power is delivered. This is due to the fact that the square-wave modulation generates a voltage fundamental component slightly larger than the HEM at the same set value  $u_{set}$ ; thus the RMS of  $u_{iv}(t)$  of resonant inverter is smaller than that of the HEM inverter when the same active power is delivered from inverters.

### 4.3.4 Total Harmonic Distortion (THD)

The importance of a low total harmonic distortion (THD, see Appendix A.4) results from the fact that the life time of the piezoelectric ceramic stacks suffers from too high THD of the exciting voltage. So the THD values of the selected power supplies are analyzed and used as one criterion of judgement, in order to evaluate the performance of the designed inverters and the filter circuits.

#### 4.3.4.1 THD of Inverter Output Voltage

The inverter output voltage  $u_{iv}(t)$  is analyzed up to the 21th harmonic and the THD characteristic curves are presented in Fig. 4.24, where the pulse number of all LLCC PWM-controlled inverter equals 10.

Note that the THD of  $u_{iv}(t)$  depends only on the inverter behavior itself (pulse width modulation, delay-time of switching transistor), while the THD of the filter output voltage  $u_{Cp}(t)$  is decided by the inverter as well as the filter characteristic.

THD curves are dependent on the set value  $u_{set}(t)$  of the fundamental component of the inverter output voltage. Due to the different inverter characteristics and their modulation schemes, there are two different set values here.

- Resonant inverter and two-level HEM inverter:  $u_{set}(t)$  equals the normalized amplitude of the fundamental component of  $u_{iv}(t)$ .

$$u_{set} = \frac{U_{1iv}^*}{U_{dc}}$$

- Two-level and three-level CBM inverter using CBM:  $u_{set}(t)$  equals the amplitude of the sinus reference signal.

$$u_{set} = U_{sin}$$

### 4.3 Evaluation and Comparison of Power Supply Topologies

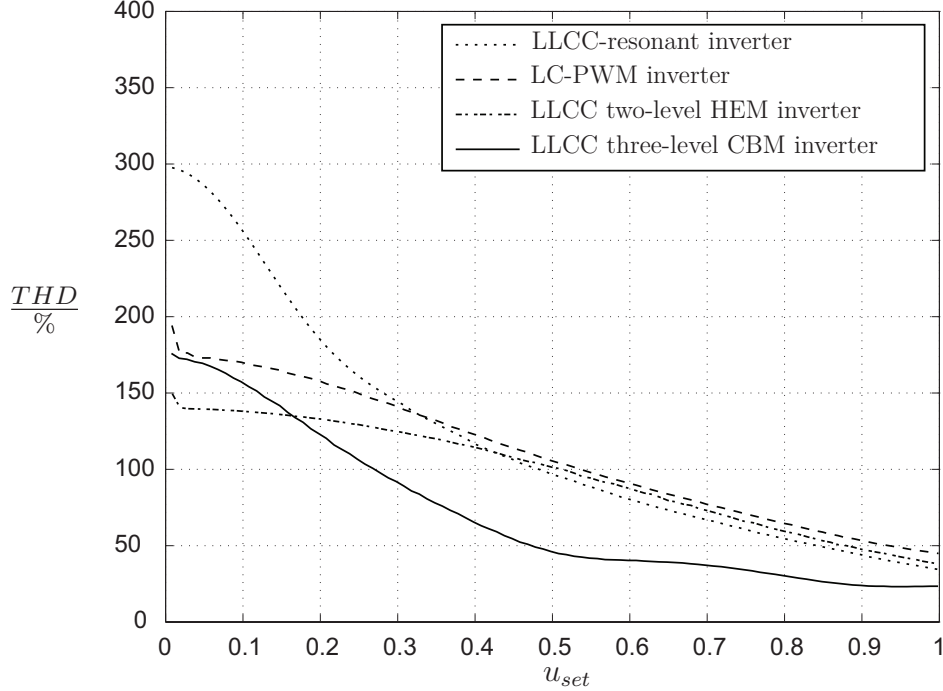


Figure 4.24: THD curves of output voltage  $u_{iv}(t)$  up to 21th harmonic of selected inverter

Due to the advantage of five levels of the inverter output voltage, the three-level CBM produces the lowest THD. The difference of two-level PWM inverter output voltage  $u_{iv}(t)$  is very small between using HEM and using CBM. The reason for this is that even though in case of HEM the selected low-order harmonic components are eliminated using precalculated switching angles, the amplitudes of other higher-order harmonic components are larger than using CBM. Hence, the resulting THD curves of both modulation schemes equal each other nearly.

Even though the resonant inverter has less THD than the two-level PWM inverter when  $u_{set}$  is larger than 0.5, the dominating harmonics are of lower order than with the PWM inverter and thus more disturbing. This increases the filter demand.

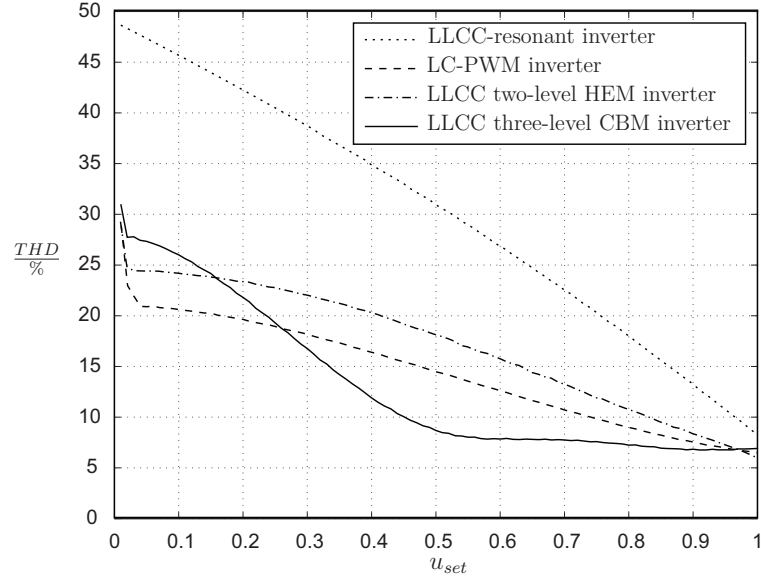
#### 4.3.4.2 THD of Filtered Voltages

As discussed before, the filter output voltage THD is determined by the spectrum of  $u_{iv}(t)$  and the transfer function of the filter circuit. In Fig. 4.26 the four

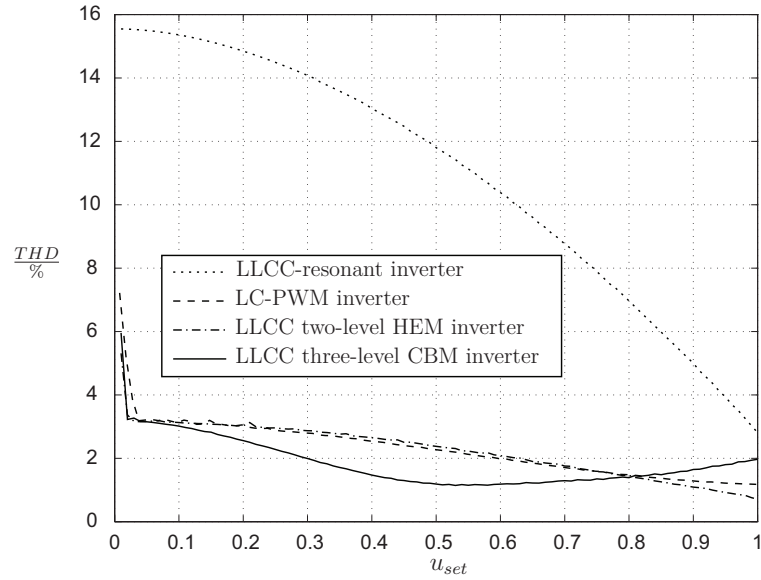
#### 4. PWM-CONTROLLED DRIVING CONCEPT WITH LLCC-FILTER CIRCUIT

---

filter transfer functions are illustrated, where all gain curves decline nearly with  $-40$  dB/decade at frequencies larger than the 3<sup>rd</sup> harmonic.



(a) THD of  $i_{iv}(t)$



(b) THD of  $u_{Cp}(t)$

Figure 4.25: Comparison of THD after filter circuits

The THD characteristic curves of inverter current  $i_{iv}(t)$  and piezoelectric actuator voltage  $u_{Cp}(t)$  are calculated and shown in Fig. 4.25(a) and 4.25(b), where the in-

### 4.3 Evaluation and Comparison of Power Supply Topologies

verter set values are  $u_{set} = 0.0$  V to 1.0 . In summary, the THD characteristics of PWM-controlled power supplies are smaller than of square-wave controlled power supplies, even though the LLCC-resonant filter provides the largest attenuation of all candidates.

The LLCC HEM inverter is designed with the smallest harmonic suppressing ratio, but the advantage of the HEM is, that it has a smaller THD of  $i_{iv}(t)$  and  $u_{Cp}(t)$ , because the 3<sup>rd</sup>, 5<sup>th</sup>, 7<sup>th</sup>, and 9<sup>th</sup> harmonics are eliminated, in contrast to the LC-PWM inverter.

The LLCC three-level CBM inverter attains the smallest THD of  $i_{iv}(t)$  and  $u_{Cp}(t)$  in a wide range of  $u_{set}(t)$ , but since still low-order harmonic component exist (see Chapter 4.2.3.2 ), the THD values of  $i_{iv}(t)$  and  $u_{Cp}(t)$  are larger than for LLCC HEM inverter.

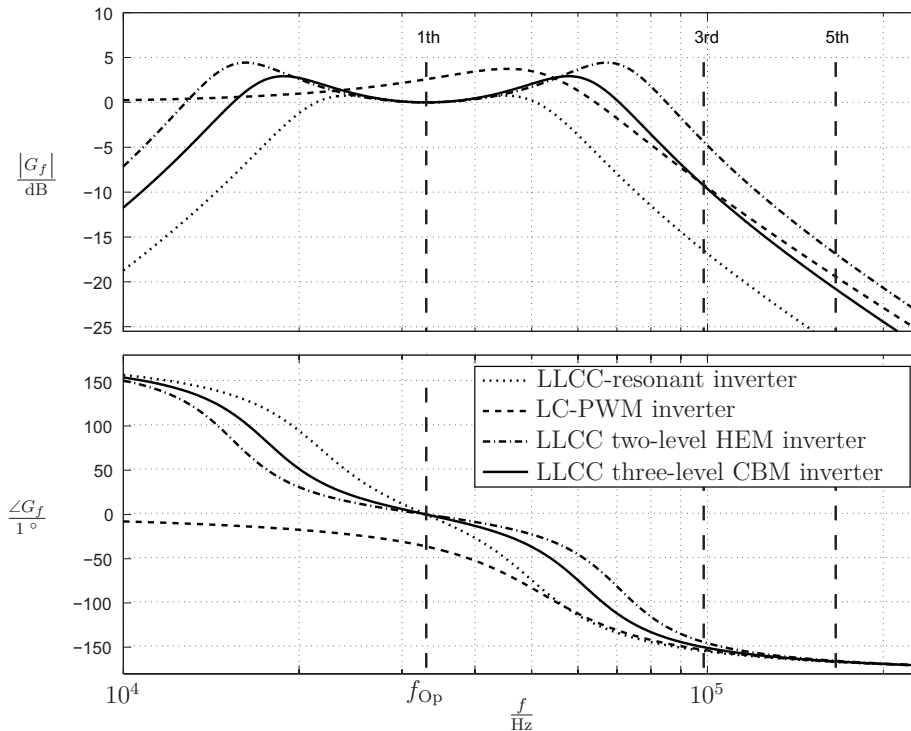


Figure 4.26: Filter transfer function  $u_{Cp}(s)/u_{iv}(s)$  of selected power supplies

## 4. PWM-CONTROLLED DRIVING CONCEPT WITH LLCC-FILTER CIRCUIT

### 4.3.5 Estimation of Efficiency and Weight

#### A. Efficiency

The estimation of inverter efficiency is conducted by calculating the dominant losses of magnetic components and power switching components (See Appendix B.2), which are conduction, switching and gate-charge losses of MOSFETs. In Fig. 4.27, the resulting efficiencies of four inverters are presented versus output power. Losses are then processed to determine the required cooling. This is again utilized to determine the total weight of inverter.

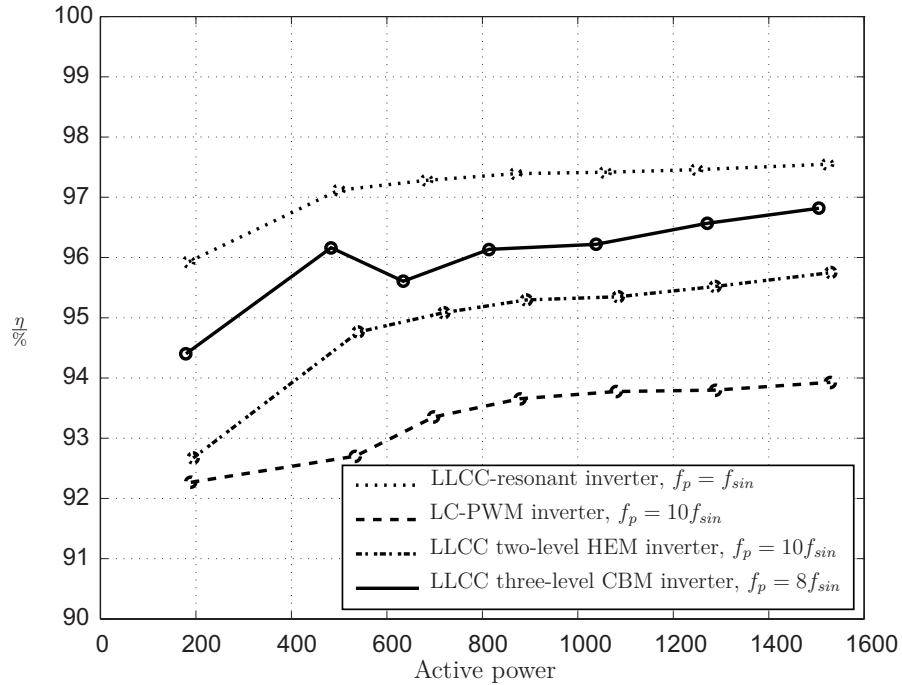


Figure 4.27: Comparison of estimated efficiency

Inspection of Fig. 4.27 indicates that the LLCC-resonant inverter generates the lowest losses due to the lowest switching frequency, whereby the highest efficiency results in contrast to the LC-PWM inverter, which produces higher losses than the other PWM inverters, due to its largest apparent power.

#### B. Volume and weight

Volume and weight of the inverters are mainly decided by the number of components and heat sink. The three-level inverter consists of more active switching

### 4.3 Evaluation and Comparison of Power Supply Topologies

	Resonant inverter with LLCC filter	Two-level CBM inverter with LC filter	Two-level HEM inverter with LLCC filter	Three-level CBM with LLCC filter
Inverter	0.7 kg	1.1 kg	0.9 kg	1.0 kg
Filter	1.5 kg	1.3 kg	0.8 kg	0.75 kg
Sum	2.2 kg	2.4 kg	1.7 kg	1.75 kg

Table 4.8: Weight estimation of power supplies for MM-USM tangential mode (one motor)

components, compared with the two-level PWM inverter, which requires more passive switching components (diodes). The LLCC-resonant inverter generates lowest losses, hence requires lowest cooling efforts, but requires heaviest filter magnetic components due to its lowest switching frequency. In summary the LLCC HEM inverter is the best candidate in terms of weight, but the three-level solution with LLCC filter is very close to it.

	LLCC-resonant inverter	LC two-level PWM inverter	LLCC two-level HEM inverter	LLCC three-level CBM inverter
Volume / weight	0	–	++	+
Total harmonic distortion (THD)	–	0	++	+
Electrical stress	+	–	0	++
Power factor	+	–	0	++
Efficiency and efforts for cooling means	++	–	0	+
Robust operating behavior	0	–	++	+
Dynamics to be attained	–	+	++	+
Topology complexity	++	+	0	–

Table 4.9: Comparison of different inverters, filters and modulation schemes (– poor, 0 medium, + good, ++ excellent)

#### 4.3.6 Comparison Results

In the previous chapters, the power supply candidates have been discussed and analyzed, in order to enable a technical-criteria-based decision about which topol-

## 4. PWM-CONTROLLED DRIVING CONCEPT WITH LLCC-FILTER CIRCUIT

---

ogy suits best for supplying MM-USM. Detailed comparisons are summarized in Tab. 4.9 and supplemented by weighting and additional criteria (gate drives, snubbers, EMC-filters, starting and stopping circuitry, fusing and overcurrent and other protection means are not included).

### 4.4 Experimental Validation

#### 4.4.1 Prototype Design

An experimental inverter prototype of 1.5 kW rated power was built to verify the operating principle of the LLCC PWM inverter, see Fig. 4.28, where the proposed hybrid three-level inverter is employed in the power inverter topology shown in 4.29. Due to the fact that the target motor is still under construction, an equivalent load consisting of capacitors and resistors was used for testing instead.

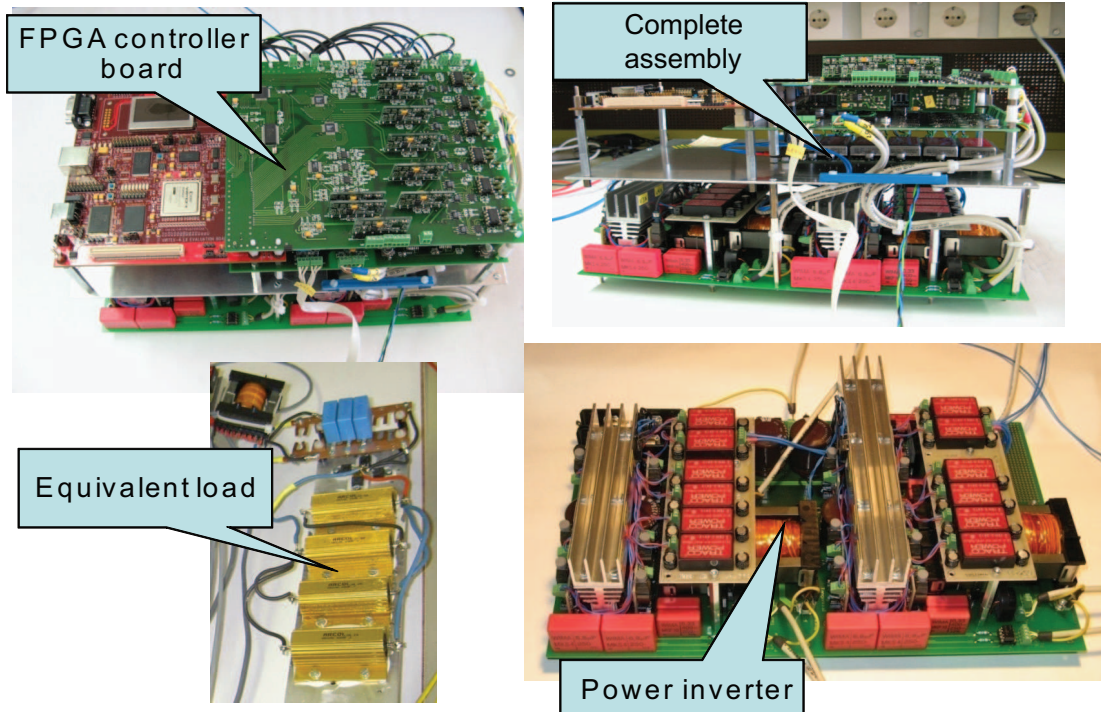


Figure 4.28: Power-supply prototype

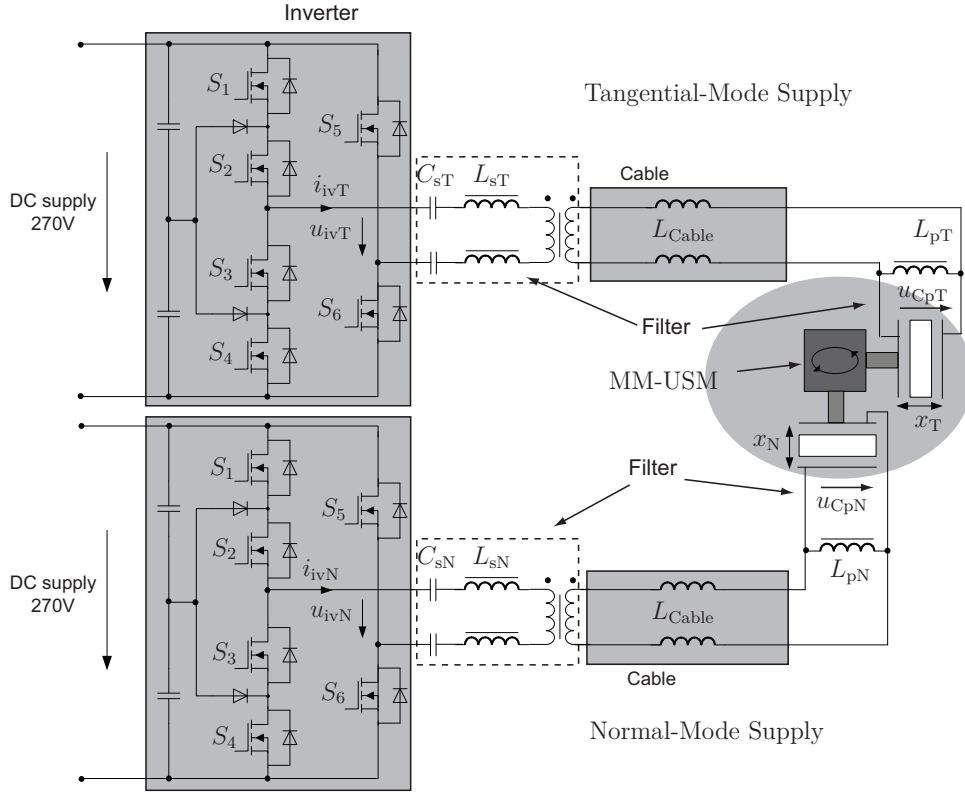


Figure 4.29: Power supply system structure

#### 4.4.1.1 Power Circuitry and Control Interface

Even though the normal-mode piezoelectric actuators need to be supplied by power smaller than 100 W, the inverters of both the tangential-mode and of the normal-mode piezoelectric actuator are built identically in order to provide the possibility to test with different modulation schemes.

S1 - S6	CoolMOS	SPP24N60C3
D7 - D10	SiC Schottky	IDT12S60C
Parallel inductor	$L_p$	132 $\mu\text{H}$
Series inductor	$L_s$	66 $\mu\text{H}$
Series capacitor	$C_s$	330 nF
Parallel capacitor	$C_p$	136 nF – 204 nF
Resistive load	$R'_p$	20 $\Omega$ – 400 $\Omega$

Table 4.10: Switching components

The switching components are listed in Tab. 4.10. An equivalent load consisting

## 4. PWM-CONTROLLED DRIVING CONCEPT WITH LLCC-FILTER CIRCUIT

of a parallel capacitor  $C_p$  and a resistive load  $R'_p$  was used for testing, as mentioned before.

The maximum amplitude of the output voltage is 270 V at a frequency of 33 kHz, with a DC-bus voltage of 270 V which is supplied from the common aircraft DC power grid.

### 4.4.1.2 Control Circuitry and Auxiliary Functions

The FPGA device (Xilinx Vertex4-xc4vsx35) is employed and developed with the help of the Xilinx System Generator Toolbox on the Matlab-Simulink platform. The modulation was subdivided into several components on the FPGA, which are described by the block diagram shown in Fig. 4.30. Temperature and error monitoring is also included, to ensure reliable operation.

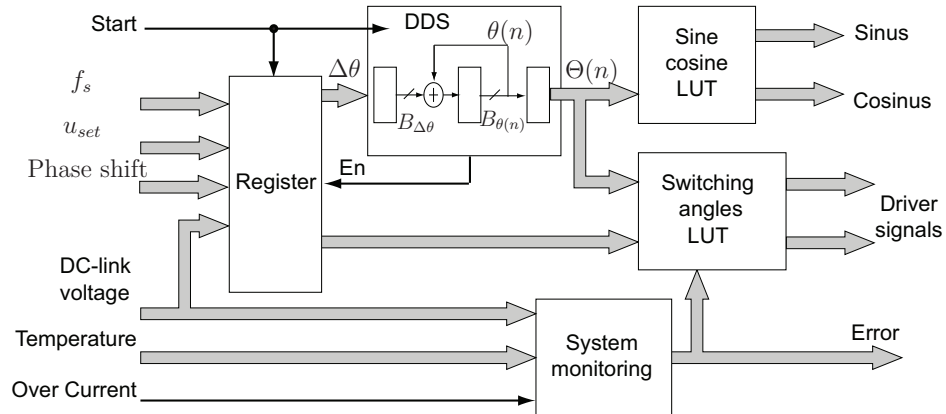


Figure 4.30: Block diagram of the components of harmonic elimination modulation

One significant component is the Direct Digital Synthesis (DDS) [xil06]. The DDS output signal  $\Theta(n)$  is a sawtoothed periodic variable and represents the phase angle of the modulation. The output frequency  $f_{DDS}$  of the DDS is a function of the FPGA system clock frequency  $f_{clk}$ , the number of bits  $B_{\theta(n)}$  in the phase accumulator and the phase increment value  $\Delta\theta$ . The output frequency is defined as  $f_{DDS} = f_{clk}\Delta\theta/2^{B_{\theta(n)}}$ . The frequency resolution can be determined using the following equation  $\Delta f = f_{clk}/2^{B_{\theta(n)}}$ . Consider a DDS with the following parameters  $B_{\theta(n)} = 32$ ,  $f_{clk} = 100$  MHz, then a frequency resolution  $\Delta f = 0.023$  Hz results. If  $\Delta\theta$  is set to 1417339,  $f_{DDS}$  equals 33 kHz .

In Fig. 4.30 the trigger block enables changing of set values (voltage, frequency) at the end of a period. The switching angles depending on the voltage reference as well as the sine and cosine values are stored in look-up tables (LUT), where the sawtooth signal  $\Theta(n)$  is used as phase input. The sine and cosine signals are used for phase-sensitive demodulation of the original measurement signals as described above.

### 4.4.2 Measurements with Three-Level CBM

Resulting experimental waveforms of three-level CBM are shown in Fig. 4.31, where pulse frequency  $f_p = 8f_{sin}$ . The waveform shows, that the voltage across the piezoelectric actuators  $u_{CpT}$  looks closer to sinusoidal as in the simulation, only the phase between  $i_{ivT}$  and  $u_{ivT}$  is slightly different. However, the power factor of the power supply is nearly unity. Though there are slight differences between simulation and measurements, the comparison is quite satisfactory.

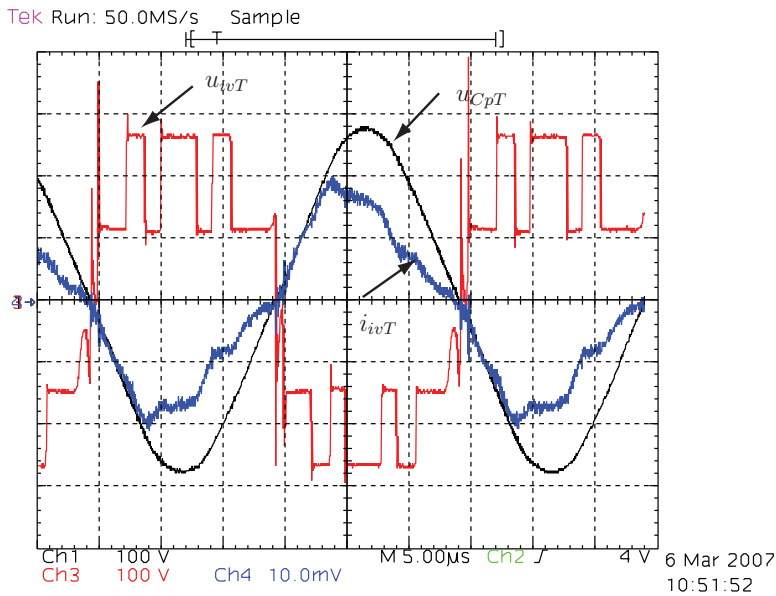


Figure 4.31: Experimental waveforms of the prototype using three-level CBM,  $f_p = 8f_{sin}$ .  
 Voltage of piezoelectric actuators ( $u_{CpT}$ , 100 V/div)  
 Output voltage of inverter ( $u_{ivT}$ , 100 V/div),  
 Output current of inverter ( $i_{ivT}$ , 5 A/div)

## 4. PWM-CONTROLLED DRIVING CONCEPT WITH LLCC-FILTER CIRCUIT

### 4.4.3 Measurements with Two-Level HEM

Resulting experimental waveforms of LLCC PWM inverter using two-level HEM (using  $f_p = 10f_{sin}$ ) are shown in Fig. 4.32, showing that the voltage across the piezoelectric actuators  $u_{CpT}$  is also nicely sinusoidal as in the case of three-level CBM.

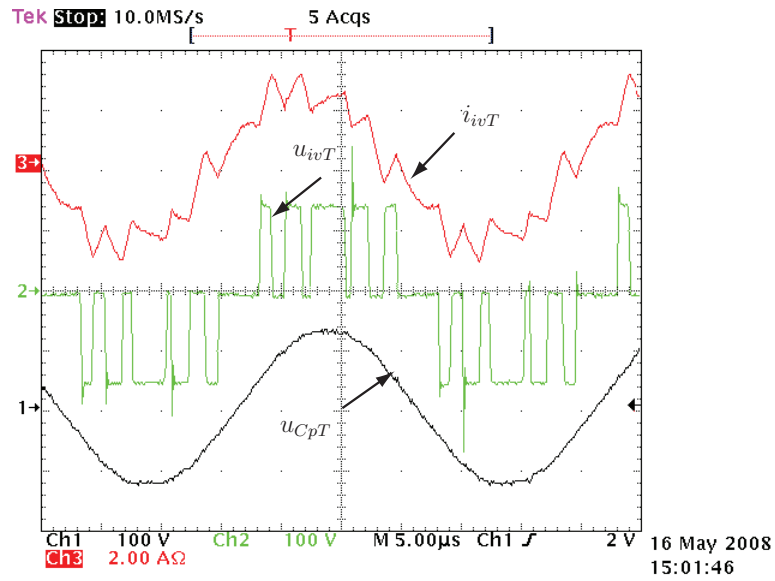


Figure 4.32: Experimental waveforms of prototype using two-level HEM. Voltage of piezoelectric actuators ( $u_{CpT}$ , 100 V/div), Output voltage of inverter ( $u_{ivT}$ , 100 V/div), Output current of inverter ( $i_{ivT}$ , 2 A/div)

However, the inverter current  $i_{ivT}$  has a larger saw-toothed ripple than in the case of three-level CBM, because the pulse voltage amplitude of  $u_{ivT}$  is double for the two-level full-bridge inverter.

The measured spectra of the piezo-actuator voltage  $u_{CpT}$  and the filter input voltage  $u_{ivT}$  are shown in Fig. 4.33. Note that the 3<sup>rd</sup>, 5<sup>th</sup>, 7<sup>th</sup> and 9<sup>th</sup> harmonic components are not zero as in the simulation in Fig. 4.9. This is caused by the delay time of the MOSFET drivers, which reduces the switching angles slightly, compared to calculation.

Even though the higher harmonic components are dominating in the harmonic distortion of  $u_{ivT}$ , we notice that the higher harmonic components of  $u_{CpT}$  are well

suppressed with increasing frequency due to the 2<sup>nd</sup> order band-pass characteristic of the LLC-filter circuit.

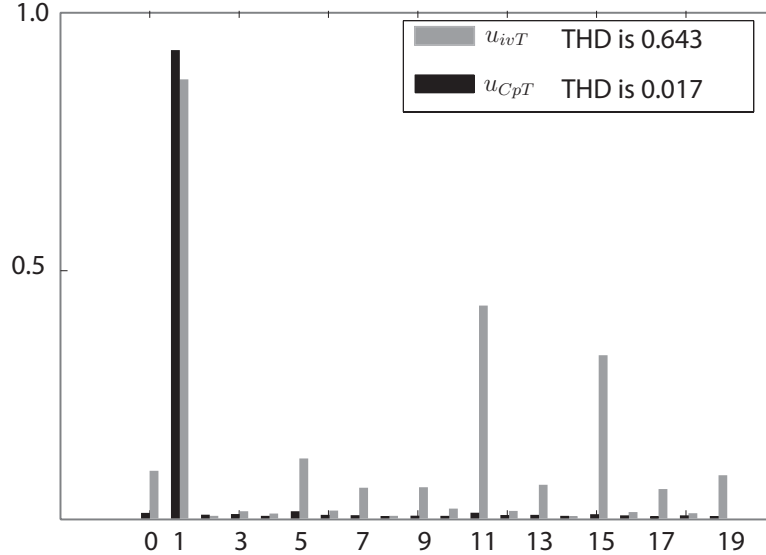


Figure 4.33: Frequency spectra of  $u_{CpT}$  and  $u_{ivT}$  using two-level HEM with  $f_p = 10f_{sin}$

## 4.5 Summary

The results demonstrate that the power supplies composed of the LLC three-level CBM inverters and the LLC two-level HEM inverters have qualified as most promising solutions for the power supply. The LLC PWM inverter is more complex, but produces less THD, has smaller and lighter filter components and a larger bandwidth compared with a square-wave controlled resonant inverter.

A thoroughly designed LLC filter exhibits the required robustness in respect to parameter variations and enables the reduction in size of filter components and the utilization of cable parasitics. The cable weight is also minimized by the reduction of RMS current rating, arising from local reactive-power compensation.

A FPGA is employed as controller by reason of its flexibility and its fast and parallel processing characteristics. The operation of the power-supply system is verified by simulation and measurement.

The proposed solution offers significant advantages:

#### 4. PWM-CONTROLLED DRIVING CONCEPT WITH LLCC-FILTER CIRCUIT

---

1. The reactive power of the piezoelectric actuator is compensated locally by placing the inductor  $L_p$  close to the actuator. Hence, inverter, resonant components, transformer and cables of considerable length between output transformer and actuators can be rated mainly with respect to the active power.
2. Due to the PWM method and reactive-power compensation, the output filter shows optimized performance at minimized volume and weight, compared to the classical resonant inverters.
3. The total harmonic distortion (THD) of the piezoelectric actuator voltage is reduced without increasing the switching frequency compared with a LC-PWM inverter.

# Chapter 5

## Investigation on LLCC Three-Level PWM inverter

In this chapter several ways are investigated to improve the PWM three-level inverter. First, the harmonic elimination modulation is studied for the hybrid three-level inverter and employed to reduce the low-order harmonic components without increasing the switching frequency, as well as its effects on power factor and THD of the LLCC filter, in comparison with carrier-based modulation (CBM) and two-level HEM. Secondly, a simple voltage balance controller is introduced to keep the difference voltage of the split DC-link voltages in an acceptable range. Some experiments were conducted to validate the design, and the results are presented here. Finally, a topology using a cascade DC-DC-AC three-level inverter is suggested for future developments.

### 5.1 Three-Level Harmonic Elimination Modulation (HEM)

As discussed in Chapter 4.2.3, the three-level inverter can generate a maximum of five voltage levels determined by the set value  $u_{set}$ . Using harmonic elimination modulation the set value  $u_{set}$  equals  $\hat{U}_{1iv}^*$ , which is defined as the expected amplitude of the fundamental components, normalized to the DC-link voltage  $U_{dc}$ .

In Fig. 5.1 the four possible output voltage waveform are illustrated and classified by the value of  $u_{set}$ . If  $u_{set} \leq 0.52$ , there are only three voltage levels

## 5. INVESTIGATION ON LLCC THREE-LEVEL PWM INVERTER

---

with maximum amplitude of  $U_{dc}/2$  (see Fig. 5.1(a)). Otherwise if  $u_{set} > 0.52$ , five voltage levels are generated in the inverter output voltage  $u_{iv}(t)$  as shown in Fig. 5.1(b,c,d). Therefor  $u_{iv}(t)$  is assumed as quarter-wave symmetrical (see Fig. 5.2 (b)), and can be divided into two separate voltage sources  $u_{1_{iv}}$  and  $u_{2_{iv}}$ , in order to compute the switching angles  $\alpha_{1,1} - \alpha_{1,4}$  and  $\alpha_{2,1} - \alpha_{2,3}$  conveniently.

$$u_{iv} = u_{1_{iv}} + u_{2_{iv}} \implies U_{\nu_{iv}} = U_{1,\nu_{iv}} + U_{2,\nu_{iv}} \quad (5.1)$$

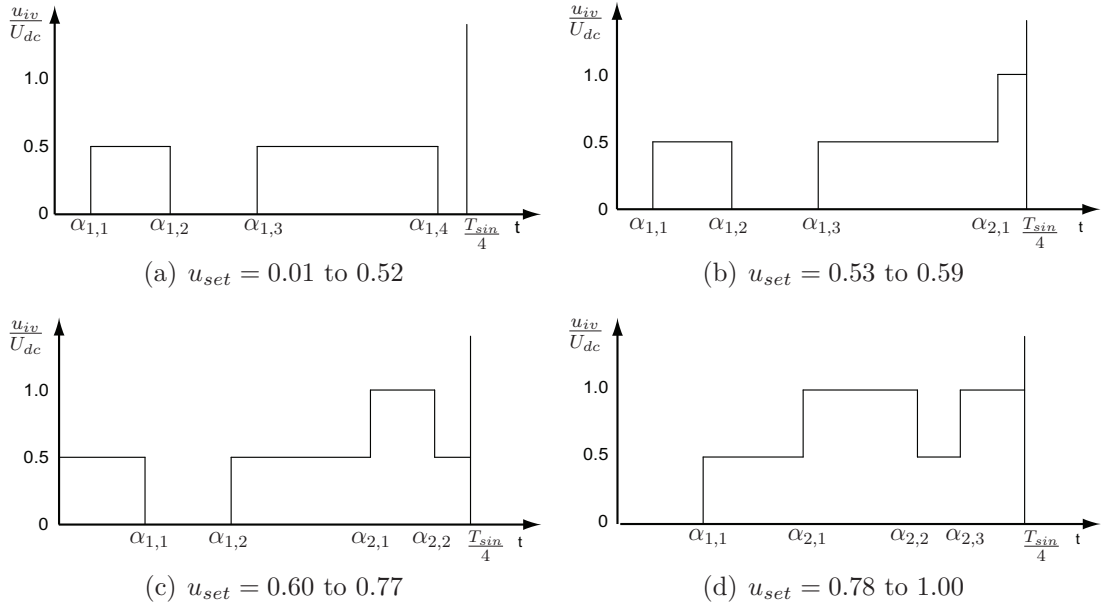


Figure 5.1: Typical output voltage waveforms of three-level inverter at 4 different set value of  $u_{set}$

The switching angles are independent in the first quarter of the waveform, but for the rest they are dependent. For given voltage  $u_{1_{iv}}$  the number of switching angles  $p$  equals 4 maximum, and for  $u_{2_{iv}}$  the number of switching angles  $q$  is 3 maximum. The sum of  $p$  and  $q$  determines the total number of switching angles which need to be calculated using the method described in Appendix A.3.

$$n = p + q \quad (5.2)$$

The selected harmonic elimination can be satisfied by realizing the expected

## 5.1 Three-Level Harmonic Elimination Modulation (HEM)

---

addition of the Fourier coefficient of each voltage in Eq. 5.3:

$$\hat{U}_{1_{iv}}^\star = \hat{U}_{1,1_{iv}} + \hat{U}_{2,1_{iv}} = u_{set} \quad (5.3a)$$

$$\hat{U}_{3_{iv}}^\star = \hat{U}_{1,3_{iv}} + \hat{U}_{2,3_{iv}} = 0 \quad (5.3b)$$

⋮

$$\hat{U}_{n_{iv}}^\star = \hat{U}_{1,n_{iv}} + \hat{U}_{2,n_{iv}} = 0 \quad (5.3c)$$

, here the set value  $u_{set}$  is from 0 to 1.0, and  $n_{iv} = 2g - 1, g = 1, 2, 3, \dots$ , because that  $u_{iv}(t)$  is quarter-wave symmetry.

The symmetrical voltage waveform, which is changing according to  $u_{set}$  (see Fig. 5.1), decides about the Fourier coefficient  $\hat{U}_{\nu_{iv}}$ , calculated using Eq. A.12 or Eq. A.13. The calculation of the general Fourier coefficient solution of a inverter voltage is described in Appendix A.2.

In order to eliminate the 3<sup>rd</sup>, 5<sup>th</sup> and 7<sup>th</sup> harmonics and to ensure a given fundamental content, the four independent switching angles  $\alpha_1, \alpha_2, \alpha_3$  and  $\alpha_4$  are required and chosen from the switching angles  $\alpha_{1,1} - \alpha_{1,4}$  and  $\alpha_{2,1} - \alpha_{2,3}$  determined by  $u_{set}$  (see Fig. 5.1).

This leads to an algorithm with four nonlinear equations which are solved applying Newton's method (see Appendix A.3) as follows [Dau72] [L07].

$$\boldsymbol{\alpha}^{(j+1)} = \boldsymbol{\alpha}^{(j)} - \frac{(\hat{\mathbf{U}}_{iv}(\boldsymbol{\alpha}^{(j)}) - \mathbf{M}_a)}{(\nabla \hat{\mathbf{U}}_{iv}(\boldsymbol{\alpha}^{(j)}))} \quad (5.4)$$

, where  $j$  is the iteration counter of the loop, and

$$\mathbf{M}_a = [\hat{U}_{1_{iv}}^\star \quad 0 \quad 0 \quad 0]^T \quad \text{reference values} \quad (5.5)$$

$$\boldsymbol{\alpha} = [\alpha_1 \quad \alpha_2 \quad \alpha_3 \quad \alpha_4]^T \quad \text{switching points} \quad (5.6)$$

$$\hat{\mathbf{U}}_{iv}(\boldsymbol{\alpha}) = [\hat{U}_{1_{iv}} \quad \hat{U}_{3_{iv}} \quad \hat{U}_{5_{iv}} \quad \hat{U}_{7_{iv}}]^T \quad \text{harmonics} \quad (5.7)$$

$$\nabla \hat{\mathbf{U}}_{iv}(\boldsymbol{\alpha}) = \frac{\partial \hat{\mathbf{U}}_{iv}(\boldsymbol{\alpha})}{\partial \alpha_1, \dots, \partial \alpha_4} \quad \text{Jacobian Matrix} \quad (5.8)$$

The vector  $\hat{\mathbf{U}}_{iv}(\boldsymbol{\alpha})$  is calculated from the Fourier coefficients (see Eq. 5.3) for the three-level inverter:

$$\hat{\mathbf{U}}_{iv}(\boldsymbol{\alpha}) = \begin{pmatrix} \hat{U}_{1_{iv}} \\ \hat{U}_{2_{iv}} \\ \vdots \\ \hat{U}_{n_{iv}} \end{pmatrix} = \begin{pmatrix} \hat{U}_{1,1_{iv}} + \hat{U}_{2,1_{iv}} \\ \hat{U}_{1,2_{iv}} + \hat{U}_{2,2_{iv}} \\ \vdots \\ \hat{U}_{1,n_{iv}} + \hat{U}_{2,n_{iv}} \end{pmatrix} \quad (5.9)$$

## 5. INVESTIGATION ON LLCC THREE-LEVEL PWM INVERTER

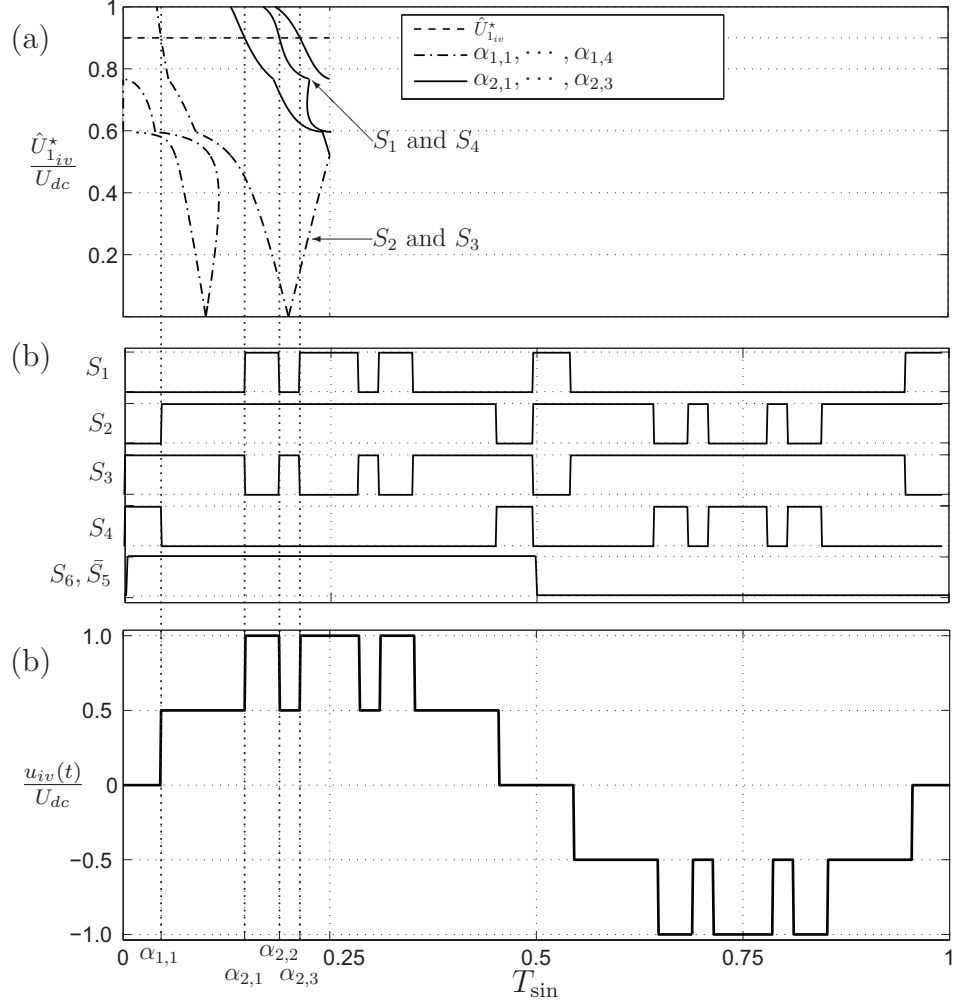


Figure 5.2: Switching angles and output voltage of three-level HEM

(a) Resulting switching angles for  $S_1, S_2, S_3$  and  $S_4$

(b) Driver signals,  $u_{set} = 0.9$

(c) Normalized inverter output voltage,  $u_{set} = 0.9$

From the vector of Fourier coefficients in Eq. 5.9, the partial differential coefficient matrix can be derived as:

$$\nabla \hat{U}_{iv}(\boldsymbol{\alpha}) = \begin{pmatrix} \frac{\partial \hat{U}_{1_{iv}}}{\partial \alpha_{1,1}} & \dots & \frac{\partial \hat{U}_{1_{iv}}}{\partial \alpha_{1,p}} & \frac{\partial \hat{U}_{1_{iv}}}{\partial \alpha_{2,1}} & \dots & \frac{\partial \hat{U}_{1_{iv}}}{\partial \alpha_{2,q}} \\ \frac{\partial \hat{U}_{2_{iv}}}{\partial \alpha_{1,1}} & \dots & \frac{\partial \hat{U}_{2_{iv}}}{\partial \alpha_{1,p}} & \frac{\partial \hat{U}_{2_{iv}}}{\partial \alpha_{2,1}} & \dots & \frac{\partial \hat{U}_{2_{iv}}}{\partial \alpha_{2,q}} \\ \vdots & \ddots & \vdots & \vdots & \ddots & \vdots \\ \frac{\partial \hat{U}_{n_{iv}}}{\partial \alpha_{1,1}} & \dots & \frac{\partial \hat{U}_{n_{iv}}}{\partial \alpha_{1,p}} & \frac{\partial \hat{U}_{n_{iv}}}{\partial \alpha_{2,1}} & \dots & \frac{\partial \hat{U}_{n_{iv}}}{\partial \alpha_{2,q}} \end{pmatrix} \quad (5.10)$$

## 5.1 Three-Level Harmonic Elimination Modulation (HEM)

---

The iterative algorithm is to calculate, until the critical difference  $\Delta\alpha$  fulfills the following inequation: .

$$\Delta\alpha = \alpha^{(j+1)} - \alpha^{(j)} < \epsilon, \text{ with the expected error } \epsilon = [\epsilon_1 \ \epsilon_2 \ \cdots \ \epsilon_n]^T. \quad (5.11)$$

The switching angles resulting from this harmonic elimination technique are shown in Fig. 5.2(a) depending on the fundamental content  $\hat{U}_{1iv}^*$ . Switching angles referring to transistors  $S_2$  and  $S_3$  are denoted as  $\alpha_{1,i}$ , those referring to  $S_1$  and  $S_4$  are denoted as  $\alpha_{2,i}$ . Note that transistors  $S_5$  and  $S_6$  are used only to change the polarity of the output voltage. E.g., for the positive halfwave with positive current,  $S_6$  is turned on and pulses are generated using  $S_1 - S_4$ , while  $S_5$  is kept completely turned off.

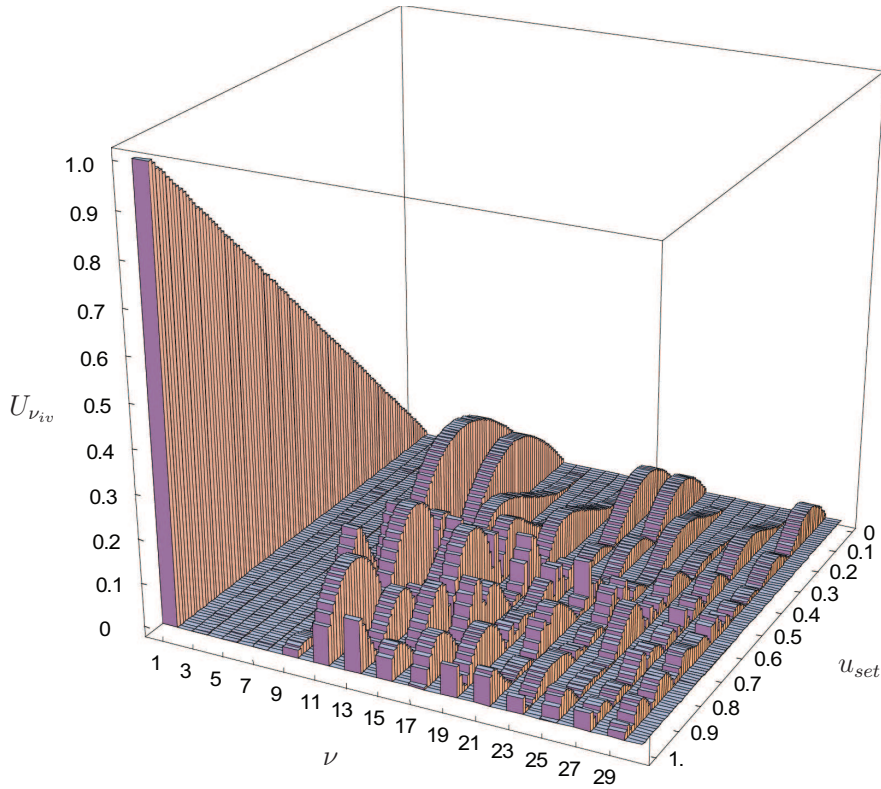


Figure 5.3: Spectrum of output voltage using three-level HEM

The spectrum of the inverter output voltage is shown in Fig. 5.3. As expected, the 3<sup>rd</sup>, 5<sup>th</sup>, 7<sup>th</sup> harmonic components do not occur, though the switching frequency is the same as with the three-level carrier-based PWM (see Chapter 4.2.3.1). But

## 5. INVESTIGATION ON LLCC THREE-LEVEL PWM INVERTER

the harmonic components of 11<sup>th</sup>, 13<sup>rd</sup>, 15<sup>th</sup> and 17<sup>th</sup> order of HEM are larger than those of CBM.

### 5.2 LLCC Three-Level HEM Inverter

According to the design process described in section 4.1, the damping of the 3<sup>rd</sup> harmonic is chosen at  $-5$  dB; hence, the design parameter  $\alpha_{LLCC} \approx 3$  results [LLFB08]. The resulting filter parameters are presented in Tab. 5.1, which are identical with parameters for LLCC two-level HEM inverter in Tab.4.1

Parameter		Value
Mechanical resonance frequency	$f_{mr1}$	33000 Hz
Piezoelectric equiv. capacitor	$C_p$	176 nF
Series capacitor	$C_s$	528 nF
Parallel inductor	$L_p$	132 $\mu$ H
Series inductor	$L_s$	44 $\mu$ H

Table 5.1: Components design of LLCC filter fed by three-level HEM inverter

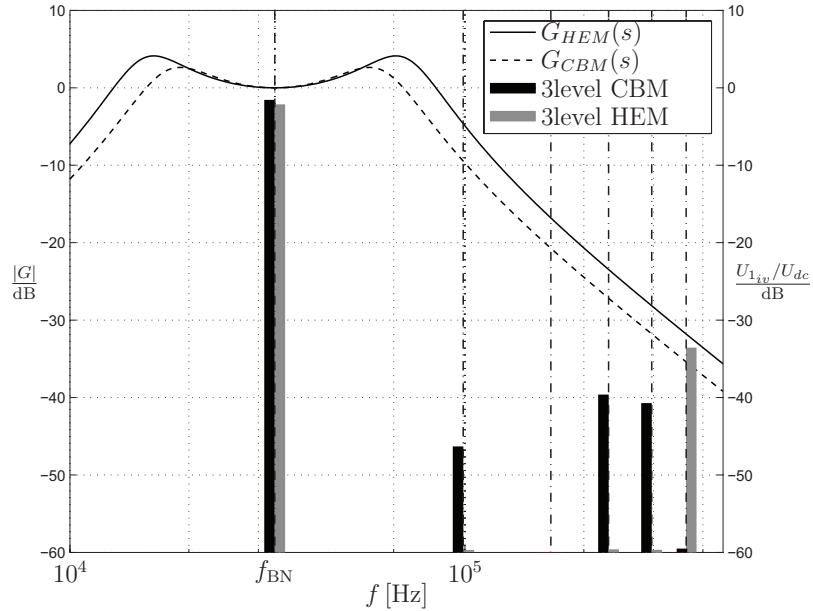


Figure 5.4: Comparison of frequency spectrum and transfer function of three-level inverter

## 5.2 LLCC Three-Level HEM Inverter

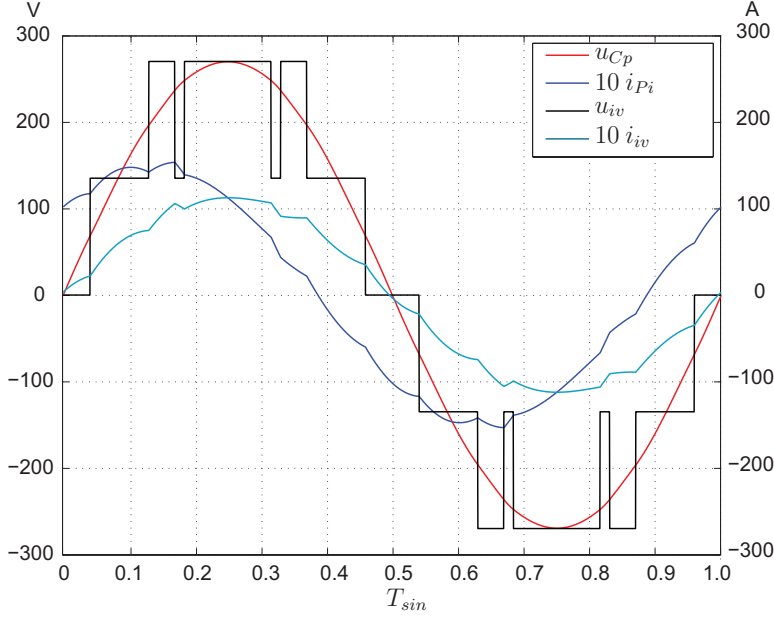


Figure 5.5: Currents and voltages of filter input and output,  $u_{set} = 1.0$

Fig. 5.4 presents the harmonics of  $u_{iv}(t)$  as they result from the harmonic elimination modulation (HEM) compared with a conventional carrier-based modulation (CBM). As expected, the harmonics of orders 3<sup>rd</sup>, 5<sup>th</sup> and 7<sup>th</sup> are adjusted to zero using HEM compared with using CBM. For higher-order harmonics, however, the CBM may generate lower amplitudes than HEM. The harmonics of the actuator voltage  $u_{Cp}(t)$  are determined by multiplication of the respective inverter harmonic amplitudes with the LLCC filter transfer function, which is shown in Fig. 5.4. Because the high-order harmonics are strongly attenuated by the filter, the THD of piezoelectric actuator voltage is therefore much lower using HEM.

The simulated results of currents and voltages of filter input and output are shown in Fig. 5.5. As the gain of the transfer function at the operating point approximates 0 dB, the amplitude of the piezoelectric actuator voltage equals the amplitude of the fundamental component of inverter output voltage. The ripple of the inverter current  $i_{iv}(t)$  is smaller than it results from the LLCC three-level CBM inverter using  $f_p = 8 f_{sin}$  and similar in case of  $f_p = 16 f_{sin}$  shown in Fig. 4.16(b), even though the pulse frequency  $f_p$  of three-level HEM is only set as  $8 f_{sin}$ .

## 5. INVESTIGATION ON LLCC THREE-LEVEL PWM INVERTER

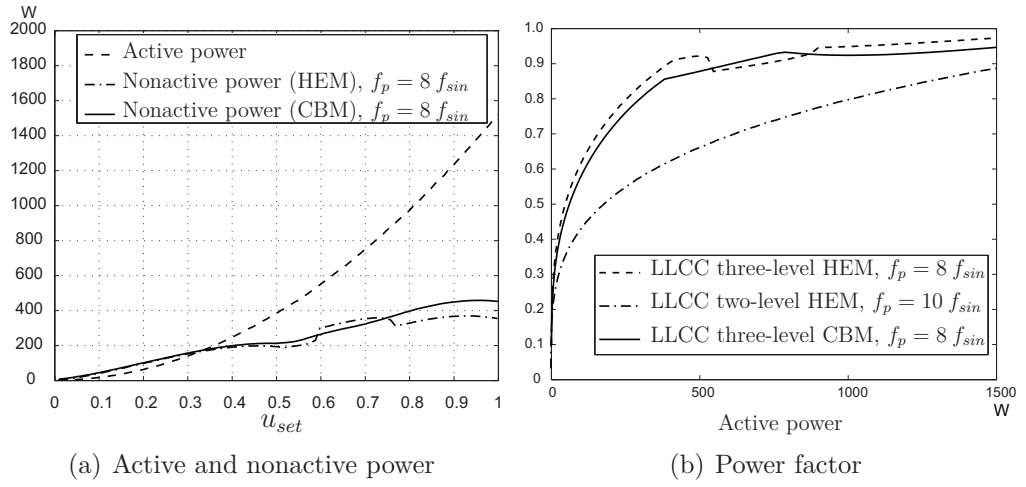


Figure 5.6: Comparison of selected power supplies

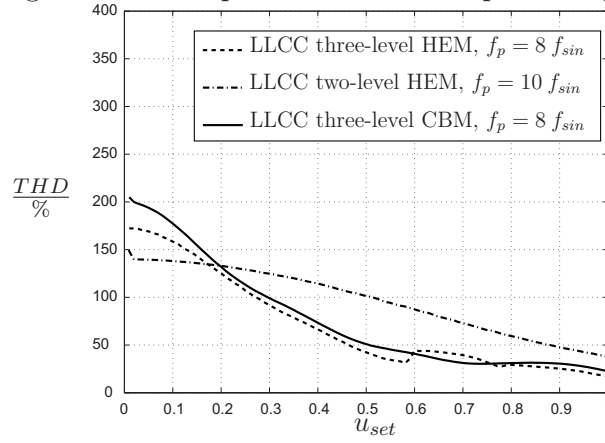


Figure 5.7: THD curve of selected inverter output voltage  $u_{iv}(t)$  up to 21th harmonics

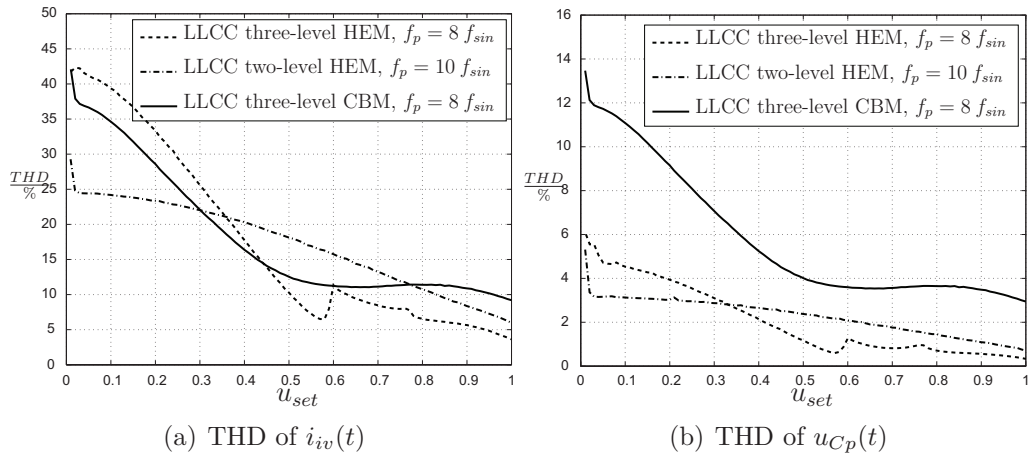


Figure 5.8: Comparison of THD after filter circuits

---

### 5.3 Strategy for Voltage-Balancing Control

The delivered nonactive powers are compared between HEM and CBM, and illustrated in 5.6(a). The difference of reactive power are not dominating, HEM produces more reactive, if  $u_{set}$  is between 0.59 to 0.76. The waveform of  $u_{iv}(t)$  in Fig. 5.1(c) can explain the reason. We see the  $u_{iv}(t)$  begins with  $U_{dc}/2$  instead of 0, while the current  $i_{is}$  rises still only from 0. This effect generates more reactive power by the inverter.

Power factor is one criterion for evaluating the performance of power supplies. In Fig. 5.6(b) the power factors of selected power supplies are presented for comparison. It can be seen that the power factor of the LLCC three-level HEM inverter is improved by 5 % compared to the LLCC three-level CBM inverter.

The THD characteristic curves of the inverter output voltage  $u_{iv}(t)$  are analysed up to 21th harmonics and presented in Fig. 5.7, where the pulse number equals 8 for both three-level inverter and 10 for two-level HEM inverter in one period. Thanks to the advantage of five voltage levels of the three-level inverter, both three-level PWM methods produce less THD than the two-level HEM inverter when  $u_{set} > 0.2$ .

As mentioned in Chapter 4.3, THD of  $u_{iv}(t)$  depends only on the modulation method of the inverter, while THD of  $i_{iv}(t)$  and  $u_{Cp}(t)$  are determined by inverter as well as filter characteristic compared in Fig. 5.4. Therefore the THD of  $i_{iv}(t)$  and  $u_{Cp}(t)$  by the different modulations presented in Fig. 5.2 are different from the THD of  $u_{iv}(t)$  in Fig. 5.7. By using HEM LLCC three-level inverter, smaller THD of  $i_{iv}(t)$  and  $u_{Cp}(t)$  than using CBM is attained; The improvements are apparent from the diagram of THD of  $u_{Cp}(t)$  (see Fig. 5.2(b)).

### 5.3 Strategy for Voltage-Balancing Control

Since the energy buffer consists of a series-capacitive voltage divider shown in Fig. 5.9, the difference voltage  $\Delta u_{dc}$  between  $u_{dc1}$  and  $u_{dc2}$  can not keep zero automatically, due to the reasons such as different capacitance or unbalancing DC charging current caused by PWM.

It is essential that the voltage across the DC-link capacitors must be balanced, otherwise the capacitors will tend to overcharge or completely discharge, and the output voltage would get a DC component and even harmonic components could

## 5. INVESTIGATION ON LLCC THREE-LEVEL PWM INVERTER

be introduced with the consequence of increased THD.

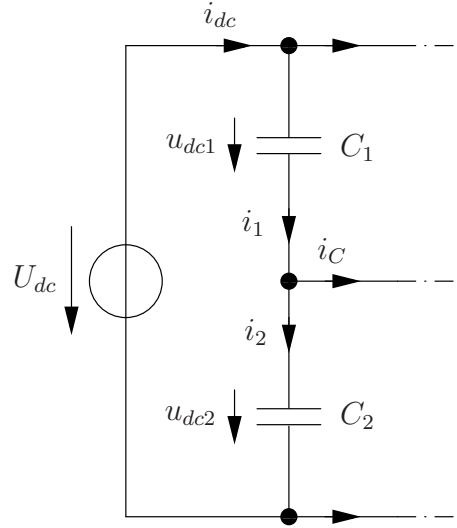


Figure 5.9: Capacitive voltage divider

In order to avoid harmful unbalanced voltage, a controller has to take care of DC balancing so that  $\Delta u_{dc}$  can be kept in a acceptable range.

$$U_{dc} = u_{dc1}(t) + u_{dc2}(t) \quad (5.12)$$

$$\Delta u_{dc} = u_{dc2}(t) - u_{dc1}(t) \quad (5.13)$$

Three different cases are considered depending on the voltage deviation:

- **Balanced case:**  $|\Delta u_{dc}| = 0$  to 5 V  
Modulation used is the same as explained in Chapter 5.1.
- **Unbalanced case:**  $|\Delta u_{dc}| = 5$  to 20 V  
In this case  $\Delta u$  has to be balanced actively by a controller; a detailed explanation follows in this section.
- **Failure case:**  $|\Delta u_{dc}| > 20$  V  
Protection shutdown.

The difference voltage  $\Delta u_{dc}$  can essentially be controlled by  $i_C(t)$  (see Fig. 5.9) according to Eq. 5.14b. The objective of the voltage balance control is to keep



## 5. INVESTIGATION ON LLCC THREE-LEVEL PWM INVERTER

four switching angles  $\beta_1$  to  $\beta_4$  in addition to  $\alpha_i$  resulting in a total set of eight independent variables. As a result of these new pulse patterns, the voltage  $u_{iv}(t)$  is not free of a DC bias, Nevertheless the DC content of  $u_{Cp}(t)$  is still nearly zero, due to the band-pass behavior of LLCC filter, which enables to suppress the DC content sufficiently.

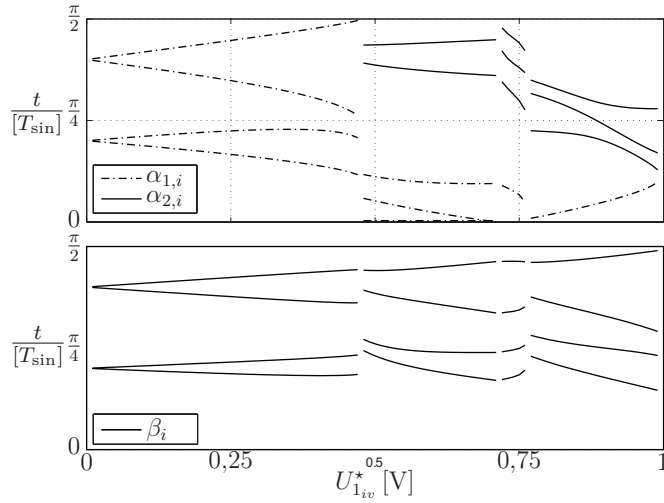


Figure 5.11: Switching angles in unbalanced state

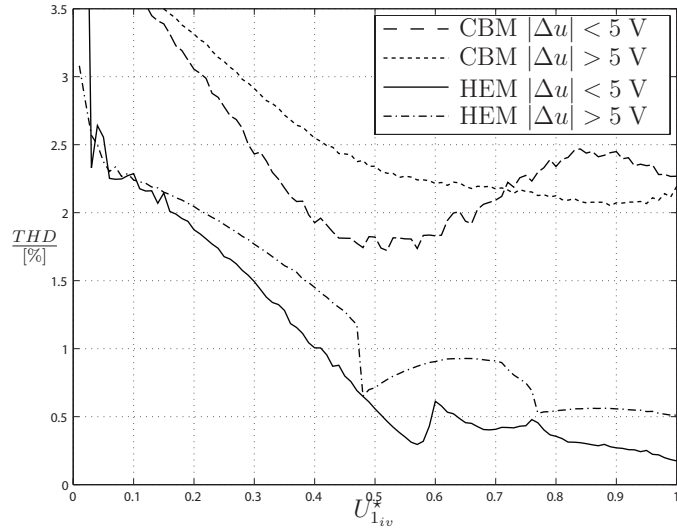


Figure 5.12: Total harmonic distortion (THD) of voltage  $u_{Cp}(t)$

The set of eight nonlinear equations is again solved applying Newton's method. The results are shown in Fig. 5.11.

## 5.4 Cascaded DC-DC-AC Three-Level Topology

A simulation was carried out to evaluate the performance of these modulation methods. For both modulation types (HEM and CBM) the THD of  $u_{Cp}(t)$  were calculated and plotted in Fig. 5.12. It is obvious that the THD values of the HEM is always lower compared to the CBM. This is valid for the whole operating region. On a closer look to Fig. 5.12 it is visible that the lowest frequency harmonics in case of CBM are not strongly attenuated. These harmonics are the major contributor for the THD. However, in case of HEM the 2<sup>nd</sup> to 8<sup>th</sup> harmonics are zero, and hence the lower THD results.

Note that this simple voltage balance controller is limited to cooperate with LLCC filter, because its precondition is that the inverter output voltage  $u_{iv}(t)$  and current  $i_{iv}(t)$  must be in phase or with only small phase shift.

## 5.4 Cascaded DC-DC-AC Three-Level Topology

Due to the limitation of the voltage-balance controller discussed in Chapter 5.3, and considering that the best performance of the three-level inverter occurs always when  $u_{set} = 1$ , a cascade DC-DC-AC PWM inverter with LLCC filter is suggested to be included future investigations.

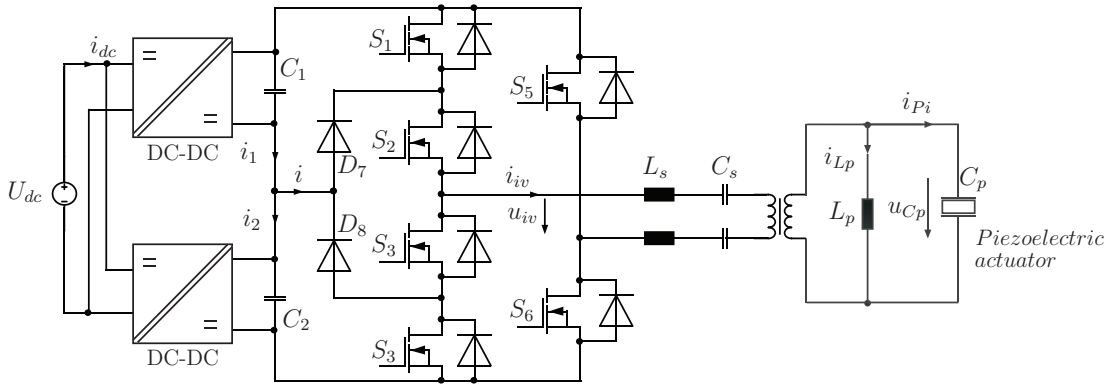


Figure 5.13: Cascaded DC-DC-AC PWM inverter with LLCC filter

In Fig. 5.13 a topology consisting of two DC-DC converters and one three-level inverter is illustrated. These DC-DC converters are used to couple the input side capacitors  $C_1$  and  $C_2$  with the DC-link. Instead of the voltage-balance controller,

## 5. INVESTIGATION ON LLCC THREE-LEVEL PWM INVERTER

the voltage amplitudes of  $C_1$  and  $C_2$  are regulated to the same value by the DC-DC converters according to the set value  $u_{set}$ . Then the three-level inverter is modulated using only one pulse pattern, for example using HEM with  $\hat{U}_{1_{iv}}^\star = 1$ .

But the penalty of adding a series-connected DC-DC converter is increased total losses.

### 5.5 Measurement Results of LLCC Three-Level Inverter with Equivalent Load

Resulting experimental waveforms using an equivalent load are shown in Fig. 5.14, showing that the voltage across the equivalent piezo capacitor  $u_{C_p}(t)$  are nicely sinusoidal as in the simulation, only the phase of  $i_{iv}(t)$  is slightly ahead of the phase of  $u_{iv}(t)$ , the LLCC circuit including equivalent load presents a capacitive behavior at this operating point.

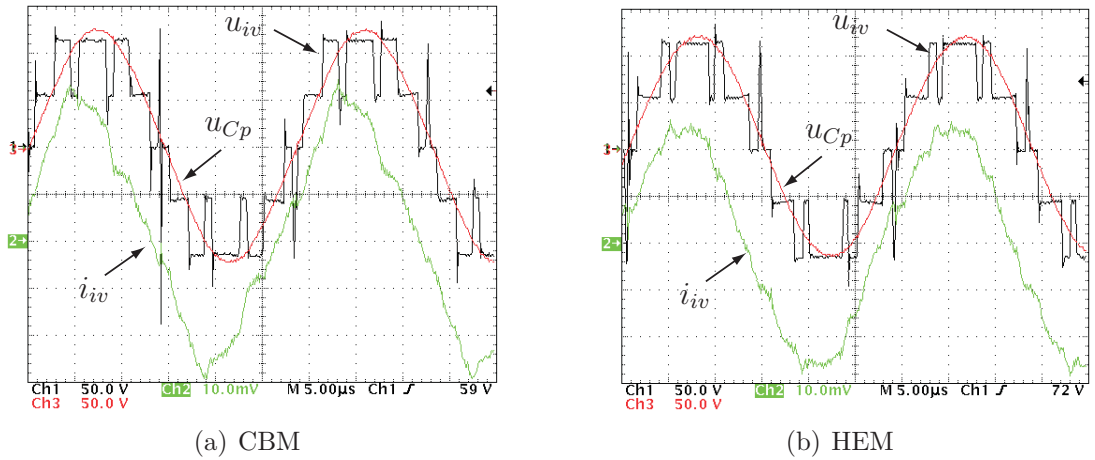


Figure 5.14: measurement of prototype

Because the freewheeling current  $i_{iv}(t)$  flows via the internal diodes of  $S_1 - S_4$  during the current commutation, voltage spikes are generated in  $u_{iv}(t)$ , when the current  $i_{iv}(t)$  changes to contra direction at the end of every half period. The amplitude of these spike equals the amplitude of DC-link voltage.

The measured spectrum of the inverter output voltage is shown in Fig. 5.15(a). As expected, the harmonics of orders 3, 5 and 7 are close to zero with the harmon-

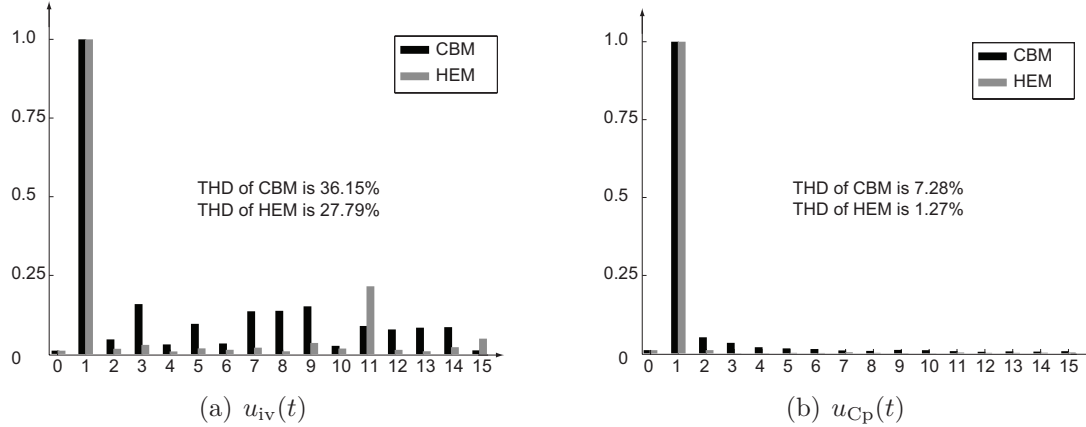


Figure 5.15: Frequency spectrum

ics elimination modulation, contrary to conventional carrier-based PWM. High-order harmonics, however, may be larger with HEM compared to CBM (e.g. orders 11 and 15). These harmonics have only minor effect on the THD, because they are sufficiently suppressed by the LLCC filter (Fig. 5.15(b)). As a result, the THD of  $u_{cp}(t)$  is smaller with HEM (Fig. 5.15(b))

In the inverter output voltage  $u_{iv}(t)$ , the 3<sup>rd</sup>, 5<sup>th</sup> and 7<sup>th</sup> harmonic components are reduced by using selective harmonic elimination modulation compared with the carrier-based PWM. From the voltage frequency spectrum of piezoelectric actuator (Fig. 5.15(b)) we see that the harmonic components are well suppressed with increasing frequency due to the characteristic of the LLCC-filter circuit. So even though the components of the harmonics after 9<sup>th</sup> order in case of HEM are larger than those in case of CBM, the THD of the piezoelectric actuator voltage is smaller at HEM.

## 5.6 Summary

A three-level inverter using HEM for driving the high-power piezoelectric actuator has been investigated, that comes out with low weight and volume together with minimized THD of the actuator voltages. In particular this has been achieved by combining several techniques as follows:

- Three-level harmonic elimination modulation

## 5. INVESTIGATION ON LLCC THREE-LEVEL PWM INVERTER

- Elimination of low-order harmonics from the PWM
- LLCC filter with matching characteristics
- Simple voltage balance controller

# Chapter 6

## Control Design of Power Supply

In this chapter a model-based control design is investigated considering the inner control loops. In order to analyze the dynamic behavior, an averaging model of the LLCC PWM inverter is set up. For controlling thrust, torque and speed by the mechanical oscillation of the tangential-mode and normal-mode piezoelectric actuators of the MM-USM, the supplying voltage amplitude and frequency are regulated, supported by the phase angle control between both modes.

### 6.1 Control Objective

The power-supply control serves as inner control loop of the whole piezoelectric brake actuator control system. Hence, three control parameters are available to control the MM-USM using power supplies, which are amplitude, fundamental frequency of supplying voltage, and phase shift between tangential-mode and normal-mode piezoelectric actuators [Pib07b] [WLFB07].

Due to the variation of mechanical load (see Fig. 2.8 and Fig. 2.10), the parameters of the equivalent electrical circuit change, indicated by load  $R_m$  resulting in different frequency characteristics, as in addition the piezoelectric capacitance  $C_p$  varies influenced mainly by temperature variation.

Those corresponding influences act on the current and voltage of the piezoelectric actuator, and exhibits on the admittance of piezoelectric actuator  $Y_{Pi}(j\omega)$ ,

## 6. CONTROL DESIGN OF POWER SUPPLY

---

whose magnitude and phase are calculated as:

$$|Y_{Pi}(j\omega)| = \left| \frac{i_{Pi}}{u_{Cp}} \right| \quad (6.1)$$

$$\phi_{Y_{Pi}(j\omega)} = \phi_{i_{Pi}} - \phi_{u_{Cp}} \quad (6.2)$$

## 6.2 Modeling of MM-USM Driven by LLCC-PWM Inverter

### 6.2.1 Generalized Averaging Method

In order to reduce the simulation time and facilitate the control design, a model with idealized switching behavior of the power circuitry is assumed. The generalized averaging method [SNLV91] is employed to approximate the original state variables by a Fourier series representation of fundamental order, since distortion of harmonic waveforms is negligible

By a 1st-order Fourier series representation, every quantity  $x(t)$  can be expressed as:

$$x(t) = x_s(t) \sin(\omega_{Op}t) + x_c(t) \cos(\omega_{Op}t) \quad (6.3)$$

with slowly time-varying Fourier coefficients  $x_s(t), x_c(t)$ , where  $\omega_{Op}$  is the operating frequency.

In publications [Mas98] and [Sch04a] this generalized averaging method was employed to build the averaging model of TW-USM driven by the LC and LLCC-resonant inverter. According to the principle of piezoelectric energy conversion, the averaging model is divided into an electrical and a mechanical subsystem. Each subsystem can be analyzed using methods for linear systems.

State-space equations are employed for representing the averaging models of the tangential-mode and the normal-mode power supplies and the piezoelectric actuator. Since the Fourier coefficients vary much slower in time than the original quantities, this model is more suitable for means of control design.

### 6.2.2 Averaging Model of Electrical Subsystem

As described in former chapters, a LLCC filter is employed between PWM inverter and piezoelectric actuator. Fig. 6.1 presents the driving circuit using a LLCC

## 6.2 Modeling of MM-USM Driven by LLCC-PWM Inverter

filter and the equivalent mechanical load is represented as a current source. The electrical subsystem consists of a series inductor, a series capacitor and a parallel inductor, while the capacitance of the piezoelectric actuator is assigned to the piezoelectric mechanical subsystem.

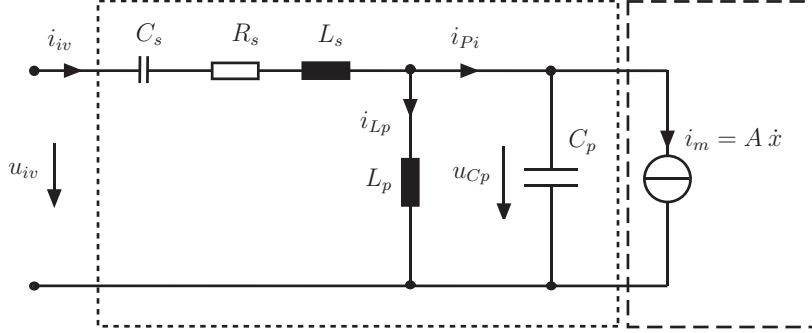


Figure 6.1: LLCC filter with equivalent mechanical load

Due to the feedback of the piezoelectric mechanical subsystem, its influence on the feeding filter and the inverter is given by the charges  $\int i_m dt$ . Considering these charges, a voltage  $u_{pi} = u_{Cp} + u_m$  is selected as state variable instead of  $u_{Cp}$ , where  $u_m = \int \frac{i_m}{C_p} dt$  is the feedback voltage of the piezoelectric actuator [MG97].

Note that the parameters presented in Fig. 6.1 are specified for both tangential mode and normal mode. The state variables of the electrical subsystem  $\mathbf{x}_{el}$  are  $[i_{Ls}, u_{Cs}, i_{Lp}, u_{pi}]$ , input variables are  $[u_{iv}, u_m]$ , and output variable is the voltage  $u_{pi}$  fed into mechanical subsystem of the piezoelectric actuator. The electrical subsystem can be described by state-space equation as follows:

$$\begin{bmatrix} \dot{i}_{Ls} \\ \dot{u}_{Cs} \\ \dot{i}_{Lp} \\ \dot{u}_{pi} \end{bmatrix} = \begin{bmatrix} -\frac{R_s}{L_s} & -\frac{1}{L_s} & 0 & -\frac{1}{L_s} \\ \frac{1}{C_s} & 0 & 0 & 0 \\ 0 & 0 & 0 & \frac{1}{L_p} \\ \frac{1}{C_p} & 0 & -\frac{1}{C_p} & -\frac{1}{C_p R_p} \end{bmatrix} \begin{bmatrix} i_{Ls} \\ u_{Cs} \\ i_{Lp} \\ u_{pi} \end{bmatrix} + \begin{bmatrix} \frac{1}{L_s} & \frac{1}{L_s} \\ 0 & 0 \\ 0 & -\frac{1}{L_p} \\ 0 & \frac{1}{C_p R_p} \end{bmatrix} \begin{bmatrix} u_{iv} \\ u_m \end{bmatrix} \quad (6.4)$$

The state-space equations of the electrical subsystem can be represented by Fourier coefficients using Eq. 6.4:

$$\begin{aligned} \begin{bmatrix} \dot{\mathbf{x}}_{el} \\ \mathbf{y}_{el} \end{bmatrix} &= \begin{bmatrix} \mathbf{A}_{el,Og} & \mathbf{\Omega}_{el,Op} \\ -\mathbf{\Omega}_{el,Op} & \mathbf{A}_{el,Og} \end{bmatrix} \begin{bmatrix} \mathbf{x}_{el} \\ \mathbf{y}_{el} \end{bmatrix} + \begin{bmatrix} \mathbf{B}_{el,Og} & 0 \\ 0 & \mathbf{B}_{el,Og} \end{bmatrix} \begin{bmatrix} \mathbf{u}_{el} \\ \mathbf{y}_{el} \end{bmatrix} \\ \begin{bmatrix} \mathbf{y}_{el} \end{bmatrix} &= \begin{bmatrix} \mathbf{C}_{el,Og} & 0 \\ 0 & \mathbf{C}_{el,Og} \end{bmatrix} \begin{bmatrix} \mathbf{x}_{el} \\ \mathbf{y}_{el} \end{bmatrix}, \end{aligned} \quad (6.5)$$

## 6. CONTROL DESIGN OF POWER SUPPLY

---

with

$$\mathbf{A}_{\text{el, Og}} = \begin{bmatrix} -\frac{R_s}{L_s} & -\frac{1}{L_s} & 0 & -\frac{1}{L_s} \\ \frac{1}{C_s} & 0 & 0 & 0 \\ 0 & 0 & 0 & \frac{1}{L_p} \\ \frac{1}{C_p} & 0 & -\frac{1}{C_p} & -\frac{1}{C_p R_p} \end{bmatrix}, \mathbf{B}_{\text{el, Og}} = \begin{bmatrix} \frac{1}{L_s} & \frac{1}{L_s} \\ 0 & 0 \\ 0 & -\frac{1}{L_p} \\ 0 & \frac{1}{C_p R_p} \end{bmatrix}$$

$$\mathbf{\Omega}_{\text{el, Op}} = \begin{bmatrix} \omega_{Op} & 0 & 0 & 0 \\ 0 & \omega_{Op} & 0 & 0 \\ 0 & 0 & \omega_{Op} & 0 \\ 0 & 0 & 0 & \omega_{Op} \end{bmatrix}, \mathbf{C}_{\text{el, Og}} = [0 \ 0 \ 0 \ 1]$$

$$\mathbf{x}_{\text{el}} = [i_{Ls,s}, u_{Cs,s}, i_{Lp,s}, u_{pi,s}, i_{Ls,c}, u_{Cs,c}, i_{Lp,c}, u_{pi,c}]^T$$

$$\mathbf{u}_{\text{el}} = [u_{iv,s}, u_{m,s}, u_{iv,c}, u_{m,c}]^T$$

$$\mathbf{y}_{\text{el}} = [u_{pi,s}, u_{pi,c}]^T.$$

For the averaging mode of the tangential and the normal electrical subsystem the same state-space equations are used, but different parameters values are assigned.

### 6.2.3 Averaging Model of Piezoelectric Mechanical Subsystem

Different from the electrical subsystem, the piezoelectric mechanical subsystem use different state-space equation for the tangential and the normal mode, due to the shearing influence of the elastic layer on the tangential mode. The state variables, input variables and output variable of piezoelectric and mechanical subsystem are listed in Tab. 6.1, where  $u_{CpT}$  and  $u_{CpN}$  are piezoelectric capacitance voltages,  $x_{tT}$  and  $x_{tN}$  are displacements of piezoelectric actuator:  $x_{iT}$  is the displacement of the elastic layer of tangential mode,  $u_{piT}$  and  $u_{piN}$  are output voltages from the electrical subsystem,  $f_{mT}$  and  $f_{mN}$  are mechanical load press.

	State variables	Input	Output
Tangential mode	$u_{CpT}, x_{tT}, \dot{x}_{tT}, x_{iT}, \dot{x}_{iT}$	$u_{piT}, f_{mT}$	$x_{tT}, x_{iT}$
Normal mode	$u_{CpN}, x_{tN}, \dot{x}_{tN}$	$u_{piN}, f_{mN}$	$x_{tN}$

Table 6.1: Variables of piezoelectric mechanical subsystem

## 6.2 Modeling of MM-USM Driven by LLCC-PWM Inverter

---

Deriving from 2.3 the differential equations of the tangential mode, the displacement of the piezoelectric mechanical subsystem including the elastic layer is calculated as:

$$\begin{cases} \ddot{x}_{tT} = \frac{1}{m_T}(A_T u_{CpT} - c_T x_{tT} - d_T \dot{x}_{tT}) - kt(x_{tT} - x_{iT}) \\ \ddot{x}_{iT} = \frac{kt}{mi_T}(x_{tT} - x_{iT} - f_{mT}), \end{cases} \quad (6.6)$$

where  $A_T$  is the force factor,  $c_T$  is the stiffness,  $d_T$  corresponds to the damping,  $m_T$  is the mass of the tangential mode and  $mi_T$  is the mass of the elastic layer.

Using the following equation

$$\begin{aligned} u_{CpT} &= u_{piT} - u_{mT} \\ &= u_{piT} - \frac{A_T}{C_{pT}}x_{tT}, \end{aligned} \quad (6.7)$$

the differential equation 6.6 can be represented as:

$$\begin{cases} \ddot{x}_{tT} = \frac{1}{m_T}(A_T u_{piT} - (c_T + \frac{A_T^2}{C_{pT}})x_{tT} - d_T \dot{x}_{tT}) - kt(x_{tT} - x_{iT}) \\ \ddot{x}_{iT} = \frac{kt}{mi_T}(x_{tT} - x_{iT} - f_{mT}), \end{cases} \quad (6.8)$$

From Eq. 6.8 the state-space equation can be described as:

$$\begin{aligned} \begin{bmatrix} \dot{x}_{tT} \\ \ddot{x}_{tT} \\ \dot{x}_{iT} \\ \ddot{x}_{iT} \end{bmatrix} &= \begin{bmatrix} 0 & 1 & 0 & 0 \\ -\frac{c'_T+kt}{m_T} & -\frac{d_T}{m_T} & \frac{kt}{m_T} & 0 \\ 0 & 0 & 0 & 1 \\ \frac{kt}{mi_T} & 0 & -\frac{kt}{mi_T} & 0 \end{bmatrix} \begin{bmatrix} x_{tT} \\ \dot{x}_{tT} \\ x_{iT} \\ \dot{x}_{iT} \end{bmatrix} + \begin{bmatrix} 0 & 0 \\ \frac{A_T}{m_T} & 0 \\ 0 & 0 \\ 0 & \frac{1}{mi_T} \end{bmatrix} \begin{bmatrix} u_{piT} \\ f_{mT} \end{bmatrix} \\ \begin{bmatrix} x_{tT} \\ x_{iT} \end{bmatrix} &= \begin{bmatrix} 1 & 0 & 0 & 0 \\ 0 & 0 & 1 & 0 \end{bmatrix} \begin{bmatrix} x_{tT} \\ \dot{x}_{tT} \\ x_{iT} \\ \dot{x}_{iT} \end{bmatrix}, \end{aligned} \quad (6.9)$$

where  $c'_T = c_T + \frac{A_T^2}{C_{pT}}$ .

Using the averaging modeling method the tangential-mode mechanical subsystem is represented in state-space mode by the 1st-order Fourier series representation:

$$\begin{aligned} \begin{bmatrix} \dot{\mathbf{x}}_{mT} \\ \mathbf{y}_{mT} \end{bmatrix} &= \begin{bmatrix} \mathbf{A}_{mT, Og} & \Omega_{mT, Op} \\ -\Omega_{mT, Op} & \mathbf{A}_{mT, Og} \end{bmatrix} \begin{bmatrix} \mathbf{x}_{mT} \\ \mathbf{y}_{mT} \end{bmatrix} + \begin{bmatrix} \mathbf{B}_{mT, Og} & 0 \\ 0 & \mathbf{B}_{mT, Og} \end{bmatrix} \begin{bmatrix} \mathbf{u}_{mT} \\ \mathbf{y}_{mT} \end{bmatrix} \\ \mathbf{y}_{mT} &= \begin{bmatrix} \mathbf{C}_{mT, Og} & 0 \\ 0 & \mathbf{C}_{mT, Og} \end{bmatrix} \begin{bmatrix} \mathbf{x}_{mT} \\ \mathbf{y}_{mT} \end{bmatrix}, \end{aligned} \quad (6.10)$$

## 6. CONTROL DESIGN OF POWER SUPPLY

---

with

$$\mathbf{A}_{\mathbf{mT},\mathbf{Og}} = \begin{bmatrix} 0 & 1 & 0 & 0 \\ -\frac{c'_T+kt}{m_T} & -\frac{d_T}{m_T} & \frac{kt}{m_T} & 0 \\ 0 & 0 & 0 & 1 \\ \frac{kt}{mi_T} & 0 & -\frac{kt}{mi_T} & 0 \end{bmatrix}, \mathbf{B}_{\mathbf{mT},\mathbf{Og}} = \begin{bmatrix} 0 & 0 \\ \frac{A_T}{m_T} & 0 \\ 0 & 0 \\ 0 & \frac{1}{mi_T} \end{bmatrix}$$

$$\mathbf{\Omega}_{\mathbf{mT},\mathbf{Op}} = \begin{bmatrix} \omega_{Op} & 0 & 0 & 0 \\ 0 & \omega_{Op} & 0 & 0 \\ 0 & 0 & \omega_{Op} & 0 \\ 0 & 0 & 0 & \omega_{Op} \end{bmatrix}, \mathbf{C}_{\mathbf{mT},\mathbf{Og}} = \begin{bmatrix} 1 & 0 & 0 & 0 \\ 0 & 0 & 1 & 0 \end{bmatrix}$$

$$\mathbf{x}_{\mathbf{mT}} = [x_{tT,s}, \dot{x}_{tT,s}, x_{iT,s}, \dot{x}_{iT,s}, x_{tT,c}, \dot{x}_{tT,c}, x_{iT,c}, \dot{x}_{iT,c}]^T$$

$$\mathbf{u}_{\mathbf{mT}} = [u_{piT,s}, f_{mT,s}, u_{piT,c}, f_{mT,c}]^T$$

$$\mathbf{y}_{\mathbf{mT}} = [x_{tT,s}, x_{iT,s}, x_{tT,c}, x_{iT,c}]^T.$$

The influence of the elastic layer on the normal-mode piezoelectric actuator is neglected, due to the very small displacement difference in normal direction. Hence, the differential equations of the normal-mode piezoelectric mechanical subsystem are represented by

$$\ddot{x}_N = \frac{1}{m_N}(A_N u_{piN} - (c_N + \frac{A_N^2}{C_{pN}}) x_N - d_N \dot{x}_N - f_{mN}), \quad (6.11)$$

where  $A_N$ ,  $c_N$ ,  $d_N$  and  $m_N$  are the normal-mode force factor, stiffness, damping and mass, respectively. From Eq. 6.11 the state-space equations can be described by:

$$\begin{bmatrix} \dot{x}_N \\ \ddot{x}_N \end{bmatrix} = \begin{bmatrix} 0 & 1 \\ -\frac{c'_N}{m_N} & -\frac{d_N}{m_N} \end{bmatrix} \begin{bmatrix} x_N \\ \dot{x}_N \end{bmatrix} + \begin{bmatrix} 0 & 0 \\ \frac{A_N}{m_N} & \frac{1}{m_N} \end{bmatrix} \begin{bmatrix} u_{piN} \\ f_{mN} \end{bmatrix} \quad (6.12)$$

$$\begin{bmatrix} x_{tN} \end{bmatrix} = \begin{bmatrix} 1 & 0 \end{bmatrix} \begin{bmatrix} x_N \\ \dot{x}_N \end{bmatrix}$$

where  $c'_N = c_N + \frac{A_N^2}{C_{pN}}$ .

The same averaging technique used for the electrical subsystem is applied to the tangential-mode mechanical subsystem, which can be represented as a state-space model using 1st-order Fourier series representation:

$$\begin{bmatrix} \dot{\mathbf{x}}_{\mathbf{mN}} \\ \mathbf{y}_{\mathbf{mN}} \end{bmatrix} = \begin{bmatrix} \mathbf{A}_{\mathbf{mN},\mathbf{Og}} & \mathbf{\Omega}_{\mathbf{mN},\mathbf{Op}} \\ -\mathbf{\Omega}_{\mathbf{mN},\mathbf{Op}} & \mathbf{A}_{\mathbf{mN},\mathbf{Og}} \end{bmatrix} \begin{bmatrix} \mathbf{x}_{\mathbf{mN}} \\ \mathbf{y}_{\mathbf{mN}} \end{bmatrix} + \begin{bmatrix} \mathbf{B}_{\mathbf{mN},\mathbf{Og}} & 0 \\ 0 & \mathbf{B}_{\mathbf{mN},\mathbf{Og}} \end{bmatrix} \begin{bmatrix} \mathbf{u}_{\mathbf{mN}} \\ \mathbf{y}_{\mathbf{mN}} \end{bmatrix}, \quad (6.13)$$

$$\begin{bmatrix} \mathbf{y}_{\mathbf{mN}} \end{bmatrix} = \begin{bmatrix} \mathbf{C}_{\mathbf{mN},\mathbf{Og}} & 0 \\ 0 & \mathbf{C}_{\mathbf{mN},\mathbf{Og}} \end{bmatrix} \begin{bmatrix} \mathbf{x}_{\mathbf{mN}} \\ \mathbf{y}_{\mathbf{mN}} \end{bmatrix}$$

with

$$\mathbf{A}_{\mathbf{mN},\mathbf{Og}} = \begin{bmatrix} 0 & 1 \\ -\frac{c'_N}{m_N} & -\frac{d_N}{m_N} \end{bmatrix}, \mathbf{B}_{\mathbf{mN},\mathbf{Og}} = \begin{bmatrix} 0 & 0 \\ \frac{A_N}{m_N} & \frac{1}{m_N} \end{bmatrix}$$

$$, \Omega_{\mathbf{mN},\mathbf{Op}} = \begin{bmatrix} \omega_{Op} & 0 \\ 0 & \omega_{Op} \end{bmatrix}, \mathbf{C}_{\mathbf{mN},\mathbf{Og}} = \begin{bmatrix} 1 & 0 \end{bmatrix}, \text{ and}$$

$$\mathbf{x}_{\mathbf{mN}} = [x_{tN,s}, \dot{x}_{tN,s}, x_{tN,c}, \dot{x}_{tN,c}]^T$$

$$\mathbf{u}_{\mathbf{mN}} = [u_{piN,s}, f_{mN,s}, u_{piN,c}, f_{mN,c}]^T$$

$$\mathbf{y}_{\mathbf{mN}} = [x_{tN,s}, x_{tN,c}]^T .$$

### 6.2.4 Dynamic Behavior Analysis

Integrating the electrical and mechanical subsystem description based on the state-space generalized averaging model enables to build the averaged model diagram illustrated in Fig. 6.2 for the MM-USM and its supply.

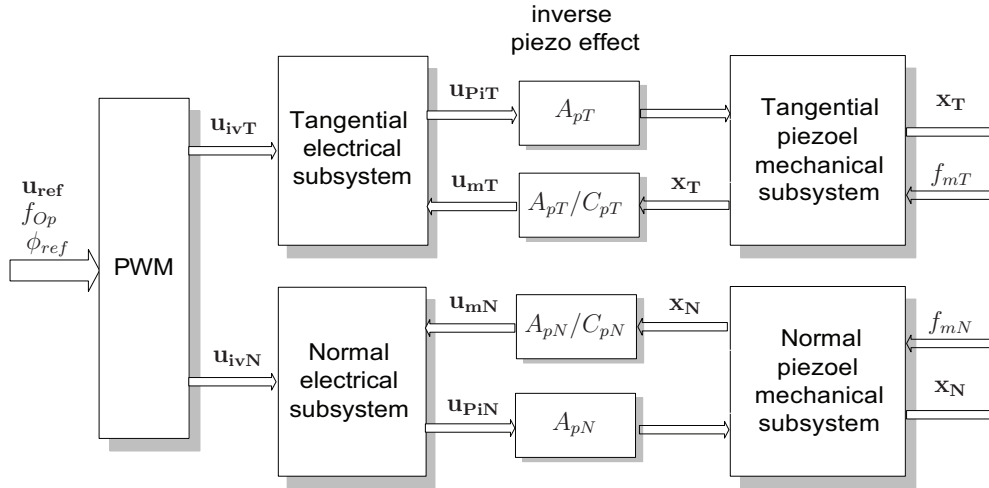


Figure 6.2: Averaged model of MM-USM for power-supply control design

The calculated state-space models are built in Simulink/Matlab to carry out transient simulations using parameters of PIBRAC's MM-USM in Tab. 2.2. Simulation results of a step response of voltage fundamental amplitudes  $[u_{iv,s}, u_{iv,c}]$  from  $[0, 0]$  to  $[180 \text{ V}, 0]$  and set to  $[0, 180 \text{ V}]$  are presented in Fig. 6.3.

## 6. CONTROL DESIGN OF POWER SUPPLY

From performed simulation we notice some oscillatory effect in the averaging model and the original system. The reason originates from the resonance of the mechanical subsystem, indicating the trend: The more damping exists in the mechanical subsystem, the smaller the excited oscillation amplitude is.

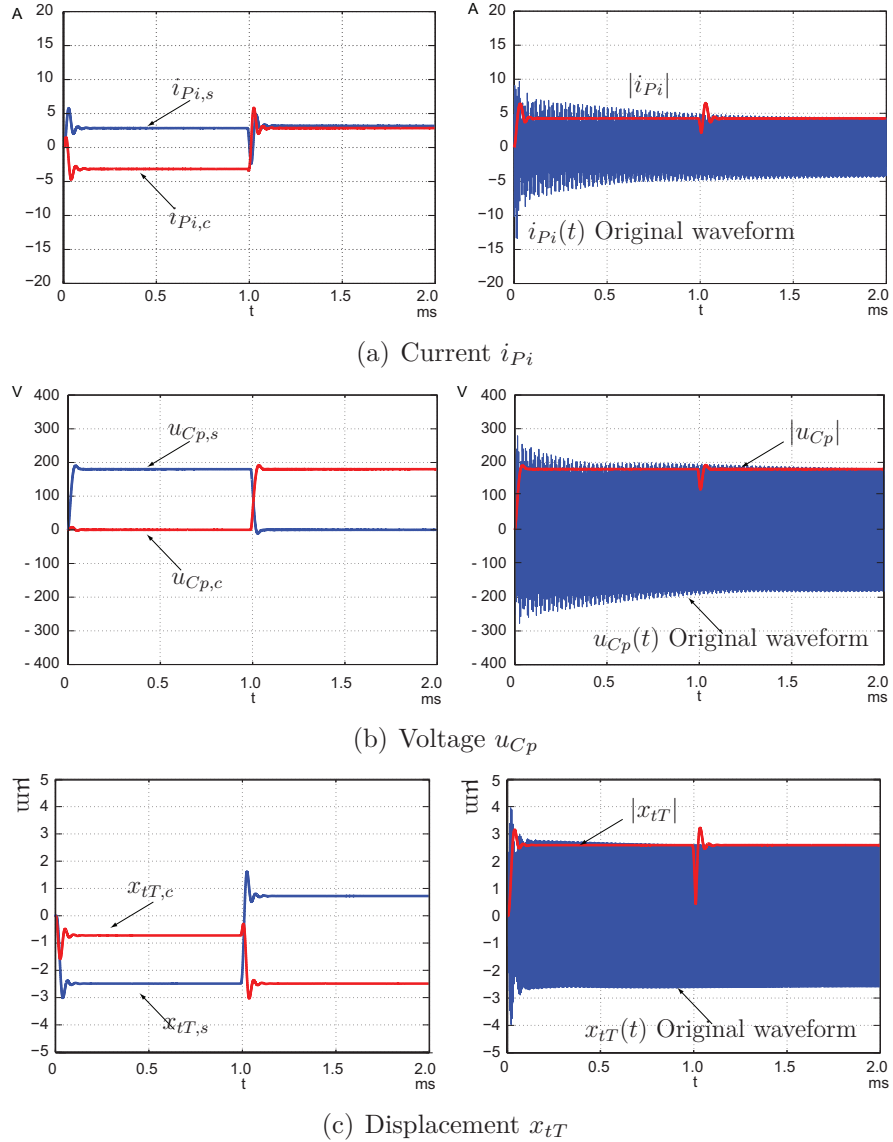


Figure 6.3: Averaging model simulation waveforms of tangential-mode piezoelectric actuator

From the state-space equation 6.5, two conjugate-complex poles  $P_{Avg}$  are derived for the averaging model of the electrical subsystem consisting of the LLCC-filter

## 6.2 Modeling of MM-USM Driven by LLCC-PWM Inverter

circuit as follows [Mas98] and [Sch04a]:

$$P_{Avg} = P_{PI} \pm j\omega_{Op} = \delta_{el} \pm j(\omega_{el} \pm \omega_{Op}), \text{ with } P_{PI} = \delta_{el} \pm j\omega_{el},$$

where  $P_{PI}$  are the conjugate-complex poles of the LLCC filter.

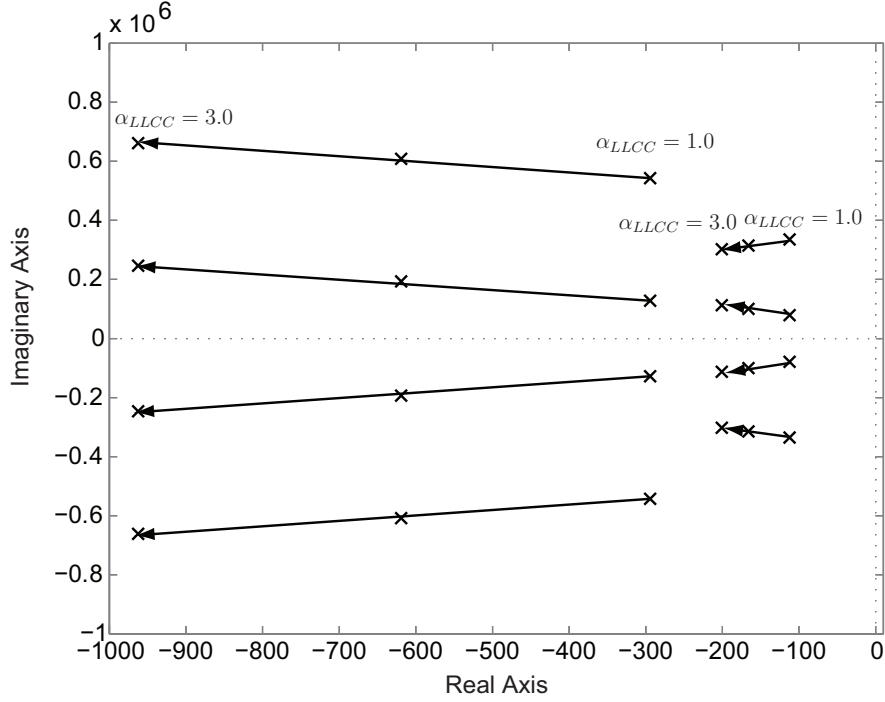


Figure 6.4: Poles of LLCC filter with variation of  $\alpha_{LLCC}$

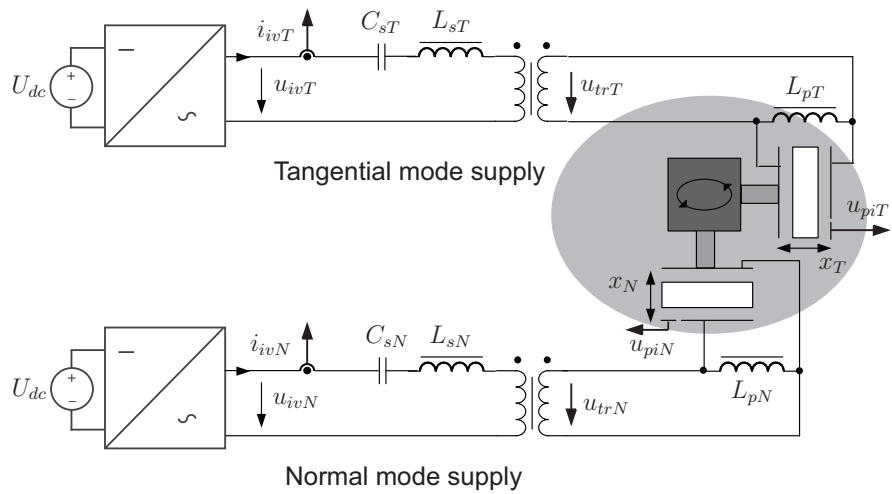
The poles location of the averaging state-space model of the LLCC filter are presented in 6.4 with variation of design parameter  $\alpha_{LLCC}$  defined in Eq. 3.15, from which it can be observed that increasing  $\alpha_{LLCC}$  from 1.0 to 3.0,  $\delta_{el}$  is increasing, whereby the conjugate-complex poles are moved to the left of the s-plane. Moreover the natural frequencies of the dominating conjugate-complex poles are also increasing slightly. Hence, we note that the impulse response of the LLCC-filter circuit decays faster and oscillates at a higher damped frequency, if  $\alpha_{LLCC}$  is increased.

By means of a PWM-controlled LLCC filter, it is possible to increase the design parameter  $\alpha_{LLCC}$  up to 3.0, so that the dynamic behavior is improved compared to the LLCC-resonant inverter. This discovery is the background for the novel drive concept based on a PWM inverter followed by a LLCC filter.

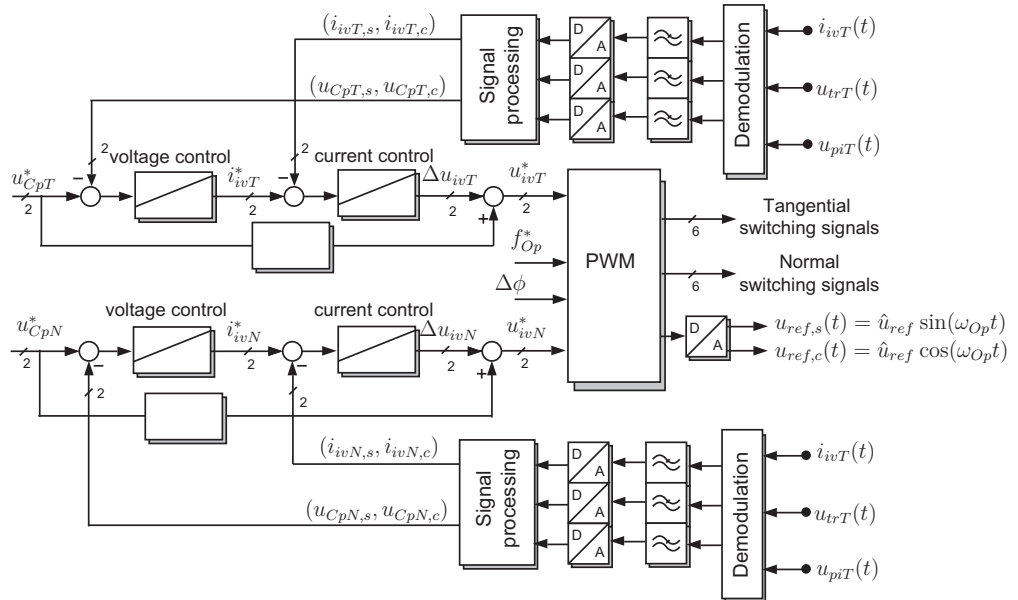
## 6. CONTROL DESIGN OF POWER SUPPLY

### 6.3 Voltage and Current Control Scheme Based on FPGA Implementation

#### 6.3.1 Voltage and Current Control Schemes



(a) Signal Measurement



(b) Cascaded voltage and current control scheme

Figure 6.5: Control and measurement

## 6.3 Voltage and Current Control Scheme Based on FPGA Implementation

---

The control scheme shown in Fig. 6.5(b) is designed to satisfy the aircraft brake system requirements and provide a proper amount of flexibility for commissioning [Wat07]. The reference variables are motor voltage  $u_{Cp}^*$ , ( $u_{Cp,s}^*$ ,  $u_{Cp,c}^*$ ), frequency  $f_{Op}^*$  and phase angle  $\Delta\phi$ . The feedback signals are current  $i_{iv}$ , voltage  $u_{tr}$  and voltage  $u_{pi}$  of a piezoelectric element used as sensor indicating the position of the oscillating mass.

### 6.3.2 Measurement and Signal Processing Scheme

The signal measurement shown in Fig. 6.5(a) provides the required electrical variables to the controller. These variables include:

1. LLCC filter current for the tangential-mode excitation  $i_{ivT}$  and the normal-mode  $i_{ivN}$
2. Transformer secondary voltages  $u_{trT}$  and  $u_{trN}$ , which can be considered as piezoelectric actuator voltages  $u_{CpT}$  and  $u_{CpN}$  for this prototype
3. Piezoelectric-sensor signals  $u_{piT}$  and  $u_{piN}$ , which provide the information about the mechanical oscillation amplitude

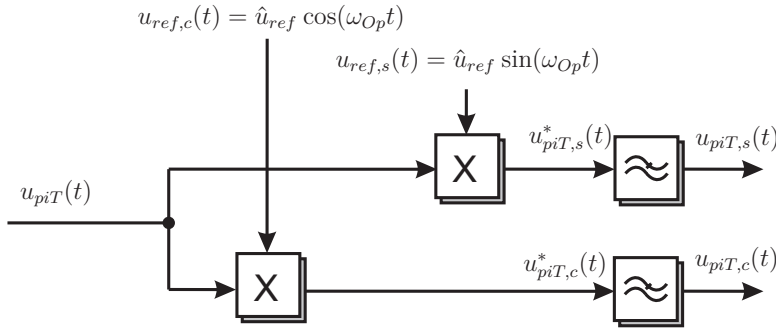


Figure 6.6: Phase sensitive demodulation

In order to reduce the calculation requirements of the signal measurement processing, an analog demodulation shown in Fig. 6.6 is utilized to deliver the sine and cosine components of the measured signals  $u_{piT}(t)$ , which equal the first order Fourier coefficients.

## 6. CONTROL DESIGN OF POWER SUPPLY

---

The controller generates PWM switching signals based on the set value  $u_{set}$  of the inverter output voltage and provides also the reference of sine and cosine values ( $u_{ref,s}(t)$ ,  $u_{ref,c}(t)$ ) for the demodulation algorithms.

### 6.3.3 Feed-Forward Voltage Control

The proposed feed-forward voltage control scheme is presented in Fig. 6.7. The electrical subsystem is replaced by a system consisting of a main transfer function  $G_{el,main}(z)$  and a coupled transfer function  $G_{el,couple}(z)$ , supplemented by a second-order Butterworth filter as pre-filter.

$$G_{f,el}(z) = \frac{1 + 2z^{-1} + z^{-2}}{1 + b_1z^{-1} + b_2z^{-2}} \quad (6.14)$$

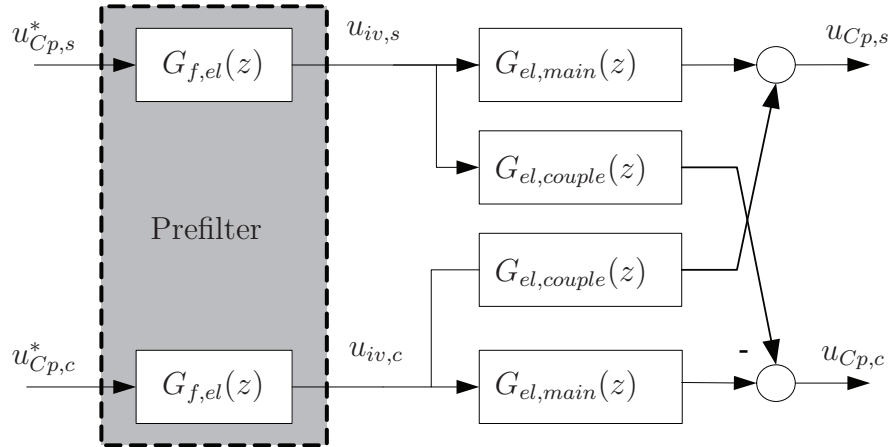
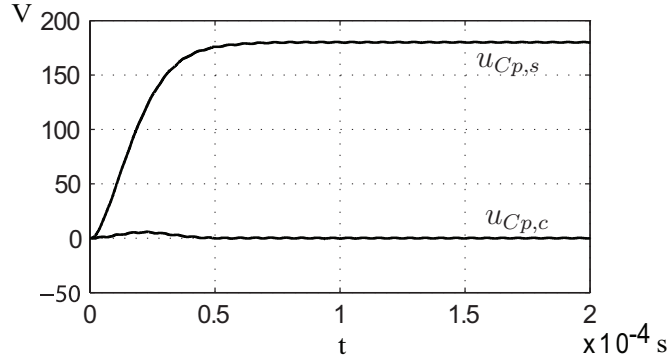


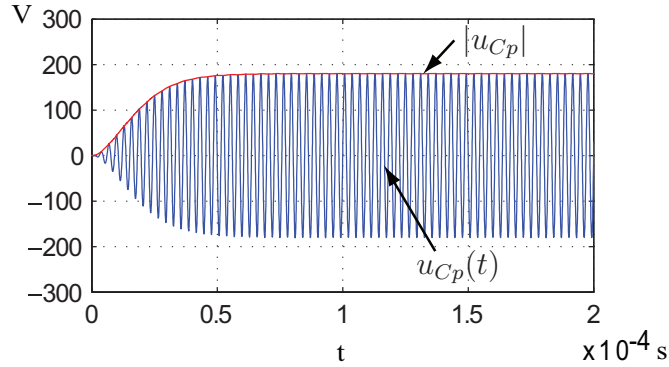
Figure 6.7: Feed-forward voltage control diagram

In Fig. 6.8 step-response simulation results of the voltage control are presented, with the amplitude calculated by  $|u_{Cp}| = \sqrt{u_{Cp,s}^2 + u_{Cp,c}^2}$ . Comparing simulation results in Fig. 6.8 with those in Fig. 6.3, one should note that the oscillatory effects are well damped by feed-forward voltage control.

### 6.3 Voltage and Current Control Scheme Based on FPGA Implementation



(a) Sine and cosine component



(b) Voltage of piezoelectric actuator

Figure 6.8: Simulation results of voltage control

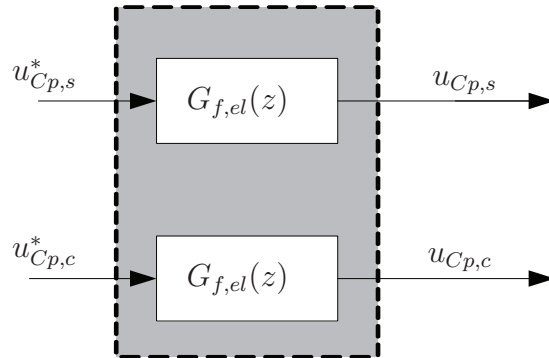


Figure 6.9: Simplified electrical subsystem with feed-forward control

Due to the robust characteristics of the LLCC-filter circuit in the proximity of  $\omega_{Op}$ , the electrical subsystem can be simplified by the pre-filter characteristic. This provides a simple inner-loop transfer function in order to design outer mechanical oscillation amplitude control.

### 6.4 Experiment on Driving MM-USM

The first joint test of the PIBRAC power-supply prototype and the motor prototype was carried out by combined efforts of SAGEM and UPB [Pib08b]. In Fig. 6.10 the configuration of the test is presented.

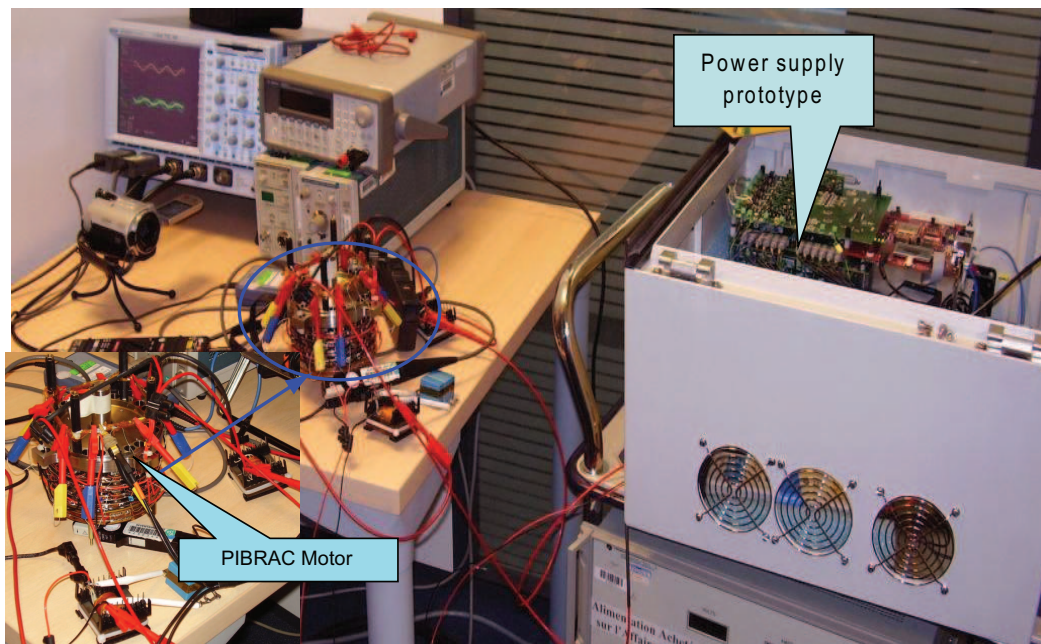


Figure 6.10: PIBRAC power supply and motor test configuration

A DC source provides the DC input voltage to the PIBRAC power-supply prototype. The parallel inductors  $L_p$  are connected closely to the tangential-mode and normal-mode piezoelectric actuators. The power supply provides the voltages with phase shift to the tangential-mode and normal-mode piezoelectric actuators, its amplitude can be varied by the DC source or the voltage controller of the power supply.

Selected waveforms of the motor tests are presented in Fig. 6.11, where the voltages of each mode of the piezo-actuators are set to 80 V, the operating frequency to 31 kHz; the total power delivered to the motor amounts to 150 W. From Fig. 6.11 it is observed that the current and voltage of tangential mode show fine sinusoidal waveforms, which are congruent with the test results using the equivalent load in Fig. 4.31 and Fig. 5.14. But the normal-mode current

## 6.4 Experiment on Driving MM-USM

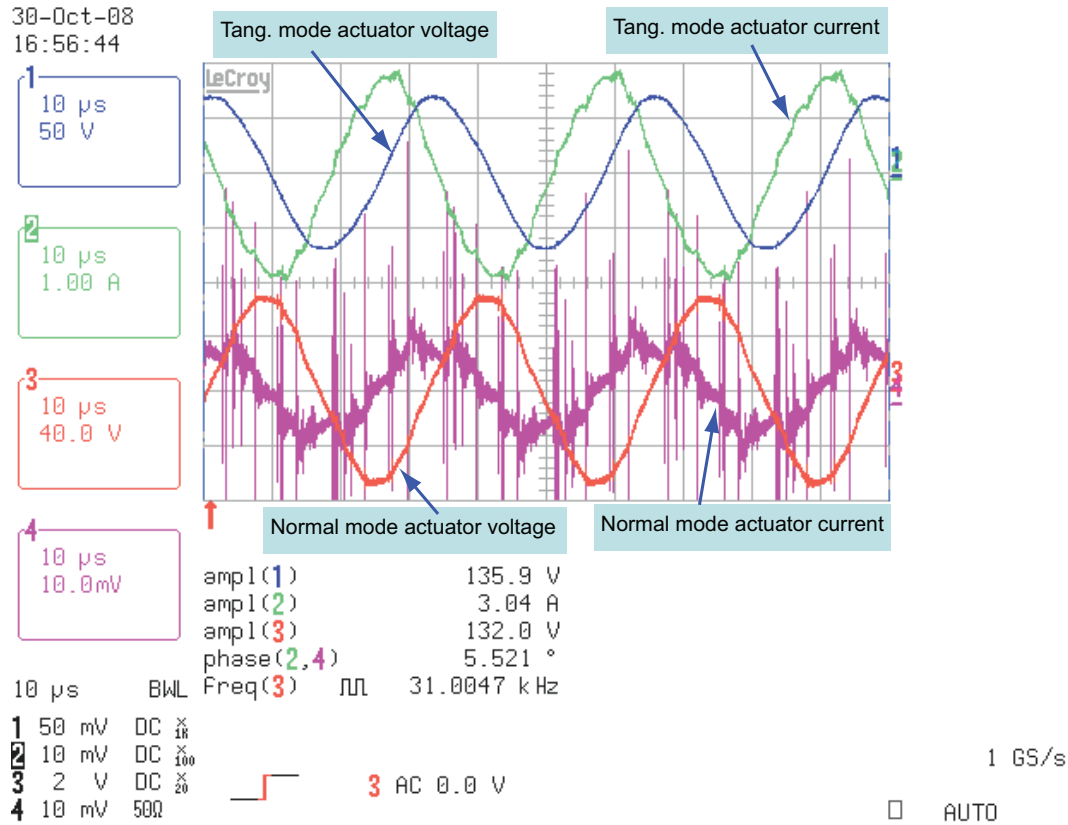


Figure 6.11: Test results of MM-USM's current and voltage

waveform contains a high degree of distortion. The reason is that the resonance frequency of the normal-mode piezoelectric stack differs from the resonance frequency of the tangential mode. Hence the current amplitude is very small due to the small admittance of the normal-mode piezoelectric actuator at this operating frequency.

### 6.5 Summary

In order to provide a stable voltage to the MM-USM, the inner voltage and current control loop is investigated and presented in this chapter as follows:

- Objective of inner control loop is defined.
- An averaging model of the MM-USM driven by the LLCC PWM inverter is set up. It is useful for simplifying the control and signal processing design, because it avoids to process the high-frequency variables directly.
- A cascaded voltage- and current-control scheme including its measurement and signal processing schemes are introduced.
- A feed-forward voltage controller is designed and implemented based on a simplified inner-loop transfer function, to regulate voltage provided to MM-USM and to enable outer mechanical loop design.

# Chapter 7

## Conclusion

More powerful piezoelectric systems become available due to the recent advancements of piezoelectric actuator technology. With their occurrence for utilizing the potential in respect to power density and control bandwidth enhancements, high-performance multi-phase power supplies are required, which can be loaded capacitatively and offer a control via several set quantities.

In order to enable the use of a MM-USM under the constraints of an aircraft brake application, high switching frequency, high efficiency, reactive-power compensation and advanced modulation technology are selected measures to reach the project objectives of PIBRAC. The goal of this work is to develop power supply technologies to meet and exceed these challenges.

In summary, the following original contributions are made in this study of power supplies for driving a high-power piezoelectric ultrasonic motor for a brake actuator application.

1. A comprehensive literature survey is presented on reactive-power compensation, harmonic distortion, multilevel inverter techniques, filter circuit design issues, control issues, and fundamental issues of piezoelectric actuator drive schemes. The various aspects associated with the inverter and the filter circuits used in the power supply for driving piezoelectric actuators are characterized and studied in depth. The following results are obtained in this study.
  - (a) A resonant inverter with LLCC-type filter shows advanced characteristics and best suited properties with respect to efficiency, stationary and

## 7. CONCLUSION

---

dynamic behavior, as well as to control and commissioning efforts. The drawbacks of these resonant inverters are the large volume, heavy and costly magnetic components of the resonant filter like the transformer and inductor, especially in case of driving piezoelectric actuators in the range of some kW.

- (b) A LC-PWM inverter provides the potential to reduce the size and the weight of magnetic components. It was shown that LC-PWM inverters are only suitable for weakly damped piezoelectric vibration systems, where less reactive power is required by the piezoelectric actuator. Thanks to the high switching frequencies, the inductivity  $L_s$  can be decreased significantly in comparison to those used in resonant filters. This results in smaller and lighter components. However, the high switching frequency of PWM inverters consequently results in too high switching losses and might be in conflict with EMC issues.
2. To overcome the drawbacks of the state-of-the-art power supplies, a new LLCC-PWM inverter topology is proposed and verified through simulation and experiments. The proposed inverter's name is abbreviated due to the use of a LLCC-filter circuit and operation in PWM-controlled mode. The solution provides significant advantages to improve the performance of the power supply:
- (a) The reactive power of the piezoelectric actuator is compensated locally, by placing the inductor  $L_p$  close to the actuator. Hence, inverter, resonant components, transformer and cables of considerable length between output transformer and actuators can be rated mainly with respect to the transmitted active power.
  - (b) A thoroughly designed LLCC filter exhibits the required robustness in respect to parameter variations, and enables the reduction in size of filter components and the utilization of cable parasitics. The cable weight is also minimized by the reduction of RMS-current rating arising from local reactive-power compensation.

- 
- (c) By combining the PWM method and the reactive-power compensation, the output filter shows optimized performance with minimized volume and weight, compared to the classical resonant inverters. It is necessary to save the volume and the weight, in order to satisfy one target of the PIBRAC project.
3. In order to suppress the lower-order harmonics, two-level and three-level harmonic elimination techniques are investigated to determine the suitable switching angles. The following results are obtained in this work:
- (a) The low-order harmonics of inverter output voltage are eliminated by HEM, in which Newton algorithm is employed to calculate the switching angles.
  - (b) The total harmonic distortion (THD) of the piezoelectric actuator voltage is reduced without increasing the switching frequency compared with a LC-PWM inverter.
4. A control algorithm for the inner voltage- and current-control loop of the power supply is proposed and discussed. Several results are achieved in this work.
- (a) For control design an averaging model of the MM-USM driven by LLCC PWM inverter is studied and verified by simulation results at transient and steady state conditions.
  - (b) A feed-forward voltage controller is designed and implemented, based on a simplified inner loop transfer function, to regulate voltage of the MM-USM and to enable outer mechanical loop design. Simulation results and experiments indicate that the proposed controller can maintain the constant piezoelectric actuator voltage with expected phase shift.
  - (c) A FPGA is employed as controller by reason of its flexibility, fast and parallel processing characteristics.

## 7. CONCLUSION

---

Methodology and technology investigated in this dissertation are suitable for direct piezoelectric drive applications for airplanes, cars, robotics and medical measurement apparatus, where a piezoelectric actuator is employed. Other fields of application are: superimposed sonotrode-assisted ultrasonic drilling, cutting and milling of tooling machines.

# Bibliography

- [AAOW06] E. Agostini, J-T. Audren, S. Ouchouche, and M. Woydt. High power piezoelectric motor for brake actuator pibrac project. *International Council of the Aeronautical Sciences 2006, Hamburg, Germany*, September 2006.
- [AB03] J-T. Audren and D. Bezanere. Vibration motors. United States Patent 6628044, September 2003.
- [ADC<sup>+</sup>00] K. Agbossou, J.-L. Dion, S. Carignan, M. Abdelkrim, and A. Cheriti. Class d amplifier for a power piezoelectric load. *IEEE Transaction on Ultrasonics, Ferroelectrics, and Frequency Control*, Vol. 47, No. 4, pp. 1036-1041, July 2000.
- [AMC07] E. Agostini, E. Merlet, and F. Cugnon. Piezoelectric motor for brake actuator. *10th SAMTECH Users Conference 2007*, March 2007.
- [BH05] T. Brückner and G. Holmes. Optimal pulse-width modulation for three-level inverters. *IEEE Transactions on Power Electronics*, Vol. 20, No. 1, pp. 82-89, 2005.
- [BS83] P. Bhagwat and V. Stefanovic. Generalized structure of a multilevel pwm inverter. *IEEE Transactions on Industry Applications*, Vol. IA-19, pp. 1057-1069, 1983.
- [CJ93] M. Cirvii and M. Jufer. Dc to ac converters for piezoelectric motors. *Proceedings of European Conference on Power Electronics and Applications (EPE 93), Brighton*, 1993.

## BIBLIOGRAPHY

---

- [CU01] A. V. Carazo and K. Uchino. Novel piezoelectric-based power supply for driving piezoelectric actuators designed for active vibration damping applications. *Journal of Electroceramics*, pp. 197-210, July 2001.
- [Dau72] D. Daum. Unterdrückung von Oberschwingungen durch Pulsbreitensteuerung. *ETZ-A 93*, Vol. H. 9, pp. 528-530, 1972.
- [EM00] R.-W. Erickson and D. Maksimovic. *Fundamentals of Power Electronics 2nd Edition*. Kluwer Academic Publishers, 2000.
- [Fal06] L. Faleiro. Summary of the European Power Optimised Aircraft (POA) project. *25th International Congress of the Aeronautical Sciences (ICAS)*, 2006.
- [Gna05] G. Gnad. Ansteuerungskonzept für piezoelektrische Aktoren. *Dissertation am Institut für Mechatronik und Antriebstechnik, Otto-von-Guericke-Universität Magdeburg*, 2005.
- [Gro02] H. Grotstollen. An introduction to resonant operated piezoelectric actuators. *International Symposium on Electrical Engineering Education, Beijing, China*, pp. 225-229, November 2002.
- [Gro04] H. Grotstollen. Supply and control of piezoelectric systems. *Deutsch-Koreanisches Symposium, Aachen, Germany*, June 2004.
- [Hol03] Grahame Holmes. *Pulse Width Modulation for Power Converters*. Wiley-IEEE Press, 2003.
- [IEE10] IEEE Std 1459-2010 (revision of IEEE Std 1459-2000), IEEE standard definitions for the measurement of electric power quantities under sinusoidal, nonsinusoidal, balanced, or unbalanced conditions. IEEE Standards, 2010.
- [JC06] P. Jänker and F. Claeysen. New actuators for aircraft and space applications. *Proceedings of 12th International Conference on New Actuators, ACTUATOR 2006, Bremen*, pp. 324-329, 2006.

## BIBLIOGRAPHY

---

- [JGvdB04] P. Jänker, B. A. Grohmann, and D. van den Bossche. Actuator technology - driver of aerospace system innovation -. *Proceedings of 10th International Conference on New Actuators, ACTUATOR 2004, Bremen*, pp. 168-176, 2004.
- [JQ02] H. Janocha and R. Quinten. New power amplifier concept for piezoelectric actuators. *Proceedings of 8th International Conference on New Actuators, ACTUATOR 2002, Bremen*, pp. 462-465, 2002.
- [KF04] C. Kauczor and N. Fröhleke. Inverter topologies for ultrasonic piezoelectric transducers with high mechanical q-factor. *Proceedings of 35th Annual IEEE Power Electronics Specialists Conference (PESC 2004), Germany*, 2004.
- [KSF02] C. Kauczor, T. Schulte, and N. Fröhleke. Resonant power converter for ultrasonic piezoelectric converter. *Proceedings of 8th International Conference on New Actuators, ACTUATOR 2002, Bremen*, 2002.
- [LÖ6] M. Lönneker. *Vergleich von Modulationsverfahren und Filtern für einen wechselrichtergespeisten Ultraschall-Motor hoher Leistung*. Universität Paderborn, Studienarbeit im Fachgebiet Leistungselektronik und Elektrische Antriebstechnik, December 2006.
- [LÖ7] M. Lönneker. *Optimierte Modulation eines 3-Punkt-Wechselrichters mit LLCC-Filter zur Speisung eines Ultraschall-Motors*. Universität Paderborn, Diplomarbeit im Fachgebiet Leistungselektronik und Elektrische Antriebstechnik, October 2007.
- [LDH99] F.-J. Lin, R.-Y. Duan, and C.-M. Hong. Llcc resonant inverter for piezoelectric ultrasonic motor drive. *Proceedings of IEEE Electric Power Applications*, Sep 1999.
- [LDL99] F.-J. Lin, R.-Y. Duan, and H.-H. Lin. An ultrasonic motor drive using llcc resonant technique. *Proceedings of 30th Annual IEEE Power Electronics Specialists Conference (PESC '99)*, 1999.

## BIBLIOGRAPHY

---

- [Len74] A. Lenk. *Elektromechanische Systeme*, volume 2: System mit verteilten Parametern. VEB Verlag Technik Berlin, 1974.
- [LFB08] R. Li, N. Fröhleke, and J. Böcker. Llcc-pwm inverter for driving high power piezoelectric actuators. *Proceedings of EPE-PEMC 2008*, 2008.
- [LFWB06a] R. Li, N. Fröhleke, H. Wetzel, and J. Böcker. Power supply and control scheme for an airborne piezoelectric brake actuator. *Proceedings of 10th International Conference on New Actuators (ACTUATOR 2006), Bremen*, 2006.
- [LFWB06b] R. Li, N. Fröhleke, H. Wetzel, and J. Böcker. Investigation of power supplies for a piezoelectric brake actuator in aircrafts. *Proceedings of International Power Electronics and Motion Control Conference (IPEMC 2006), Shanghai, China*, August 2006.
- [LLBC01] R. L. Lin, F. C. Lee, E. M. Baker, and D. Y. Chen. Inductorless piezoelectric transformer electronic ballast for linear fluorescent lamp. *Proceedings of APEC 2001, Anaheim, CA*, Vol. 14, No. 1, pp. 31-42, März 2001.
- [LLFB08] R. Li, M. Lönneker, N. Fröhleke, and J. Böcker. Design of power supply for driving high power piezoelectric actuators. *Proceedings of IAS 2008*, 2008.
- [LZS<sup>+</sup>02] D.-K. Lindner, H. Zhu, C. Song, W. Huang, and D. Cheng. Driver circuit for piezoelectric motor. *Proceedings of SPIE's 2002 North American Symposium on Smart Structures and Materials, San Diego, CA*, March 2002.
- [LZVL02] D.-K. Lindner, H. Zhu, N. Vujic, and D. Leo. Comparison of linear and switching drive amplifiers for piezoelectric actuators. *Proceedings of the AIAA/ASME/ASCE/AHS/ASC 43th Structures, Structural Dynamics, and Materials Conference, Denver, CO*, April 2002.

## BIBLIOGRAPHY

---

- [Mas98] J. Mass. *Modellierung und Regelung von stromrichter-gespeisten Ultraschall-Wanderwellenmotoren*. Dissertation Universität Paderborn, Fortschritt-Berichte VDI Verlag, 1998.
- [MB06] Messier-Bugatti. Electric on track for smooth introduction brake. <http://www.messier-bugatti.com>, 2006.
- [McL04] Colonel Wm. T. McLyman. *Transformer and Inductor Design Handbook, Third Edition*. CRC, 2004.
- [MG97] J. Maas and H. Grotstollen. Averaged model of inverter-fed ultrasonic motors. *Proceedings of 28th Annual IEEE Power Electronics Specialists Conference (PESC '97)*, 22-27 June 1997.
- [MKFG95] J. Maas, P. Krafska, N. Fröhleke, and H. Grotstollen. Prototype drive and modulation concepts for dsp-controlled ultrasonic motors powered by resonant converters. *Proceedings of EPE'95, Sevilla, Spain*, 1995.
- [MSF00] J. Maas, T. Schulte, and N. Fröhleke. Model-based control for ultrasonic motors. *IEEE/ASME Transactions on Mechatronics*, Vol. 5, No. 2, pp. 165-180, June 2000.
- [MSG97] J. Maas, T. Schulte, and H. Grotstollen. Optimized drive control for inverter-fed ultrasonic motors. *Proceedings of Thirty-Second IEEE Industry Applications Conference (IAS '97)*, 5-9 Oct. 1997.
- [NF01] H.-D. Njiende and N. Fröhleke. Optimization of inductors in power converter feeding high power piezoelectric motors. *Proceedings of Aupec 2001*, 2001.
- [NTA81] A. Nabae, I. Takahashi, and H. Akagi. A new neutral-point-clamped pem inverter. *IEEE Transactions on Industry Application*, Vol. IA-17, pp. 518-523(5), 1981.

## BIBLIOGRAPHY

---

- [PH73] H. Patel and R. G. Hoft. Generalized techniques of harmonic elimination voltage control of thyristor inverter: Part i — harmonic elimination. *IEEE Transactions on Industry Application*, Vol. IA-9, pp. 310-317(3), 1973.
- [PH74] H. Patel and R. G. Hoft. Generalized techniques of harmonic elimination voltage control of thyristor inverter: Part ii — voltage control techniques. *IEEE Transactions on Industry Application*, Vol. IA-10, pp. 666-673(5), 1974.
- [Pib06a] Pibrac project deliverable d.220.2c: Pibrac wp220 technical specification document - pibrac power controller detailed specifications, 2006.
- [Pib06b] Pibrac project deliverable d.220.4: Pibrac wp220 report - pibrac power consumption estimation, 2006.
- [Pib07a] Pibrac project deliverable d.330.1: Pibrac wp330 report - converter topology description, 2007.
- [Pib07b] Pibrac project deliverable d.330.2: Pibrac wp330 report - modelling and control, 2007.
- [Pib08a] Pibrac project deliverable d.410.1: Pibrac wp410 final report - evaluation of rotational motor, 2008.
- [Pib08b] Pibrac project deliverable d.430.1: Pibrac wp430 final report - prototype description, 2008.
- [SBG94] J. Sun, S. Beineke, and H. Grotstollen. Dsp-based real-time harmonic elimination of pwm inverters. *Proceedings of 25th Annual Power Electronics Specialists Conference (PESC '94)*, 20-25 June 1994.
- [SBG96] J. Sun, S. Beineke, and H. Grotstollen. Optimal pwm based on real-time solution of harmonic elimination equations. *IEEE Transactions on Power Electronics*, Vol. 11, pp. 612-621, July 1996.

## BIBLIOGRAPHY

---

- [SBT04] G. Spiazzi, S. Buso, and P. Tomasin. Cold cathod fluorescent lamp power supply based on piezoelectric transformers. *Proceedings of IEEE Power Electronics Specialists Conference (PESC 2004)*, Germany, 2004.
- [Sch04a] T. Schulte. *Stromrichter- und Regelungskonzepte für Ultraschall-Wanderwellenmotoren*. Dissertation Universität Paderborn, Fortschritt-Berichte VDI Verlag, 2004.
- [Sch04b] Hubert Schwetlick. *Numerische Lösung nichtlinearer Gleichungen*. R. Oldenbourg Verlag München Wien, 2004.
- [SF01] T. Schulte and N. Fröhleke. Development of power converter for high power piezoelectric motors. *Proceedings of AUPEC 2001*, 2001.
- [SFG00] T. Schulte, N. Fröhleke, and H. Grotstollen. Control for ultrasonic motors with llcc-resonant converter. *Proceedings of 7th International Conference on New Actuators (ACTUATOR 2000)*, Bremen, Germany, Juni 2000.
- [SJ00] C. Stiebel and H. Janocha. 6 kv power amplifier designed for actuators with electrorheological (er) fluids. *Proceedings of 7th International Conference on New Actuators (ACTUATOR 2000)*, Bremen, pages pp. 135–138, 2000.
- [SNLV91] S. R. Sanders, J. M. Noworolski, X. Z. Lui, and G. C. Verghese. Generalized averaging method for power conversion circuits. *IEEE Transactions on Power Electronics*, Vol. 6, Nr. 2, pp. 251-258, 1991.
- [STJ01] C. Stiebel, Würtz. T., and H. Janocha. Leistungsverstärker für piezoelektrische aktoren. *Elektronik*, December 2001.
- [Sun95] J. Sun. *Optimal Pulsewidth Modulation Techniques for High-Power Voltage-Source Inverters*. Dissertation Universität Paderborn, Fortschritt-Berichte VDI Verlag, 1995.

## BIBLIOGRAPHY

---

- [Uch97] K. Uchino. *Piezoelectric Actuators and Ultrasonic Motors*. Kluwer Academic Publishers, 1997.
- [Wal95] J. Wallaschek. Piezoelectric ultrasonic motors. *Journal of Intelligent Material Systems and Structures*, Vol.6, pp. 71-83, Jan. 1995.
- [Wat07] M. Wattenberg. *Entwicklung einer Schnittstelle für Leistungsverstärker zur Speisung eine MM-USM (Multi-Mass Ultrasonic Motor)*. Universität Paderborn, Studienarbeit im Fachgebiet Leistungselektronik und Elektrische Antriebstechnik, February 2007.
- [WFB<sup>+</sup>06] H. Wetzel, N. Fröhleke, J. Böcker, S. Ouchouche, D. Bezanere, and F. Cugnon. Modelling and control of a multi-mass ultrasonic motor for airborne applications. *Proceedings of International Electronics Conference (IECON 2006), Paris, Frankreich*, November 2006.
- [WLFB07] H. Wetzel, R. Li, N. Fröhleke, and J. Böcker. Piezoelektrische flugzeugbremse. *Workshop Entwurf mechatronischer Systeme 2007, Paderborn, Germany*, März 2007.
- [xil06] Xilinx logiccore dds v5.0, 2006.
- [ZL98] G. A. Zvonar and D. K. Lindner. Power flow analysis of electrostrictive actuators driven by switch mode amplifiers. *Journal on Intelligent Material Systems and Structures, special issue on the 3rd Annual ARO Workshop on Smart Structures*, Vol. 9, No 3, pp. 210-222, March 1998.

# Appendix A

## Definition

### A.1 Power Factor

The power factor  $\lambda$  is defined in [IEE10] as:

$$\lambda = \frac{|P|}{S} \quad (\text{A.1})$$

$$\lambda = \frac{|\cos(\angle Y(f_{\text{BN}}))|}{\sqrt{1 + \text{THD}_u^2} \cdot \sqrt{1 + \text{THD}_i^2}} \quad (\text{A.2})$$

### A.2 General Fourier Coefficient Solution of Inverter Voltage

Fig. A.1 presents four kinds of normalized inverter voltage waveforms, in which the waveforms in Fig. A.1(a, b) have  $n$  switching angles, and the waveforms in Fig. A.1(c, d) have  $n + 1$  switching angles.

The switching angles are independent in the first quarter of the waveform, and the rest are dependent and symmetric. The independent switching angles should satisfy the condition:

$$0 \leq \alpha_1 \leq \dots \leq \alpha_n \leq \frac{\pi}{2} \quad (\text{A.3})$$

## A. DEFINITION

---

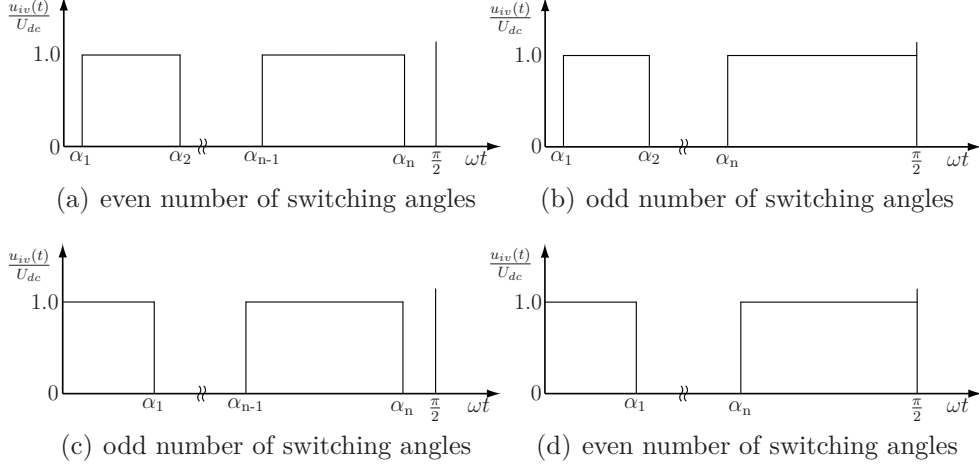


Figure A.1: Possible output-voltage waveforms of inverter

According to the symmetry of the waveforms, the angles group in one period can be described as:

$$\begin{cases} \alpha_i = \alpha_i \\ \alpha_{n+i} = \pi - \alpha_{n+1-i} \\ \alpha_{2n+i} = \pi + \alpha_i \\ \alpha_{3n+i} = 2\pi - \alpha_{n+1-i} \end{cases}, \quad i = 1 \dots n \quad (\text{A.4})$$

The Fourier coefficient  $U_{\nu_{iv}}$  can be calculated for a normalized voltage  $u_{iv}(t)$  with the DC-link voltage  $U_{dc}$  as:

$$U_{\nu_{iv}} = \frac{1}{2\pi} \int_0^{2\pi} \frac{u_{iv}(t)}{U_{dc}} e^{-j\nu x} dx \quad (\text{A.5})$$

The switching angles decide essentially about the waveform of voltage. Eq. A.5 can be recalculated using the switching angles (see Fig. A.1) as:

$$\begin{aligned} U_{\nu_{iv}} = & \frac{1}{2\pi} \int_{\alpha_1}^{\alpha_2} e^{-j\nu x} dx + \dots + \frac{1}{2\pi} \int_{\alpha_{2n-1}}^{\alpha_{2n}} e^{-j\nu x} dx \\ & - \frac{1}{2\pi} \int_{\alpha_{2n+1}}^{\alpha_{2n+2}} e^{-j\nu x} dx - \dots - \frac{1}{2\pi} \int_{\alpha_{4n-1}}^{\alpha_{4n}} e^{-j\nu x} dx \end{aligned} \quad (\text{A.6})$$

Moreover from Eq. A.4 the switching angles in one period can be replaced by

## A.2 General Fourier Coefficient Solution of Inverter Voltage

---

the switching angles in the first quarter-period, the Fourier coefficient  $U_{\nu_{iv}}$  are:

$$\begin{aligned}
 U_{\nu_{iv}} = & \frac{1}{2\pi} \int_{\alpha_1}^{\alpha_2} e^{-j\nu x} dx + \dots + \frac{1}{2\pi} \int_{\pi-\alpha_2}^{\pi-\alpha_1} e^{-j\nu x} dx \\
 & - \frac{1}{2\pi} \int_{\pi+\alpha_1}^{\pi+\alpha_2} e^{-j\nu x} dx - \dots - \frac{1}{2\pi} \int_{2\pi+\alpha_1}^{2\pi+\alpha_2} e^{-j\nu x} dx
 \end{aligned} \tag{A.7}$$

Considering  $u_{iv}(t)$  being an odd function, the Fourier coefficients  $U_{\nu_{iv}}$  are odd and imaginary numbers:

$$\left. \begin{aligned}
 u_{iv}(x) = -u_{iv}(-x) & \implies U_{\nu_{iv}} = -U_{-\nu_{iv}} \\
 u_{iv}(x) = u_{iv}^*(x) & \implies U_{\nu_{iv}} = U_{-\nu_{iv}}^*
 \end{aligned} \right\} \Rightarrow U_{\nu_{iv}} \tag{A.8}$$

Using Eq. A.7 the Fourier coefficient of each waveform in Fig. A.1 can be derived:

1. Waveform in Fig. A.1(a,b) validate:

$$U_{\nu_{iv}} = \begin{cases} \frac{2}{j\nu\pi} \sum_{i=1}^n (-1)^{i+1} \cos(\nu\alpha_i) & \nu = \{\dots, -3, -1, 1, 3, \dots\} \\ 0 & \text{sonst} \end{cases} \tag{A.9}$$

2. Waveform in Fig. 5.1(c,d) validate:

$$U_{\nu_{iv}} = \begin{cases} \frac{2}{j\nu\pi} - \frac{2}{j\nu\pi} \sum_{i=1}^n (-1)^{i+1} \cos(\nu\alpha_i) & \nu = \{\dots, -3, -1, 1, 3, \dots\} \\ 0 & \text{sonst} \end{cases} \tag{A.10}$$

Because the Fourier coefficient are odd and imaginary (see Eq. A.8), Eq. A.9 and Eq. A.10 can be simplified as:

$$\hat{U}_{\nu_{iv}} = U_{\nu_{iv}} - U_{-\nu_{iv}} \tag{A.11}$$

$$(\text{A.9}) \Rightarrow \hat{U}_{\nu_{iv}} = \frac{4}{j(2\nu-1)\pi} \sum_{i=1}^n (-1)^{i+1} \cos((2\nu-1)\alpha_i) \quad \forall \nu \in \mathbb{N} \tag{A.12}$$

$$(\text{A.10}) \Rightarrow \hat{U}_{\nu_{iv}} = \frac{4}{j(2\nu-1)\pi} \left( 1 - \sum_{i=1}^n (-1)^{i+1} \cos((2\nu-1)\alpha_i) \right) \quad \forall \nu \in \mathbb{N} \tag{A.13}$$

### A.3 Harmonic Elimination Modulation (HEM) Using Newton Algorithm

In order to eliminate the 3th, 5th, 7th,  $\dots$ ,  $n$ th harmonic components, non-linear equations with the required modulation amplitude  $\mathbf{M}_a$  have to be solved using suitable numerical methods [Dau72] [Sun95] [Sch04b]:

$$\boldsymbol{\alpha}^{(j+1)} = \boldsymbol{\alpha}^{(j)} - \frac{(\hat{U}_{iv}(\boldsymbol{\alpha}^{(j)}) - \mathbf{M}_a)}{(\nabla \hat{U}_{iv}(\boldsymbol{\alpha}^{(j)}))}, \quad (\text{A.14})$$

in which  $j$  is the iteration count of the loop, and  $\boldsymbol{\alpha}$  is a vector containing the switching points for inverter:

$$\boldsymbol{\alpha} = (\alpha_1, \alpha_2, \dots, \alpha_n)^T \quad (\text{A.15})$$

and for three-level inverter:

$$\boldsymbol{\alpha} = (\alpha_{1,1}, \dots, \alpha_{1,p}, \alpha_{2,1}, \dots, \alpha_{2,q})^T \quad (\text{A.16})$$

with  $p + q = n$ .

$\mathbf{M}_a$  is the expected modulation amplitude of the fundamental and harmonic components:

$$\mathbf{M}_a = \begin{pmatrix} \hat{U}_{1iv}^* \\ 0 \\ \vdots \\ 0 \end{pmatrix} \quad (\text{A.17})$$

The iterative algorithm is to calculate, until the critical difference  $\Delta\boldsymbol{\alpha}$  is smaller than the expected error  $\epsilon$ :

$$\Delta\boldsymbol{\alpha} = \boldsymbol{\alpha}^{(j+1)} - \boldsymbol{\alpha}^{(j)} < \epsilon, \text{ where } \epsilon = [\epsilon_1 \ \epsilon_2 \ \dots \ \epsilon_n]^T. \quad (\text{A.18})$$

In Fig. A.2, the variable  $j$  is the iteration counter of the loop, and the variable  $k$  decides which kind of waveform from Fig. A.1 is employed for the actual set value.

### A.3 Harmonic Elimination Modulation (HEM) Using Newton Algorithm

---

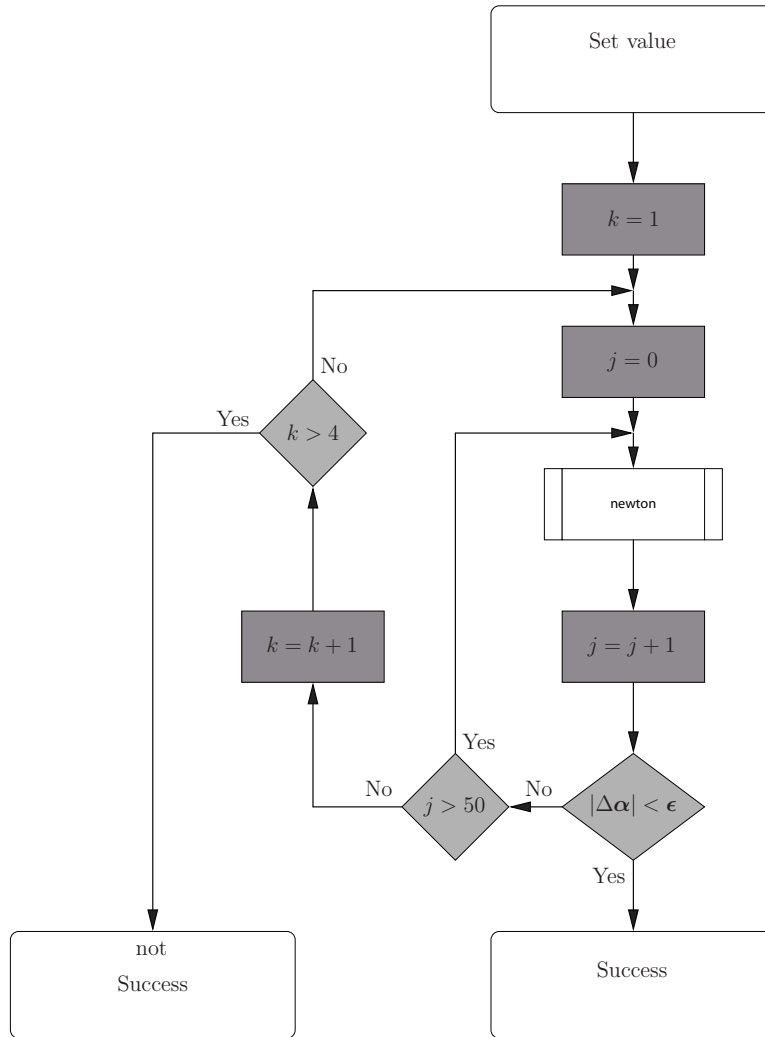


Figure A.2: Diagram for calculation of the switching angles using Newton algorithm

## A.4 Total Harmonic Distortion (THD)

The total harmonic distortion (THD) is defined as the ratio of geometric sum of the harmonic components to the fundamental component. The THD of a voltage and a current waveform is calculated as:

$$THD_u = \frac{\sqrt{U_2^2 + U_3^2 + U_4^2 + \dots + U_n^2}}{U_1} \quad (\text{A.19})$$

$$THD_i = \frac{\sqrt{I_2^2 + I_3^2 + I_4^2 + \dots + I_n^2}}{I_1} \quad (\text{A.20})$$

where  $U_\nu$  and  $I_\nu$  ( $\nu = 1, 2, \dots, n$ ) are the fundamental and harmonic components of the analysed voltage and current.

# Appendix B

## Design Aspects

### B.1 Inductive Components Using Area Products

Using the core Area Product is a widely spread method and it is simply obtained by multiplying the magnetic core cross-section area  $A_{Fe}$  by the window area available for the winding  $A_W$ .

The shape of an E-type magnetic core is shown in Fig. B.1, where  $A_W$  is the cross-section area of the winding, and  $A_{Fe}$  is the cross-section area of the magnetic core. The unit of this area product is  $m^4$ , which is not equal to the normal volume dimension  $m^3$ .

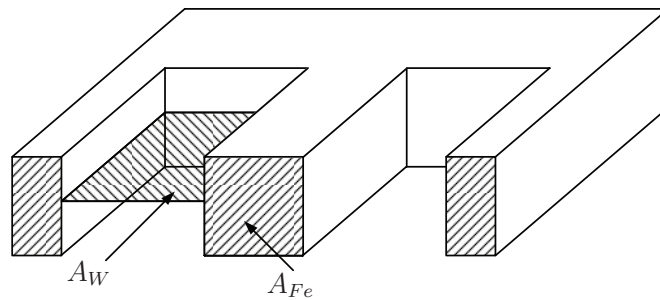


Figure B.1: Shape of an E-type magnetic core

The following formula provides a crude indication of the area product required for inductors and transformers [McL04]:

For inductors:

$$AP_L = A_W A_{Fe} = \frac{L I_{pk} I_{rms}^{4/3}}{B_{MAX} K_1} \quad (B.1)$$

## B. DESIGN ASPECTS

---

For transformers:

$$AP_T = A_W A_{Fe} = \frac{S_o}{\Delta B_{MAX} f_T K_2}^{4/3} \quad (\text{B.2})$$

where the design specification of inductor and transformer is given in Tab. B.1.

Components		Unit
$L$	Inductance	H
$I_{pk}$	Inductor peak current	A
$I_{rms}$	Inductor RMS current	A
$B_{MAX}$	Saturation limited flux density	T
$\Delta B$	Flux density excursion	T
$f_T$	Transformer operating frequency	Hz
$S_o$	Apparent power of transformer	VA
$K_1, K_2$	Influenced by current density and window utilization (depending on design, ambient conditions and conductor material)	

Table B.1: Design specification of inductors and transformers

## B.2 Efficiency Calculations

The total losses  $P_{L,all}$  of one switching components (e.g. MOSFET or Diode) are computed as:

$$P_{L,all} = P_{L,on} + P_{L,off} + P_{L, fwd} + P_{L, cd} \quad (\text{B.3})$$

where  $P_{L,on}$  is switch-on loss,  $P_{L,off}$  is switch-off loss,  $P_{L, fwd}$  forward conduction losses, and  $P_{L, cd}$  charge down losses [EM00].

The geometric and arithmetic mean current (RMS and average current) are employed for calculation of losses of switching components, and are computed as follows:

$$I_{RMS} = \sqrt{\frac{1}{T_F} \int_0^{T_F} i_T^2(t) dt} \quad (\text{B.4})$$

$$I_{AV} = \frac{1}{T_F} \int_0^{T_F} i_T(t) dt \quad (\text{B.5})$$

where  $T_F$  is the duration of the fundamental period.

## B.2 Efficiency Calculations

---

### A. Loss model for MOSFETs

Forward conducting losses of MOSFET:

$$P_{L, fwd} = \frac{1}{T_F} \int_0^{T_F} u_T(t) i_T(t) dt = r_{DSon}(T_j) I_{T,RMS}^2 \quad (\text{B.6})$$

$r_{DSon}(T_j)$  is the drain-source on-state resistance, with junction temperature  $T_j$  chosen at 100 °C.  $I_{T,RMS}$  is the RMS - current flowing through a MOSFET.

Turn-on losses of a MOSFET are calculated using linear approximated waveforms following:

$$P_{L, on} = f_s W_{L, on} = U_d I_{T, av} t_{on} f_s \quad (\text{B.7})$$

The turn-on time equals rising time  $t_r$ , that is  $t_{on} = t_r$ . From these equations we see, that the turn-on losses are increasing linearly with current and switching frequency. By this estimation the losses are considered to rise proportionate to the average current of inductor  $L_s$ .

Turn-off losses of a MOSFET are calculated similarly as follows:

$$P_{L, off} = f_s W_{L, off} = U_d I_{T, av} t_{off} f_s, \quad (\text{B.8})$$

in which the turn-off time is analogously assumed to equal the fall time  $t_f$ , then  $t_{off} = t_f$ .

The gate-charge losses depend on the parasitic capacitance of the respective MOSFET, and is approximated by:

$$P_{L, cd} = 0.5 f_s (C_{oss} + C_{rss}) U_d \quad (\text{B.9})$$

For both switching losses holds, that assumptions are only valid, if diodes do not show forward and reverse recovery effects, which can easily produce an instantaneous current of twice the average current.

### B. Loss model of Diode

Forward conduction losses of diode:

$$P_{L, fwd} = \frac{1}{T_F} \int_0^{T_F} u_D(t) i_D(t) dt = U_{DF} I_{D, av} + r_{Don}(T_j) I_{D,RMS}^2 \quad (\text{B.10})$$

## B. DESIGN ASPECTS

---

In which  $U_{DF}$  is the diode forward voltage,  $I_{D,av}$  is the average current of diode,  $r_{Don}(T_j)$  is the diode on-state resistance.  $I_{D,RMS}$  is the RMS current of the diode.

The turn-on and turn-off losses of diodes are neglected, due to the low reverse recovery charge of SiC Schottky Diodes.

*C. Required Cooling* The maximal absorbable power dissipation of a heat sink is calculated by:

$$P_{th(max)} = \frac{\Delta \vartheta}{R_{thGK} + R_{thjG} + R_{thK}} \quad (\text{B.11})$$

$\Delta \vartheta = T_j - T_u$ , is the temperature difference between junction ( $T_j$ ) to ambient ( $T_u$ ) temperature,  $R_{thGK}$  is the heat transfer resistance at the surface,  $R_{thjG}$  is internal thermal resistance of junction to surface in the switching components,  $R_{thK}$  is thermal resistance of heat sink.

In order to keep components of the power supply in an acceptable temperature range, the losses of all components should be kept smaller as the maximal acceptable dissipation of the heat sink, that is  $P_{th(max)} > P_{L,all}$ .